Investigation of Turbulent Flame Characteristics via Laser Induced Fluorescence

Dem Fachbereich Maschinenbau

an der Technischen Universität Darmstadt

zur Erlangung des Grades

eines Doktor-Ingenieurs (Dr.-Ing.)

genehmigte

Dissertation

von

Dipl.-Ing Sunil Kumar Omar (M.Tech.)

aus Sumerpur(U.P.), Indien

Berichterstatter	Prof. Dr.-Ing. J. Janicka
Mitberichterstatter	Prof. Dr.-Ing. H.-P. Schiffer
Mitberichterstatter	Dr.rer.nat.habil. A. Dreizler
Tag der Einreichung	08.12.2005
Tag der mündlichen Prüfung	03.03.2006

Darmstadt 2006

D17

Hiermit erklre ich, dass ich die vorleigende Dissertaion selbstndig verfasst und nur die angegebenen Hilfsmittel verwendet habe. Ich habe bisher noch keinen Promotionsversuch unternommen.

Sunil Kumar Omar,
Darmstadt im März 2006

Acknowledgements

The present work was performed at the Institute of Energy and Power-plant Technology (EKT) at the Darmstadt University of Technology, Germany.

I wish to express my sincere thanks to the head of the institute, Prof. Dr.-Ing. Johannes Janicka, for his great support and offer to pursue a PhD. under his supervision. I am grateful to him for his steady optimism and trust towards my dissertation work.

My sincere gratitude goes to Prof. Dr.-Ing. Heinz-Peter Schiffer (TU-Darmstadt) for his willingness to report on my work.

I greatly acknowledge the support and guidance from Dr.rer.nat.habil. Andreas Dreizler, who was kind and patient enough to assist me through out this work. His perpetual enthusiasm in the area of combustion and laser diagnostics was always the source of encouragement and inspiration to me. I also thank him for his tireless effort and never give-up attitude, which led me finish this work.

I am heartly greatful to my colleagues Rajani Akula, Andreas Ludwig, Mark Gregor, Dirk Geyer, Cristoph Schneider and Andreas Nauert for many professional discussion. I wish to thank Andreas Kempf, Markus Klein, Bernhard Wegner, Elena Schneider for the pleasant working atmosphere during my stay at EKT. Many thanks to the diplom students Jan Brübach and Axel Sättler for their kind help in the laser lab. I take my opportunity to thank all EKT staffs and technical workshop staffs for their kind support and letting me use the available facilities.

Many thanks to Dr. M.Renfro and V.Krishnan for their help during the collaborative project work in turbulent opposed jet flames at the Purdue University, Indianapolis USA.

I wish to thank Himanshu Verma, Dr. Rahul Harshe, Amit, Santosh, Sidharth Sekhar and Anita Singh for their moral support and great time we had together.

I owe a great debt of gratitude to my family specially my parents, who have always been very loving, supportive and believed in my abilities. My heartily thanks goes to my supportive brother's Pankaj Omar, Rajendra Gupta, my only sister Ruchi Omar and sister-in-law Seema Gupta. I could have never came such far without their support and affection towards me.

To my parents, Shri. Raj Kumar Gupta and Smt. Rani Gupta

Sunil Kumar Omar
Darmstadt, March 2006

Contents

Nomenclature

Latin Symbols

Symbol	Dimension	Definition
a_m	$[s^{-1}]$	mean strain rate
a	$[s^{-1}]$	strain rate
A		peak amplitude of exponential decay
A_G	$[mm^2]$	global area
A_L	$[mm^2]$	local area
b_{12}	$[s^{-1}]$	rate constant for stimulated absorption
b_{21}	$[s^{-1}]$	rate constant for stimulated emission
B		background signal from exponential decay
c		optimized parameter
c_0	$[ms^{-1}]$	speed of light
d_b	$[mm]$	bluff-body diameter
d_{cf}	$[mm]$	co-flow nozzle diameter for swirl burner
D_{in}	$[mm]$	nozzle diameter for opposed jet burner
D_{cf}	$[mm]$	co-flow nozzle diameter for opposed jet burner
E_1	$[cm^{-1}]$	upper energy level
E_2	$[cm^{-1}]$	lower energy level
$E_{i,j}$		sensitivity
f_{st}		stoichiometric mixture fraction
f		mixture fraction
f_l	$[m]$	focal length
f_n		f number
h	[J s]	Plank's constant

H	$[mm]$	distance between the nozzles
I		intermittency
I_{sat}^{ν}	$[Wm^{-2}]$	saturation irradiance
I_{ν}	$[Wm^{-2}]$	incident laser spectral irradiance
k	$[J]$	turbulent kinetic energy
k_b	$[JK^{-1}]$	Boltzmann constant
k_f		rate coefficient
L	$[mm]$	integral length scale
L_{bottom}	$[m]$	flame length
m		constant in non-linear diffusion filter
n	$[cm^{-3}]$	number density of molecule
n_1	$[cm^{-3}]$	number density of the molecule in electronic ground state
n_2	$[cm^{-3}]$	number density of the molecule in electronic excited state
n_1^0	$[cm^{-3}]$	lower level population prior to laser excitation
P_d		photoionization
P	$[W]$	thermal power of the flame
Q_{gas}	$[lthr^{-1}]$	flow rate of fuel (Swirl Burner)
Q_{air}	$[lthr^{-1}]$	flow rate of air (Swirl Burner)
r	$[mm]$	radial flow field co-ordinates (Opposed Jet Burner)
R	$[mm]$	radius of the inner nozzle (Opposed Jet Burner)
RR	$[mollt^{-1}s^{-1}]$	forward reaction Rate
Re		Reynolds number
s_l	$[ms^{-1}]$	flame velocity
S		swirl number
Sc		Schmidt number
Si_{OH}		lif signal from hydroxyl molecule
Si_{HCHO}		lif signal from formaldehyde molecule
t_{res}	[ms]	residence time of eddy
t_{ov}	[ms]	large eddy turn overtime
$\overline{u}$	$[ms^{-1}]$	mean velocity
$\dot{u}$	$[ms^{-1}]$	bulk velocity
u'	$[ms^{-1}]$	velocity fluctuation
W		predissociation
Y_{α}		mass fraction of element α
$Y_{\alpha,O}$		mass fraction of element α in oxidizer flow

$Y_{\alpha,F}$		mass fraction of element α in fuel flow
z, Z	[mm]	axial flow field co-ordinates

Greek Symbols

Symbol	Dimension	Definition
τ_l, τ	[ns]	lifetime
τ_I	[ms]	integral time scale
ν	[Hz]	light pulse frequency
Ω	[sterad]	collection solid angle
ω	[nm]	light frequency
θ	[rad]	flame angle
λ_w	[nm]	wavelength of laser pulse
λ		contrast parameter
λ_B		air-to-fuel ratio
ϕ, ϕ_B		equivalence ratio
η_B	[mm]	Batchelor length scale
η_k	[mm]	Kolmogorov length scale
ρ		autocorrelation function
ρ_u	$[kgm^3]$	density of unburned fluid
ρ_b	$[kgm^3]$	density of burned fluid
∇		gradient operator
σ		gaussian kernel
Å		Angstrom

Abbreviations

BBO	beta borium borate non-linear crystal
CCD	charge coupled device
CFD	computational fluid dynamics
DCS	direct current sampling

DPR	dual pulse resolution
DNS	direct numerical simulation
EKT	Fachgebiet für Energie- und Kraftwerkstechnik (Institute for Energy and Power-Plant Technology)
$FWHM$	full width half maximum
GTI	Gires-Tournois interferometer
$ICCD$	intensified charge coupled device
IEO	international energy outlook
IR	infra-red
$LASKIN$	LASer KINetics (a simulation program for time-resolved LIF spectra)
LBO	lithium tribonate non-linear crystal
LDV	laser Doppler velocimetry
LES	large eddy simulation
LIF	laser induced fluorescence
LII	laser induced incandescence
MCA	multi-channel analyzer
NIM	nuclear instrumentation method pulse
$NLDF$	non-linear diffusion filter
$OPPDIF$	opposed jet diffusion flame
PBP	pellin-broca-prism
PDF	probability density function
$PITLIF$	pico-second time-resolved laser induced fluorescence
PIV	particle image velocimetry
$PLIF$	planar laser induced fluorescence
PMT	photomultiplier
PSD	power spectral density
$RANS$	Reynolds averaged numerical simulation
RET	rotational energy transfer
RLD	rapid lifetime determination
SFB	Sonderforschungsbereich
SNR	signal-to-noise ratio
SPC	signal photon counting
TAC	time-to-amplitude convertor
TGP	turbulence generating plate

TNF	turbulent non-premixed flame
TOJ	turbulent opposed jet flame
UV	ultra-violet
WEX	wavelength extender
$WLLS$	weighted linear least-square method

Molecular Species

CH	Methylidyne
$CH_2O, HCHO$	Formaldehyde
CH_4	Methane
OH	Hydroxyl
HCO	Formyl

1 Introduction

The world is using an increasing amount of energy. Both the developed and less developed countries are demanding larger shares of world energy resources. At the same time, it is fully recognized that such resources are limited. Most are fossil fuels, formed underneath the surface of the earth millions of years ago. They will not easily be replenished! The most plentiful source of fossil energy is coal. This is essentially carbon but contains a number of impurities such as nitrogen, sulphur, and chlorine. Another group of fuels is the hydrocarbons. These may be liquid or gaseous and are compounds of hydrogen and carbon in different proportions. However, coal is well suited to industrial processes such as power generation, but it is difficult to store and transport. Hydrocarbons provide convenient automotive power, whether on the road or in the air.

Fossil fuels remain the primary source of energy for domestic heating, power generation and transportation. Other energy sources such as solar energy, wind energy or nuclear energy still account for less than 20 percent of total energy consumption. Therefore combustion of fossil fuels, being humanity's oldest technology, remains a key technology today and even in foreseeable future. On the same token, world energy consumption is projected to increase by 58 percent over 24-years forecast horizon, from 2001-2025 [IEO2003].

Today, combustion of fossil fuel is the main source of energy for mankind. However, it is also the major contributor to the pollution in earth's atmosphere. It pollutes the earth by emitting exhaust gases from various combustion processes. If the combustion process of fossil fuel is perfect, the only elements remaining would be carbon dioxide, water, nitrogen and excess oxygen. Unfortunately, combustion isn't perfect, thus emitting pollutants in the process such as carbon monoxide, UHC (unburnt hydrocarbons), NOx, sulphur dioxide etc. These gases effect our local as well as global environment causing air pollution, acid rain, global warming, forest fire and other hazards. Thus understanding of combustion processes and improvements are necessary to lower the emission, while

maintaining a high efficiency rate. It is thus important to increase the efficiency of combustion and reduce pollution in order to improve the quality of life and save all endangered species around the globe.

Turbulent combustion is an important technical process found mostly in all practical industrial devices, like automotive engines, gas turbines and power plants (boilers etc). A significant amount of effort is ongoing to improve the knowledge of combustion under turbulent environment, both experimentally and numerically. The improvement in terms of efficiency and pollution reduction in practical combustion systems is an immense task. In addition, it requires complete understanding of complex processes and interaction involved with turbulent combustion. Understanding of turbulent combustion requires knowledge on turbulent flow field, combustion chemistry and their interaction with other processes. One of the interaction is interaction between turbulent flow field and combustion chemistry known as turbulent-chemistry interaction that occur in molecular level during combustion. Due to its complexity and insufficient knowledge, it still remains an attractive research topic around the globe.

Improvement in combustor design, its efficiency and to meet future emission constraints requires the fundamental understanding of turbulent combustion and its complex interactions. The motivation for understanding turbulent combustion to design future combustion system arises from two primary reasons: 1) the systems are too complex to be understood easily, and trial and error techniques of design simply do not work and 2) the systems are too large that trial and error techniques are far too expensive to practice. Therefore a better understanding of combustion is required, which will give an insight into the physical understanding of the complex behavior and hence significantly reduce the dependence on the trial and error technique.

Modelling technique is mainly used to design combustors in the industrial environment, but there is limitation to these modelling technique. In order to test for the efficiency and capabilities of these numerical models, relevant experimental data is required. With increasing computational power and growing importance of numerical studies, pressure to generate good and useful experimental data is huge. The assessment and validation of new and improved numerical models need experimental data, in order to correctly predict the complex physical phenomenon involved with turbulent combustion. Present work contributes to increase knowledge on turbulent combustion, that will enable the combustor de-

signers to achieve three important targets: to save fossil fuels, to minimize the formation of pollutants and to reduce the cost of energy produced from fossil fuels.

More specifically, current work aims to provide experimental information on various laboratory friendly and technical relevant flames that mainly solve two purposes: firstly data will allow the numerical simulators to test the efficiency of existing numerical models and secondly it tries to explain the physics behind the complex process that is involved with turbulent combustion. Above mentioned twin-fold importance remains to be the motivation of the thesis.

First part of the thesis illustrates the background and basics of turbulent combustion, various complex interaction involved and the framework adopted to improve on its understanding. It also provides information on turbulence-chemistry interaction which remains to be the bottleneck unresolved problem among the researchers around the globe. Importance of experimental studies for validation purpose and limitation of numerical studies is also detailed in the same chapter. Third chapter introduces the basic principles on the laser based technique (Laser Induced Fluorescence) utilized to investigate the flame characteristics in the current work. Methods to evaluate quantitative information from the fluorescence signal is also depicted and available techniques are as well explained.

Chapter four is more specific. It provides the information on important parameter of interest that has been measured and evaluated during this work. Information on single point and two-dimensional measurement along with literature survey on previous work is also described. This chapter will provide the basic platform on the parameters needed for the study and thereafter, subsequent chapters will demonstrate its application and show the results obtained during the measurement of various flames.

Details on experimental set-up and instrumentation utilized to carry out measurements in turbulent flames is provided in chapter five. This chapter is divided according to the type of flames measured, first two sections detail on experimental methods used in application on turbulent opposed jet flame, whereas last section details on turbulent swirl flame. Chapter six, talks about the importance of image processing to evaluate the information from the raw planar image taken during the experimental measurements. This chapter also lets us to choose the right filtering and the image processing technique to extract relevant information from the planar LIF images.

Last three chapters provides the outcome from the experimental measurement in various flames. Discussion and conclusion is also done to visualize the outcome and improve our knowledge in these turbulent flames. Future work and important conclusion from the present work is provided in the chapter with heading "Summary and Outlook".

2 Turbulent Reacting Flows

This chapter introduces the concept of turbulent combustion, its processes and its complex behavior. Typical framework that has been proposed to understand the turbulent combustion and its complex behavior is also explained. This includes the importance of combined effort from both numerical and experimental methods and their current status in the field of turbulent combustion.

2.1 Introduction on Turbulent Combustion

Turbulence phenomenon is still living up to its expectation as Werner Heisenberg once answered, when he was asked what he would ask God, given the opportunity. His reply was: "When I meet God, I am going to ask him two questions: Why relativity? and why turbulence? I really believe he will have an answer for the first".

Turbulent flow is characterized by the complex motion of fluid molecules that are mainly composed of circular structures (eddies) and moving in a chaotic manner in all directions. During visualization of such flows, one would observe complicated instead of simple streamlined patterns in the flow. Flows that are pseudo-random, three dimensional, unsteady, swirled structured and dissipative (i.e. kinetic energy is changed into heat as the flow progresses) in nature are defined as "turbulent flows". Turbulence in fluid flow, is encouraged since it strongly enhances the mixing process between the fluids. Large-scale vortex motion and mixing at molecular level through diffusion are the cause for mixing process between the fluids.

Turbulence itself is a very complicated non-linear problem. Turbulent reacting flows are a step ahead in terms of complications, because it involves strong interaction of several physical and chemical processes such as turbulence, mixing, mass and heat transfer, radiation and multi-phase flow phenomena [1] (see figure 2.1).

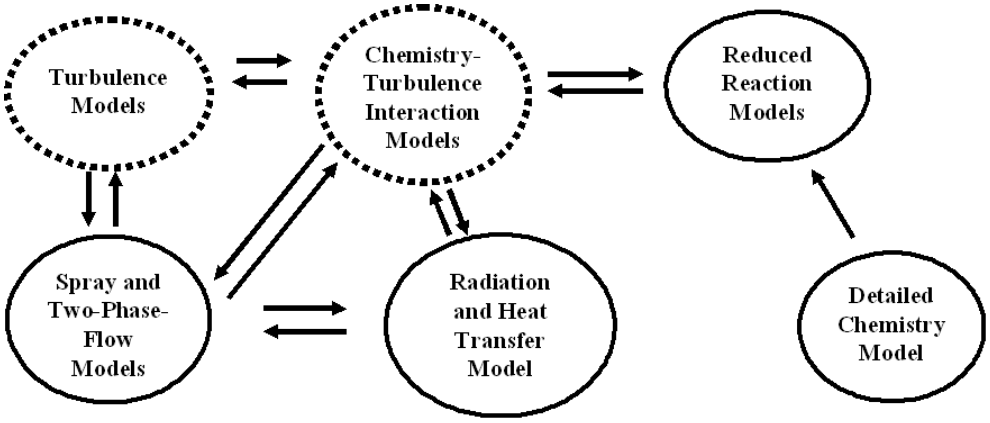

Figure 2.1: Structure of integral and sub-models showing various processes and interaction involved with turbulent combustion

This complicated picture can be reduced, if multi-phase phenomena and radiation effect is opted out in the turbulent reacting flow. Even then, the strong non-linear coupling between turbulence and chemistry is extremely difficult and requires understanding at the fundamental level. This is mainly because the chemical reaction can involve hundreds of species and thousands of elementary reactions, with a wide range of chemical reaction length and time scales, starting from a nanometer regime of molecular encounters to combustor dimension of a few meters. Some of which may overlap with the turbulent flow scales, thus complicating the flow field structure.

In turbulence-chemistry interaction, initially turbulence causes the mixing of reactants through large scale vortices in the flow field, small scale molecular mixing then proceeds the chemical reaction. During chemical reaction heat is released, which alters the density field thus modifying the turbulent flow field. This non-linear coupling of turbulent flow and chemical reaction is the most complex and challenging topic for the researchers working in the field of turbulent combustion.

This thesis is limited to the critical issue of turbulence-chemistry interaction in turbulent flames. Almost in all practical combustion systems such as internal combustion (IC) engines or gas turbines (GT), chemical reactions takes place in a turbulent flow field. Therefore, in order to develop more efficient and environment friendly combustion systems, the fundamental knowledge of this interaction and its reliable prediction in turbulent reacting flow is required.

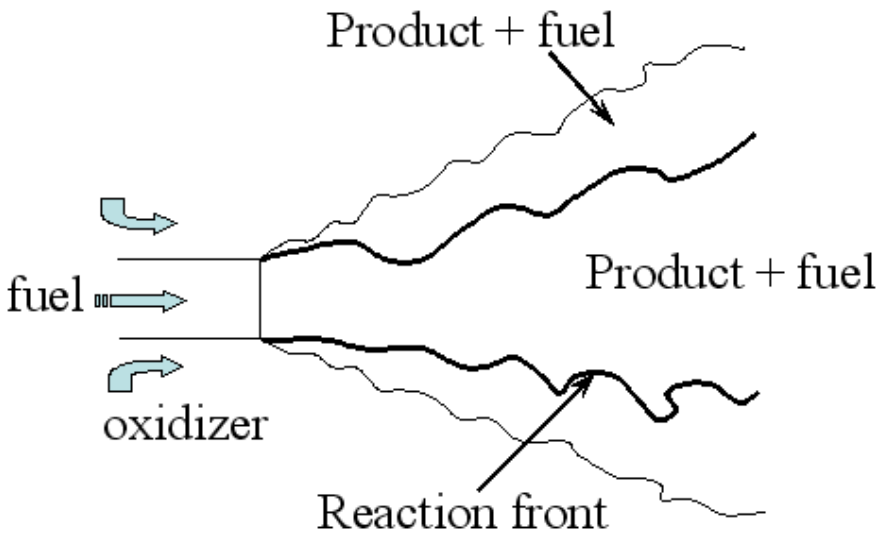

Figure 2.2: Schematic drawing of a turbulent non-premixed jet flame

2.1.1 Modes of Turbulent Reacting Flows

Fortunately, turbulent reacting flows are classified only into premixed and non-premixed modes of combustion. This classification has to do with the state of mixing of the reactants before entering the reaction zone. If the reactants are separately fed into the reaction zone, the resultant flame is known as non-premixed flame. Mixing brings reactants into the reaction zone where thin layer of burnable mixtures at different are formed and combustion takes place. Most of the mixing in this thin zone occurs mainly by a molecular diffusion process. On either side of the reaction zone, the mixture is either too lean (oxidiser side) or too rich (fuel side) for chemical reaction to take place (see figure 2.2). Non-premixed flames are normally safe and simpler to operate because they are not mixed prior to the combustion chamber and they do not propagate against the flow, as their premixed counterpart. Non-premixed flames are of major interest in gas turbine engines, jet engines, Diesel engines, boiler, furnace etc.

The main disadvantage of pure diffusion flames is their pollutant generation. This is because the fuel does not get enough oxidant in the right place resulting in incomplete combustion. In such flames, maximum combustion temperature is achieved at the location, where the mixture is stoichiometric and this is associated with increased production of NO_x. Stoichiometry is used to refer to the ratio of

oxidizer to fuel which just leads to complete product of combustion. One of the useful qualities related to stoichiometry is equivalence ratio (ϕ). It is the ratio of fuel to oxidizer by weight in a given case to that to stoichiometry stated in the form of an equation 2.1. Thus all stoichiometric mixture have equivalence ratio of unity. Rich mixtures have ϕ greater than unity, whereas lean mixture have ϕ less than unity.

$$\phi = \frac{fuel/air}{fuel/air_{\,stoichiometry}} \tag{2.1}$$

In a two feed system as shown in figure 2.2, one can introduce a conserved scalar, mixture fraction, as a dimensionless element mass fraction shown in equation 2.2

$$f_\alpha = \frac{Y_\alpha - Y_{\alpha,O}}{Y_{\alpha,F} - Y_{\alpha,O}} \tag{2.2}$$

Where Y_α denotes mass fraction of element α. The second subscript, F and O refers to the fuel and oxidizer in their initially unmixed state and $Y_{\alpha,F}$, $Y_{\alpha,O}$ corresponds to the element mass fraction value in the fuel and oxidizer streams respectively.

In contrary to the diffusion flames considered in last paragraphs, the reactants in premixed flames are thoroughly premixed homogeneously on the molecular scale before entering the reaction zone. The reactants in a premixed flame are mixed before chemical reaction occurs therefore the chemical reaction rate determines the overall reaction rate in such flames. Combustion in such flames occurs by propagation of a reaction front through the flow. In such flames the combustion zone is defined mainly by two main zones, i.e. the preheated zone and the reaction zone. Initially, in the preheated zone the mixed reactants proceed intensively due to diffusion of heat and mass without any chemical reaction. Thereafter, the chemical reaction occurs and the reaction rate increases at high level. At this reaction zone combustion occurs and maximum heat is released. They are compact in nature and the common application is in Spark-Ignition engines that are mostly used in cars.

The above mentioned non-premixed and premixed regimes of combustion are classified according to the mixing condition of the reactants. However, in technical applications, there are very few situations where one of these combustion

regimes appears in their pure form. The combination of non-premixed and premixed regimes takes place more often to produce so called partially premixed combustion. Partially premixed phenomenon can be seen in triplet flame. In particular, triplet flames essentially comprise three flames, namely a rich premixed flame accompanied by a diffusion flame in the middle and followed by a lean premixed flame. Similarly, in partially premixed flames the equivalence ratio of the fresh gas mixture directly in vicinity of the flame front is still within the flammability limits. If the equivalence ratio ϕ varies only within the lean region, the complete fuel consumption occurs in the flame front. But if the mixture includes rich value of ϕ, then the premixed flame is accompanied by an additional diffusion flame in the post flame region where the remaining fuel oxidizes. In such flames, strong interaction of fluid dynamics, mixing and chemical reaction is found.

Over the last two decades, significant advances have been made on turbulent non-premixed combustion. These advances have been closely associated with a series of international workshops on turbulent non-premixed flames(TNF, 2000). By the same token, advances in premixed flames have been relatively less in comparison with turbulent non-premixed flames. Reason for this sluggish advances is because premixed turbulent combustion is inherently more complex than non-premixed and also associated with much stronger coupling between the chemistry and the turbulence [2].

2.2 Framework to Understand Turbulent Reacting Flows

Typical framework for turbulent combustion research is through close collaboration between experimental, numerical and theoretical studies with a focus on understanding the interaction between turbulence and flame chemistry. This close collaboration has led to the continuous improvement in the measurement technique and the numerical models (Computational Fluid Dynamics) respectively. Even after such improvements and numerous advances, turbulent combustion still remains to be the most challenging topic today.

Numerical model design and development have been increased in past years due to the availability of increased computer power. While developing future

numerical models, the major questions we want to answer is whether we can make a model to predict the flame physics and utilize this knowledge to design efficient practical combustion devices. In order to validate and further develop efficient numerical models, there is continuous need of experimental data. This includes providing precise and accurate experimental results that is well aligned with the capabilities of the modelling and simulation techniques. Therefore, researchers around the world are working in collaboration to generate the required data base for turbulent flames and further develop innovative modelling and measurement techniques.

2.3 Experimental Methods

2.3.1 Introduction

Under the above mentioned framework to understand the turbulent reacting flows, Bray [3] outlined the essential role of experiments in model development and named several attributes of ideal experiments. The main purpose was to measure data complete enough that quantitative comparison with model calculations can be performed without ambiguity. The outcome from the combustion modelling depends on the quality and quantity of measured data provided by the experimentalist. Therefore experimental data must meet certain requirements, which includes accurate initial and boundary conditions, choice of simple flow configuration, sufficient amount of data and spatially covering whole region of interest.

The complete data set includes relevant physical properties of turbulent flames as a function of field variables such as mass fraction of species concentration (both major species such as fuels and oxidants, the intermediate species such as flame radicals), as well as flow field velocity, density, temperature, flame front location and the location of heat release rate [4]. Hassel et al. gives an overview of data, connected to the different sub-models for turbulent combustion and common methods to measure them [5]. These measurements are divided into two different classes, first is represented by single point measurements from which a large statistical data base can be established. Second is field measurement to study the flame dynamics and its structural characteristics.

A complete characterization of turbulent flames may require measurement data

acquired from a multi-dimensional (2D or ideally 3D) measurement technique. As the turbulence is also inherently time-dependent the experiment should be performed with high temporal resolution, and the acquisition time for each data point must be short enough to freeze the flow. In order to get the detailed insight on the turbulent combustion phenomenon, multiple quantities must be measured simultaneously.

2.3.1.1 Laser Diagnostics

Measurements using traditional techniques such as thermocouples and gas sampling probes, while useful for certain applications, are limited by their intrusiveness when used in combustion environment. Besides perturbing the flow field they are often limited in their spatial resolution and temporal response. Several other limitations are associated with individual sensors for example thermocouples. It requires radiative corrections which can introduce a large source of uncertainty in the temperature measurement. Similarly, with species measurements gas sampling probes cannot measure the highly reactive combustion intermediate such as hydroxyl radical. This molecule is an important intermediate during combustion, where air as oxidizer is involved.

Therefore, measurements are done preferably with laser diagnostics methods due to their non-intrusiveness, high repetition rate, high spatial and temporal resolution. Several individual measurement techniques using laser have been developed to great accuracy in recent years. Laser based spectroscopic techniques play an important role in the field of turbulent reacting flows. High spatial resolution ($\sim$50 μm) can be obtained by focusing the laser beam to a small point or a narrow sheet. The data can be sampled using an extremely short measurement time, which is determined by the laser pulse length ($\sim$10 ns), this effectively freezes all turbulent flows and allows instantaneous measurements. In most cases the measurements are non-intrusive, which ensures that measurements are performed in an unperturbed system.

The disadvantages of the laser based spectroscopic techniques are: the need of optical access on the test rig and measurements close to walls although highly desirable are generally difficult to perform. This is due to the intense scattering from the surface.

Common laser based measurement techniques are Laser Induced Fluorescence

(LIF) for intermediate species measurement, spontaneous Raman spectroscopy (SRS) for major species. Temperature can be measured either indirectly through the gas density by Rayleigh scattering or by probing the spectroscopic state of atoms or molecules using LIF or coherent anti-stroke Raman scattering (CARS). Laser Doppler Velocitimetry (LDV) can be used to determine gas velocity field and its higher moments. Combination of some of the measurement techniques are common and some are under development. For example, simultaneous Raman/Rayleigh/LIF measurement have been done in a turbulent diffusion jet flame [6] and simultaneous Raman-LDV scattering measurements have been done by Dibble et al. [7]. On the same path simultaneous Raman/Rayleigh/LDV measurement and its application in turbulent flames is under development in TU-Darmtstadt [1].

2.3.1.2 Multi-dimensional Measurements

Laser spectroscopic techniques can be implemented to register information from a single point, along a line, in a plane and in some cases even in a volume. Single point measurement can be performed by focusing the laser beam into a small point and signal can then be detected using a spatially integrating detector.

Detailed point measurements have proven very useful in order to generate a comprehensive database. This may include the information on turbulent flow field [8],[9], turbulence structure [10], scalar fluctuation [11] and the lifetime of intermediate species [12]. Turbulent flow field information comprises mean velocity, higher order moments and Reynolds-stresses. Whereas temporal time scales, spatial length scales and the power spectral density are the information associated with turbulence structure. All these measurements can only be done using single point or two-point measurement techniques due to the limitation of sufficient spatial resolution on the laser based diagnostic methods.

In 1-D measurements the laser beam is formed to a narrow line and the signal along a portion of the laser beam is imaged onto a 1-D or 2-D array detector. Such measurements are undertaken, if there is a difficulty in accurately measuring a parameter in a single-shot basis with sufficient spatial resolution. Multi-scalar line Raman measurement in a turbulent opposed jet flame is one such example [13]. Another example is where double pulse line measurements of major species concentrations and temperature have been performed using Raman and Rayleigh

scattering [14].

Two-dimensional measurements are the state of the art techniques that are performed when sufficient signal from the flame is available and can be accurately detected in a single-shot basis. Such measurement provides detailed understanding of the flame front topology and structural dynamics of the turbulent flames. 2-D measurements are performed by forming the laser beam to a narrow sheet of high spatial resolution and then focussed into a planar region. Wherein, the signal is generated and can be detected using a 2-D detector. Several planar measurements utilizing a wide range of laser diagnostic techniques have been reported in the field of turbulent combustion such as Planar measurement utilizing LIF [15], Raman [16], Rayleigh [17],[18].

As turbulence is an intrinsically three-dimensional phenomenon, 3-D measurements of relevant flow and flame quantities are highly desirable. 2-D imaging techniques can be extended to obtain quasi 3-D information by rapidly recording a stack of closely spaced planar images. This is feasible by sweeping the laser beam through the measurement volume using a rapidly rotating mirror [19],[20].

2.3.1.3 Multi-scalar Measurements

Several laser spectroscopic techniques can be used in combination to yield simultaneous data of two or more parameters and are highly recommended. The combined information of several flame and flow quantities can be used to study the structure of turbulent flame fronts. Usually more than one laser and detector system is needed for this type of experiment where the different laser beams are overlapped to generate all signals in the same experimental region.

Multi-scalar, time averaged, point measurement of major species concentration, intermediate radical and temperature have been performed by using combined Raman/Rayleigh/LIF measurements [21]. Simultaneous measurements of velocity and scalars are of great interest in turbulent combustion because of the need to validate models for scalar-velocity correlation. In recent years, PIV have been combined with planar imaging of various scalars, including OH, CH, fuel and temperature. more recently, joint PDF measurement of velocity and scalar measurement was done by using simultaneous LDV and PLIF measurement by Nauert *et al.* [22].

Simultaneous CH/OH have been used to study the location of stoichiometric

contour and flame surface density in non-premixed flames by Donbar *et al.* [23]. Instantaneous reaction rate and temperature field imaging was done using simultaneous measurement of hydroxyl and formaldehyde concentration with Rayleigh scattering in a turbulent flame [24]. In the present work, multiple-scalar measurement laser based techniques are utilized to identify the location of peak heat release rate in a turbulent swirl flame.

2.4 Numerical Modelling Methods

Characterization, modelling and numerical simulation of turbulent combustion requires the understanding and modelling of complex turbulent flows, the chemical reactions of fuel and oxidizer, including the generation of pollutants, energy transfer via radiation and the interaction of all these aspects, complicating matters by far. Until now the most challenging part is the treatment of turbulent reacting flows. This phenomenon is partly understood, and its complete numerical handling requires immense computer processing time and storage.

In turbulent combustion, the description and modelling is based on the system of a large number of coupled partial differential equations describing both fluid flow and chemistry. These equations need to be solved in space and time domain. These full and general set of differential equations governing the motion of a fluid is referred as Navier-Stokes Equation. In the final analysis, these equation comprise the equations expressing conservation of mass, linear momentum, and energy for general motions. An overview of different approaches to solve or model these equations are found for example in [25],[4] and will not be discussed in detail. The main idea of this section is to provide information on available numerical methods for the treatment of turbulent flows.

Numerical investigation of turbulent combustion can be classified into three major groups: direct numerical simulation (DNS), Reynolds averaged Navier-Stokes modelling (RANS), and large eddy simulation (LES).

A full description of the turbulence in flames is carried out in DNS. For given chemistry and transport models, all the scales (time and length) are solved directly with the Navier-Stokes equations for reacting flows. Due to the huge computational cost and processing time involved, its application is restricted to the low Reynolds number flows only. Due to Reynolds number limitations, DNS

does not allow calculations of real combustion chamber configurations or characterization of high turbulent combustion flames. As computational power is increased in recent years, DNS may be able to resolve the combustion flame of technical relevance.

Improvement and development of the design of technical devices in the industrial application has been widely done with RANS modelling. Useful information on time-averaged quantities such as fuel consumption or pollutant formation at an affordable computational cost is the main attraction of this modelling technique. It is done by formulating time-independent equations that describes the mean quantities.

Large eddy simulation (LES) stands in the middle of the range of turbulent flow prediction tools, between direct numerical simulation (DNS), in which all scales of turbulence are numerically resolved, and Reynolds-averaged Navier-Stokes (RANS) calculations, in which all scales of turbulence are modeled. In LES, the large, energy- containing scales of motion are simulated numerically (as in DNS), while the small, unresolved sub-grid scales and their interactions with the large scales are modelled. The large scales, which usually control the behavior and statistical properties of a turbulent flow, tend to be geometry and flow dependent. This dependence is difficult to capture in Reynolds average models and makes LES well suited for studies of combustion instabilities. The explicit calculation of large structures also allows a better description of turbulence chemistry interactions.

Main aim of the current work is to provide experimental data, which assists in the development of such modelling technique. The development of above mentioned modelling techniques have been highly dependent on the experimental results taken from various diagnostics methods. This collaboration has helped in developing both experimental and numerical techniques keeping in the mind to provide better understanding of turbulent reacting flows.

3 Laser Technique

Flame diagnostics involves detection and identification of the intermediate species in the flames. Therefore, a measurement technique is required that can provide the information on the intermediate species and important radicals occurring during the combustion. Here in this section, a well-known minor-species detection technique known as laser induced fluorescence(LIF), is presented.

This technique is of a great importance in combustion studies due to its species specific property, non-intrusiveness, high temporal and spatial resolution. It is one of the most successful and a frequently used method for minor-species detection in combustion flames. Almost 20 percent of all published experimental papers in twenty-seventh symposium on combustion utilized LIF as a experimental technique, shows its popularity [26]. All the experimental measurement undertaken in this work utilizes LIF as laser diagnostic method.

3.1 Introduction

Any substance that emits light, is a luminescent substance and the phenomenon is known as luminescence. Luminescence occurs when a substance is excited by an external energy source from a ground state to an unstable energy state. While returning back to the stable ground state, it emits energy in the form of light. If the excitation is due to the chemical reaction, it is called chemiluminescence. Moreover, if a light pulse is used as a external source for excitation and the emission that follows the excitation lasts only for a short duration, then the phenomenon is known as fluorescence.

Fluorescence is the spontaneous emission of radiation by which the molecule or atom relaxes from an upper energy level to the ground level. The optical excitation is normally through a laser pulse that is carefully tuned to a transition from a lower to an upper state of the targeted species. If the target molecule is resonantly excited by the laser source, then a photon of energy hν will be

absorbed, bringing the molecule from a ground state to a certain rotational and vibrational level in a higher electronic state. Where h is the Plank's constant and ν is the tuned frequency. Such a state is unstable and the population is rapidly redistributed by the rotational energy transfer (RET), as illustrated in the figure 3.1. This redistribution results in populating of the neighboring rotational sub-levels, as well as spontaneously emitting another photon of energy hν before it decays to the rotational and vibrational sub-levels in the ground electronic state.

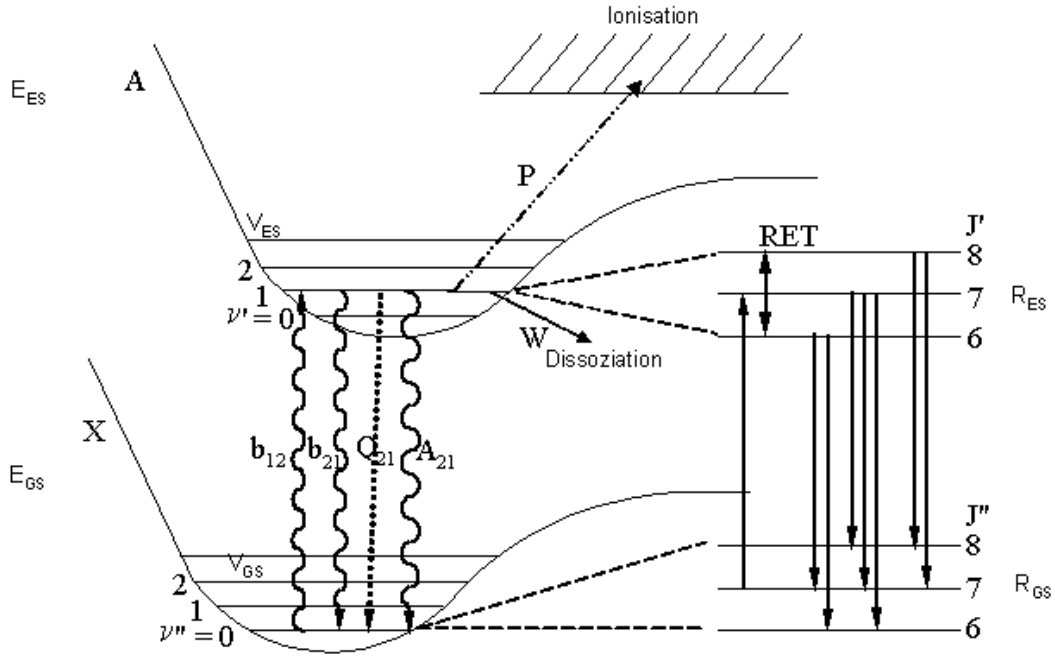

Figure 3.1: Full model for laser-induced fluorescence. Subscript GS represents ground state and ES excited state. V represents vibrational level, E electronic level and R rotational level. RET is rotational energy transfer, P loss due to ionization, W loss due to dissociation.

The fluorescence photons are emitted in all directions with an equal probability and are the source of the LIF signal. These emitted photons can be collected with the help of a CCD camera or a photomultiplier, thereby giving information about the chemical and physical properties of the species.

Although an atom or molecule at a higher energy level may not necessarily emit radiation, as several other pathways for this loss compete with the fluorescence

(see figure 3.1). Some of these are dissociation, energy transfer to nearby species through collision, other internal energy states and chemical reaction. Among all losses, electronic quenching (Q_{21}) of potential molecules will reduce the significant amount of fluorescence and is caused due to the collision between the molecules. Colliding molecule may transfer a part or all of its energy to the collision partner, without emitting a photon and hence contributes to the lost of signal. Quenching depends upon the pressure, temperature and on intermolecular characteristics of individual colliders.

W corresponds to predissociation and P to photoionization. Predissociation is the probability of the specific excited states, to decay without emitting radiation into fragments like neutral atoms. The fluorescence process can be easily understood by considering a simple two-level model and will be detailed in the next section.

There have been several reviews published on LIF from time to time. A historical perspective on the development of this technique and its application can be found from the book by Eckbreth [27]. More recently, two articles published in the Progress in Energy and Combustion Sciences provide the outlook on recent advancement on LIF [28],[29].

Laser-induced fluorescence is the technique of choice, if a strong signal from one specific molecular species is needed. Each atom or molecule has a specific absorption line and emission pattern that makes LIF species selective. It is an attractive technique with its application in several fields such as medical research, applied physics, chemical detection etc., other than its significant use in the field of combustion. Using LIF in the combustion environment, it has been possible to detect flame radicals, reaction intermediates and pollutants at, or even below, ppm (parts per million) levels.

3.2 Theory

The simplest two-level model of LIF is depicted, in which the medium is described by two electronic energy levels. In figure 3.2 the rate constants for the different optical and collisional processes connecting the upper and lower energy levels E_1 and E_2, are shown. Parameter A is the rate constant for spontaneous emission, given by the Einstein A coefficient. Variable b_{12} and b_{21} are, respectively, the

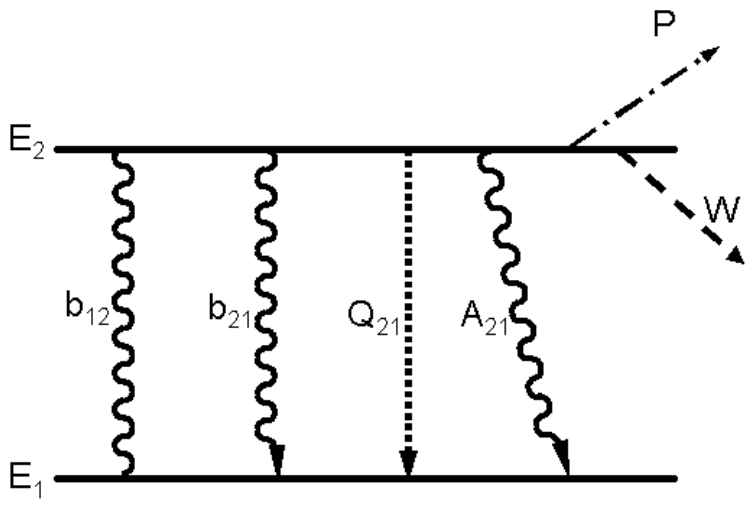

Figure 3.2: Simple two energy level diagram of LIF with the energy transfer processes

rates for absorption and stimulated emission and are related to the Einstein coefficients for stimulated emission, B, through

$$b = \frac{BI_\nu}{c}, \tag{3.1}$$

where I_ν is the incident laser spectral irradiance and c, the speed of light. Q_{21} corresponds to collisional quenching (dash line in figure 3.2), which is energy transfer without emission of light due to collision of molecules. The rate equations for the population densities of the two energy levels, n_1 and n_2, based on a simple two-level model with weak (unsaturated) excitation can be written as:

$$dn_1/dt = \dot{n}_1 = -n_1 b_{12} + n_2(b_{21} + A_{21} + Q_{21}) \tag{3.2}$$

and

$$dn_2/dt = \dot{n}_2 = -n_1 b_{12} - n_2(b_{21} + A_{21} + Q_{21}) \tag{3.3}$$

Where n_1 is the number density of the molecule in electronic ground state and n_2 is the number density of the molecule in electronic excited state. Number density is defined as the number of the molecule in a specific volume. The population conservation equation may be written as:

$$n_1^0 = n_1 + n_2 \tag{3.4}$$

where n_1^0 is the lower level population prior to laser excitation. Combining equations 3.2 and 3.3 and solving for n_2 gives:

$$n_2(t) = \frac{b_{12}n_1^0}{r}(1 - e^{-rt}) \tag{3.5}$$

Where $r = b_{12} + b_{21} + A_{21} + Q_{21}$. As long as rt $\ll 1$, there is continuous rise of population in upper state with time,

$$n_2(t) = b_{12}n_1^0 t \tag{3.6}$$

for rt > 1, stable condition is achieved

$$n_2 = \frac{b_{12}n_1^0}{r} \tag{3.7}$$

where the first factor gives the excited population at steady state, which is reached after a short delay called the pumping time, $\tau = 1/(b_{12}+b_{21}+A_{21}+Q_{21}) = 1/r$. At atmospheric pressure τ is much shorter than the duration of the laser pulse (<1 ns compared to 10 ns for a typical laser pulse), and the steady state population is given by:

$$n_2 = n_1^0 \frac{b_{12}}{b_{12} + b_{21}} \frac{1}{1 + \frac{A_{21}+Q_{21}}{b_{12}+b_{21}}} \tag{3.8}$$

Where I_{sat}^{ν} is the saturation irradiance:

$$I_{sat}^{\nu} = \frac{(A_{21} + Q_{21})c}{B_{12} + B_{21}} \tag{3.9}$$

After replacing I_{sat}^{ν} in equ 3.8 and simplifying in a new form:

$$n_2 = n_1^0 \frac{B_{12}}{B_{12} + B_{21}} \frac{1}{1 + \frac{I_{sat}^{\nu}}{I^{\nu}}} \tag{3.10}$$

The fluorescence signal power F is proportional to $n_2 A_{21}$ and can be expressed as:

$$F = h\nu n_2 A_{21} \frac{\Omega}{4\pi} V \propto n_1^0 \frac{B_{12}}{B_{12} + B_{21}} \frac{A_{21}}{1 + \frac{I_{sat}^{\nu}}{I^{\nu}}} \tag{3.11}$$

At low laser irradiance, $I^{\nu} \ll I^{\nu}_{sat}$. Thus, substituting for I^{ν}_{sat} and n_2 in equation 3.11 will result in simplified form shown in equation 3.13.

where n_2 (upper state population) is given by,

$$n_2 = n_1^0 \frac{I_\nu}{c} \frac{B_{12}}{A_{21} + Q_{21}} \tag{3.12}$$

$$F = h\nu B_{12} \frac{\Omega}{4\pi} V n_1^0 \frac{I_{nu}}{c} \frac{A_{21}}{A_{21} + Q_{21}} \tag{3.13}$$

Where $h\nu$ is the photon energy, Ω is the collection solid angle and V the interaction volume. The fluorescence signal is linearly proportional on the number of molecule in the focal volume n_1^0V and the laser irradiance I_{nu}. Additionally, it depends on the Einstein coefficient for stimulated absorption B_{12} and on the quenching rate Q_{21}. The term $A_{21}/(A_{21} + Q_{21})$ can be interpreted as a fluorescence efficiency, it is generally much smaller than 1 as $A_{21} \ll Q_{21}$. In order to quantify the signal from laser induced fluorescence, all the parameter in the equation 3.14 should be correctly predicted.

$$F \propto B_{12} A_{21} n_1^0 \tau_l \tag{3.14}$$

where τ_l is the lifetime and equal to $(A_{21} + Q_{21})^{-1}$.

It is important to perform the global calibration of the set-up for quantitative measurement. Factors like the laser energy, an effective probe volume, the fluorescence detection solid angle and detection sensitivity must be known prior to measurements. Careful calibration measurement is the only way to minimize measurement errors and thus great care must be taken to ensure that the calibration measurement is performed under similar conditions as the actual measurement. Calibration object such as McKenna burner or Wolfhard-Parker burner can be used as a object for calibration of flames.

3.3 Criteria for Line Selection

In reality, each of the two electronic states is distributed over several vibrational and rotational sub-levels as illustrated in figure 3.1. After excitation to a particular sub-level in the upper state the population is redistributed to neighboring sub-levels, before returning to a sub-level in the ground state. The global fluores-

cence intensity detected over a large band is also dependent on the concentration at the lower sub-levels. The ratio of the number density of molecules in the lower rovibronic level to the total number density, n, is defined by the Boltzmann fraction which is a function of temperature (see equation 3.15).

If the fluorescence intensity is to be proportional to the total concentration of the species and independent of temperature it is necessary to pump a sub-level for which the relative population is nearly constant over the temperature range expected in the measurement volume. This is important in the combustion flame as the temperature ranges from 300K in the incoming fluid to as large as 3000K within the flame. Thus, with proper selection of the transition, the Boltzmann fraction will be nearly constant over the range of temperatures encountered in the focal volume, making the number of photons captured by the detector proportional to the total number density and the lifetime only.

$$n_j \propto n \frac{g_j e^{-\varepsilon_j/kT}}{\sum_j g_j e^{-\varepsilon_j/KT}} \tag{3.15}$$

where n_j is the number density of particles in the j^{th} energy level j; n , the total number density; k, Boltzmann's constant; T, the temperature; and g_j, the degeneracy of the j^{th} energy state.

3.4 Quenching Correction in Combustion Flames

The main challenges in obtaining reliable quantitative LIF measurements are calibration of the optical detection system, fluorescence quantum yield determination and assessment of various radiative and non-radiative processes associated with LIF. In order to determine the concentration from the fluorescence signal, the dependence of the fluorescence signal on collisional quenching must be eliminated i.e by evaluating the lifetime term ("τ_l") in the equation 3.14. It is the quenching rate "term Q_{21}" that complicates quantitative LIF measurements in flames: it depends heavily on the collision environment, the state of the probed quantum level and the temperature. The fluorescence signal can be corrected from collisional quenching either by monitoring the quenching environment, measurement in a calibration flame and by computing the correction term from available literature for a given species.

Among above mentioned ways to acquire the quench-free fluorescence signal,

the calibration method is very common and attractive. Calibration issues have been solved by:

- simultaneously measuring LIF signal from the same molecule at known concentration CH_2O [30]
- comparing the LIF with that from a different molecule with similar properties and known concentration
- the measurement of major species via simultaneous measurement of single-shot Raman/Rayleigh/LIF provides the necessary information on local quenching environment for OH and NO molecule, and hence number density of the radicals can be evaluated [31], [32]
- measuring the column density by absorption and combining it with the path length to normalize the LIF signal [33]

Other techniques such as laser saturated fluorescence [34] and pre-dissociative LIF with Raman scattering [35] were also used to quantify LIF signal.

Numerical modelling of the lifetime can be applied to correct the LIF signal for recovering species-concentration information. One such simulation model based on a kinetic-rate equation model for detailed energy transfer known as LASKIN [36] may be used to describe the collision dynamics for the OH molecule [37]. Other simulation techniques are also available, which help in approximating the signal intensities for several combustion-relevant species [38]. Modelling of lifetimes requires knowledge of the local temperature, all major species concentrations (the primary collision partners), and species and temperature-dependent quenching cross sections. Lifetime better than ± 20 percent can be estimated from the literature available for hydroxyl molecule at flame temperatures. Insufficient information on collision partners and other information result in worse estimation for molecules such as CH and HCO [29].

Short pulse diagnostics offers attractive alternative: If LIF is excited with a laser pulse of a duration of less than typical collision times (100ps) and an appropriate fast detection system is used, quench free measurement can be realized [26]. After interaction with a laser pulse of duration τ, $n_2^0(\tau_l)$ molecules are excited into the upper state. After the excitation the upper state population and therefore the fluorescence signal F will change temporally according to:

$$N_2(t) = n_2^0(\tau)e^{-(A_{21}+Q_{21})t} \tag{3.16}$$

By observing this exponential decay of the fluorescence signal using a suitable rapid detection system and extrapolating it backward to t=0, it is possible to determine the lifetime and the initial number density of the excited molecule that is not effected by quenching.

3.5 Short Pulse Diagnostics (PITLIF)

As mentioned above, short pulse diagnostics is an attractive method to realize a quench-free LIF measurement in combustion environment. In application to low pressure flames, the exponential decay of the fluorescence can be deduced from the nanosecond pulses because the pumping time of the species can be longer than the duration of the laser pulse.

Although in atmospheric flames where the natural lifetime of the species is of the order of several tens or even a hundred nanosecond, a nanosecond laser pulse does not provide sufficient resolution. Typical collision times in atmospheric flame is of order of 10-100 ps and with a nanosecond pulse excitation, many collisions occur before the photons are emitted. Collision between the species adds to the loss in fluorescence signal because of the emission less transfer of energy [39].

This can be resolved by using a picosecond laser pulse which has a temporal width significantly shorter than the lifetime of the molecule at the excited state. Detailed information and characterization of short pulse laser is provided in several reviews [26]. After excitation from the picosecond laser pulse, the fluorescence signal that decays exponentially must be sampled fast enough. Photomultiplier tubes (PMT's) are inexpensive, easy to use and reliable detection systems normally used that can resolve such fast fluorescence decays.

One such facility based on a short pulse diagnostics known as picosecond time-resolved laser-induced fluorescence (PITLIF) was developed at the Purdue University (U.S.A) [40]. Picosecond time-resolved laser-induced fluorescence is a technique that combines time-series measurements of the fluorescence signal with simultaneous quenching measurements to construct a quantitative concentration time series from the minor species such as Hydroxyl [OH], Methylidyne [CH],

Nitric Oxide [NO], etc. in laminar and turbulent flames. The information on the development of this technique is available in the thesis of [41], [42],[43]. This work utilized this experimental set-up to measure the scalar fluctuation in turbulent flames and its statistics.

3.5.1 Theory

The equation of LIF evaluated in section(3.1) still holds, as the fluorescence process via laser excitation is same. Specific knowledge of the PITLIF laser can now simply be introduced to the equation 3.3. In particular, the laser used is a high repetition rate, picosecond duration pulsed laser. This implies that the fluence (J/cm2) per pulse is low (since pulse energy and repetition rate cannot both be high). As a result of this low pulse energy, the number density within the excited level will remain small and the product $n_2 b_{21}$ will be especially small; thus, it can be neglected relative to the terms $n_2 A_{21}$ and $n_2 Q_{21}$. Moreover, since the duration of the laser pulse is very short compared to the typical time required for excited state decay via spontaneous emission and electronic quenching, the excitation process and the decay process can be separated into two differential equations. The result of this analysis is equation 3.6 and equation 3.17.

$$n_2(t) = n_2^0 exp(-t(A21 + Q21)) \tag{3.17}$$

where equation 3.6 describes the excited state number density just following the laser pulse (of duration t). Finally, the rate at which fluorescence photons are collected at the detector, dF/dt, is derived from the spontaneous emission rate and the excited state number density [see equation 3.13]

While the excitation process is essentially monochromatic, RET causes the fluorescence signal to occur over approximately 20-30 nm (the spectral width of the vibrational band)[see figure 3.1]. If all of this fluorescence is not captured, the measured lifetime can differ from its actual value and the SNR will decrease because of a lower photon count. If the entire vibrational band is collected, then the simplified two-level model adequately describes the fluorescence process. Next section will describe the method to calculate the lifetime and number density from a single exponential decay.

3.5.2 Measurement of Exponential Decay

One of the easiest methods to capture the exponential decay is Direct Current Sampling (DCS), that involves direct sampling the current from the PMT. If the sampling device is fast enough, individual decays can be resolved. Once the decay is captured from the PMT output, a fitting curve could be generated from the sampled results. This fitted function will provide the information on total number density that is not effected by quenching. This method has been used for the previous PITLIF measurements of [44]. However, the temporal resolution is limited by the maximum sampling rate of the detection system. Thus the primary limitation of this technique is its inability to collect such data long enough to recover any useful turbulence statistics. Inability to resolve the decay with good temporal resolution remains to be the major drawback for above mentioned detection technique. In other words, application to turbulent condition with the DCS detection scheme is restricted.

Time-correlated single photon counting (SPC) is perhaps the most popular technique [42],[45] for lifetime measurement from the registered exponential decay. The signal-to-noise ratio from the detection system is excellent, the temporal resolution is superb, and the data reduction is fairly straightforward. The complete exponential decay is registered by building the histogram from the pulses that are sorted out according to their height. Each pulse height is proportional to the delay between the start pulse (often output from photodiode in laser path) and stop pulse (output from photomultiplier).

For SPC measurements, the output of the PMT that is able to capture single photon event, is usually directed into a time-to-amplitude converter(TAC). The TAC also receives a start pulse from a photodiode in the laser path and outputs a pulse of which the amplitude is proportional to the delay between the start and PMT (stop) pulse. These pulses are then counted with pulse-height discriminators and are sorted into a multi-channel analyzer (MCA) according to their height (which corresponds to the photon arrival time after the laser pulse). The resulting array represents the PDF of first-photon arrival times [45].

Gated photon counting techniques share many similarities to time-correlated single photon counting in that the photon counts from the PMT are distributed into bins which build up the fluorescence decay [see figure 3.3]. The main difference lies in the fact that single photon counting technique is assumed of regis-

tering a single photon per laser pulse, which is not the case with gated photon counting technique. This is because time-to-amplitude converter is replaced by a double-balance mixer (DBM) and a trombone delay line placed in line of the laser photodiode path.

Both the PMT output and the photodiode output are applied to the DBM, which will only output the pulse if both pulses are present. This effectively gates the fluorescence photons based on the arrival of the laser PD pulse. By scanning the trombone line and recording the delay along with the DBM output pulse rate, the fluorescence decay can be constructed. This technique is not limited to only one collected photon per pulse [40]. Alfano [46] describe a system for gated photon counting and discuss many of the advantages over SPC.

Photon counting system captures the decay signal from LIF into a set of bins that are temporarily delayed with the help of coaxial delay cables of varying length as can be seen from figure 3.3. A fit is generated from total number of photons stored into separate bins to reproduce fluorescence decay and properties such as total number density and lifetime is evaluated from the rapid lifetime determination (RLD) algorithm. The instrumentation based on gated photon counting technique that captures the complete decay is detailed in the chapter 5. The line diagram of the photon path inside the instrumentation and also the method the photons are stored into the each individual delayed bins is explained in the section(5.1.4) of the same chapter.

3.5.3 LIFTIME

The novel technique LIFTIME was modelled based on the algorithm from ashworth's rapid lifetime determination (RLD) technique. The RLD method determines the peak decay amplitude and the fluorescence lifetime by calculating the ratio of two integrated areas under the fluorescence decay. This method computes the lifetime from algebraic equations based on this fluorescence ratio has advantage of being faster and using less computational power. This technique exploits the fact that a fluorescence decay is often a well-defined system, so only two points on the decay are necessary to describe the lifetime completely [47]. These two points often are referred as the storage bin for the incoming photons. Therefore in RLD technique only two bins were used to register the incoming photons.

Lytle *et al.* [47] used this algorithm for on-the-fly correction of fluorescence lifetime from two-point decay measurement. They used a two-channel sampling oscilloscope to acquire simultaneously two values on a fluorescence decay generated by pulsed laser excitation. The error analysis of this technique and its comparison with weighted linear least-square (WLLS) method was determined by Richard.et.al [48]. Precision of the RLD was undertaken in the same study by two independent methods, error propagation and numerical (Monto Corlo) simulation. RLD was found to be tens to hundreds of times faster than the WLLS method, depending upon how the data are taken. RLD with two integrated bin system cannot be used without significant errors, given an signal background. This restricts the application of RLD technique in combustion flames, because flame environment often consists of large flame-emission background.

The LIFTIME improves on the RLD method by adding a third integrated bin capable of directly monitoring the background. This improvement permits the application of LIFTIME in combustion flames, without additional losses. Figure 3.3 depict the three-bin arrangement for LIFTIME.

If the widths of the three areas are chosen to be the same (a condition that is easily attained in the experiment), the fluorescence lifetime, peak amplitude, and background can be found from

$$\tau_l = \frac{\Delta t}{\ln[\frac{(D_2 - D_3)}{(D_3 - D_4)}]} \tag{3.18}$$

$$B = \frac{D_2 C^2 - D_4}{\Delta t (C^2 - 1} \tag{3.19}$$

$$A = \frac{D_2 - B\Delta t}{\tau_l (1 - C)} \tag{3.20}$$

where τ_l is the fluorescence lifetime, B is the background, A is the amplitude of the fluorescence signal, t is the width of each integrated bin, and C is defined as $C = exp(-\Delta t/\tau l)$ for convenience. These equations have been derived by pack. et al. [42] by neglecting the instrumentation response from the PMT and by assuming that the background is constant (i.e., not correlated with the laser pulse). Figure 3.3 shows the measured impulse response for the PMT.

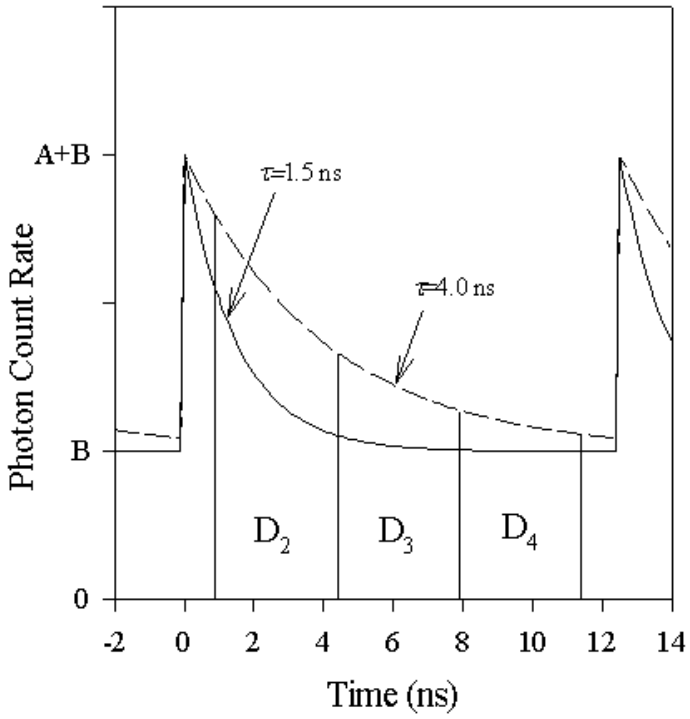

Figure 3.3: PMT impulse response function as compared to a typical fluorescence decay. The areas D2, D3, and D4 represent integrated measurements of the gated photon-counting system. D1 represents the total integrated fluorescence signal (0 to 12.5 ns). The background, B, is typical of flame emission, and the amplitude, A, is proportional to concentration

3.5.4 Quantitative time-series

The photon counting system summed the counts in each bin for a specific period of time, the inverse of the sampling rate. This results in recording of separate time-series of these three accumulated counts from each individual bins. The system is capable of sampling rates up to 500Hz and can record up to 8192 sequential points in a single time-series.

All our measurements were carried at sampling rates of 2 KHz and 4096 points were recorded in a single time-series. The bin counts were also used to determine the fluorescence lifetime, flame emission background and species concentration at each point from the software [40].

4 Applied Studies on Turbulent Flames

This chapter provides the introduction and mathematical description of important flame characteristics that have been investigated in this work. Significance of investigated physical properties for the description of flame physics under turbulent environment, are also discussed. Flame characteristics are catalogued and distributed according to the type of laser induced fluorescence measurements (single-point or planar measurement).

Initial sections are devoted to the parameters that are investigated using single-point LIF and planar LIF measurements respectively. More specifically, first section describes information on single-point quantitative scalar time-series measurement using time-resolved pico-second laser induced fluorescence (PITLIF) on turbulent opposed jet flame. Next section elaborates the flame characteristics evaluated from 2D planar LIF measurement on turbulent opposed jet flame and swirl jet flame measurements. Last section provides information on investigated molecule and their significance as a suitable flame front marker in the reacting flow.

4.1 Single Point Measurement

4.1.1 Time-resolved measurement: OH-PITLIF

Minor-species concentration measurement in turbulent flames have been of great interest, owing to their importance in pollutant chemistry and their use as a flame front marker. Normally, accurate predictions of scalar single-time statistics (mean, variance and PDF) are sufficient for most engineering applications. However in turbulent applications, more information extracted simultaneously in short temporal and spatial scale are important for the better understanding

of turbulent flames and the behavior associated with the turbulence-chemistry interaction. Simultaneous measurement of minor-species concentration and its fluctuations (time-resolved data) would be more beneficial. Such measurements will help in providing detailed insight on the flame front dynamics, minor-species concentration fluctuation and the information on extinction phenomenon. Additionally, the outcome may be used to test the numerical models capability, which are normally limited to predict only the average values of the scalar or limited to higher moments of the scalar distribution [49].

Fluorescence concentration of a scalar, when measured at high repetition rate with respect to time can provide the simultaneous information on its intensity fluctuation and concentration at the measured location. Additionally, scalar time-series can be constructed from such measurements that can provide insight on concentration correlation and power spectra of the fluctuating scalar in turbulent flames.

Time-resolved information can be provided by scalar time-series when measurement repetition rates are sufficiently fast to resolve turbulent fluctuations. For that purpose a laser with a high repetition rate, or alternatively a continuous laser, is needed. However, high repetition rate lasers generally have low laser pulse energy, which limits their use to point measurement techniques. For measurements in a point, where low laser energies are sufficient, measurement of temporal correlations in turbulent flames have been demonstrated for velocity [50] and many scalars, including temperature [51], chemiluminescence [52], and minor-species have been reported [53],[54].

In the current study, PITLIF (Pico-second time resolved LIF) have been used for the hydroxyl time series measurements for the first time in turbulent opposed jet flames. This technique seeks to combine LIF measurements with the capability for on-the-fly quenching corrections, yielding a time series of quantitative concentration measurement [40]. These measurements were done in collaboration with Mechanical Engineering Department of Purdue University (USA).

4.1.1.1 Time-Series

Registering the flame emission or any specific species as a function of time will result in time series. It provides an idea on the dependency of the next measurement, with the one which is measured before. For example, time series of

a constant signal will result in a straight line, when the signal value is plotted with respect to time. This means that the measured signal at any specific time for the above condition will have a same value as the previous measured value. This may be the case when the time series from flame emission or any excited scalar is detected from a laminar flame. However, in turbulent environment the time series may be very fluctuating and the measurement made may not have the same value as measured before. In other words, the two measurements taken at any instant of time may not show self-correlation.

Minor-species quantitative time series measurement in turbulent flames normally involves averaging of the instantaneous concentration over a period of time that is smaller than the smallest temporal scale, and reporting this average continuously for a period of time sufficient to capture the largest scale of the fluid flow. At single location, fifty time-series of 60 sec were collected at random to produced clean statistics from the turbulent opposed jet flame. Each time-series consists of 4096 points.

4.1.1.2 Autocorrelation and Integral Time Scale

The autocorrelation function reveals how correlations between any two values in the corresponding time-series change with temporal separation. The general formula for two point spatial and temporal correlation term in a three dimensional turbulent flow, is formally defined by (eq.4.1).

$$R_{i,j}(\overrightarrow{x}, t, \Delta\overrightarrow{x}, \Delta t) = \overline{u_i'(\overrightarrow{x}, t) u_j'(\overrightarrow{x} + \Delta\overrightarrow{x}, t + \Delta t)} \tag{4.1}$$

Where i and j are the dimensions of the vector that varies from 1 to 3 and u is the velocity term. If the temporal correlation is considered, that means correlation equation for same spatial location ($\overrightarrow{\Delta x} = 0$). The equation is reduced to:

$$R_{i,j}(\overrightarrow{x}, t, \Delta t) = \overline{u_i'(\overrightarrow{x}, t) u_j'(\overrightarrow{x}, t + \Delta t)} \tag{4.2}$$

Normally autocorrelation is normalized by the mean fluctuation component. And, if it considered for a single point measurement and only a function of time difference. Then the eq.4.2 can be rewritten as:

$$\rho(\Delta t) = \frac{\overline{u'(t)u'(t+\Delta t)}}{(u'_{rms})^2} \tag{4.3}$$

and Integral time scale τ_I, which represents approximately the largest time over which fluctuations are correlated is given by eq.4.4.

$$\tau_I = \int_0^\infty \rho(\Delta t) d\Delta t. \tag{4.4}$$

If fluctuation from a scalar is considered, as in our case where the hydroxyl molecule is the investigated scalar, the velocity fluctuation term is replaced by $[C_{OH}]$ resulting in a new set of equation for single-point auto-correlation and the integral time scale (eq.4.5)-(eq.4.6). Where $[C_{OH}]$ is the concentration of detected molecule, in our case it is hydroxyl.

$$\rho(\Delta t) = \frac{\overline{[C_{OH}]'(t)[C_{OH}]'(t+\Delta t)}}{([C_{OH}]'_{rms})^2} \tag{4.5}$$

$$\tau_I = \int_0^\infty \rho(\Delta t) d\Delta t. \tag{4.6}$$

Where $[C_{OH}]' = [C_{OH}] - \overline{[C_{OH}]}$ is the fluctuating part of the time series, and root mean square value $[C_{OH}]'_{rms} = \sqrt{\overline{[C_{OH}]'^2}}$.

4.2 Multi-dimensional Investigation: 2D Planar

For viewing effects of turbulence-chemistry interaction and to provide structural data on the flame sheet in the view of LES validation, wrinkling and location of the mean reaction zone, spatial extension of the reaction zone and of regions containing hot combustion products are some of the most important parameters. Two applications of flame front topology using the two-dimensional planar technique have been identified, first is to visualize the location of instantaneous stoichiometric contour in turbulent opposed jet partially-premixed and non-premixed flames. And secondly, to visualize the position of peak heat release rate in more technical relevant swirl stabilized lean premixed flame. Other flame front characteristics were also evaluated and studied in these flames in order to build a data base for numerical model validation.

4.2.1 Flame-front Topology

The flame-front or the reaction zone in turbulent reacting flows is defined as the region where chemical reactants involving fuel and oxidizer reacts to form combustion product, thereby releasing maximum energy. Several studies have been motivated in the past decade on visualizing and identifying the accurate location of reaction zone in combustion. Research in this field was fuelled by the identification and detection of several intermediate species that occur near the reaction zone.

It is known that direct measurement of the instantaneous flame-front location is difficult, rather flame-front detection has been relied upon identification of species existing near flame reaction zone. Such measurement were difficult due to the reason that no single species can mark the entire fuel decomposition zone, which depends on all of the relevant radicals (CH_3, CH_2, CH, HCO, etc.). Thus proper choice of the species for the flame-front identification is an important task for the success of such measurement. Various chemical (chemiluminescence, LIF etc.) and physical quantities (dilatation rate) were used to localize the flame-front in unsteady reacting flows and have been documented. Various flame-front markers include OH, CH, HCO, HCHO, OH*, CH*, C_2* and dilatation rate represented by $\Delta.v$.

In non-premixed flames the reaction zone is identified as region existing between fuel and oxidizer. In such flames, the location of reaction rate is attached with the zone of stoichiometric condition. Therefore, most of the time reaction rate have been predicted just by imaging the species that accurately predict the location of stoichiometric contour. Simultaneous scalar imaging of OH/CH PLIF [23] or OH/CO LIF [18] was used to study the reaction rate in a piloted CH_4/air jet flame. Same paper also utilized polarized Rayleigh scattering to register field image of temperature, which was used to correlate the results with reaction rate location.

In premixed flames the reaction zone is the area differentiating between burned and unburned region. Also, the location of reaction zone is no longer attached with the zone of stoichiometric condition and combustion occurs by the propagation of reaction front through the turbulent flow. Therefore to identify the location of reaction zone, a different approach was proposed by Paul *et al.* [55], which will be detailed later in this section.

Very less research have been done for the partial-premixed flames in terms of predicting the location of reaction zone. Studying partially-premixed flames is important regarding the fact, that it could provide insight on the transition between partially-premixed and non-premixed flames. This information could be useful to understand the physical behavior of such flames. Present work tries to extract the position of stoichiometric contour from planar laser induced fluorescence (PLIF) measurements that are applied to the turbulent opposed jet flames ranging from premixed to partially-premixed mode.

4.2.1.1 Visualization of Instantaneous Stoichiometric contour

Information on the location of instantaneous stoichiometric contour in turbulent opposed jet flames (section: 7.5.1.3) is of special importance, because along this contour it is useful to know the value of certain quantities such as scalar dissipation rate and the strain rate. Such measurements are complex to pursue due to the fact that the reaction zone remains thin and rarely exceeds 1 mm. Simultaneous measurement of two or more species that occur near the reaction zone is another complex procedure, time consuming and costly.

The molecules, namely CH and OH were previously simultaneously imaged in turbulent jet flames by Donbar *et al.* [23], for the purpose to visualize the instantaneous stoichiometric contour. It was found that the boundary between OH layer (lean side) and CH layer (rich side) was found to be a very good marker for visualizing stoichiometric contour. However, they proposed some caution during interpretation of CH and OH images, especially in high turbulent flames and the locations where the flame is locally extinguished. This is because CH yields erroneous results near the locally extinction zone and it is not known if the entire flame is extinguished or if only the reactions involving CH have extinguished.

In non-premixed jet flames, CH is helpful in complicated flow environments for a distinction between the OH formed in the reaction zone itself and regions of hot combustion products where OH exists because of the thermo-chemical equilibrium with water. In contrast to co-flowing jet flames and more complicated flows, in the counter-flow configuration oxidizer and fuel approach the shear layer with opposed flow directions, allowing a definite discrimination between the flame contour and reaction products. The OH surface on its own is therefore

a reasonable marker to identify the structure of the stoichiometric contour in counter-flow configuration.

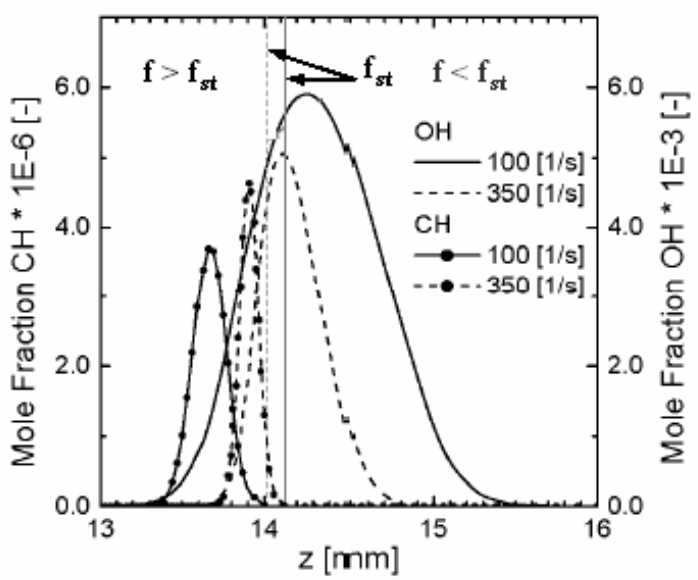

Figure 4.1: Profiles of OH and CH mole fractions calculated from laminar opposed jet flames using flamelet theory. Results are shown for strain rates of 100 and 350 s^{-1}, respectively. Solid lines denote $a = 100s^{-1}$, dashed lines $a = 350s^{-1}$. CH is represented by additional symbols. Vertical lines denote the location of stoichiometric mixture fraction (f_{st}) and f is the mixture fraction. The stagnation plane for this counter-flow configuration lies at z = 15 mm.

This statement is even more supported by the calculation of spatial hydroxyl profile of laminar opposed-jet flames using flamelet theory. I am much obliged Prof. J.Y.Chen for providing data on laminar opposed jet calculation. Hydroxyl profiles were computed for a partially premixed fuel with $\phi = 2.0$ and strain rates of 100 and $350s^{-1}$respectively, are shown in figure 4.1. Strain rate is calculated as the ratio velocity to the distance between the nozzles. Corresponding stoichiometric positions (f_{st}) are marked by the vertical lines and f is the mixture fraction. For this configuration, z equal to 15 mm is the location of the horizontal stagnation plane between the opposed nozzles. The lower nozzle (fuel side) is situated at z equal to 0, whereas the upper nozzle (air side) is located at z equals 30 mm.

For $a = 100s^{-1}$, the onset of the OH slope (mole fraction $\geq 1 \times 10^{-3}$) on the fuel rich side is 0.57 mm displaced from the stoichiometric point. With increasing strain this displacement reduces remarkably. For $a = 350s^{-1}$ the displacement is less than 0.25 mm. Thereby, the lower contour of the hydroxyl profile only is a reasonable marker of the stoichiometric contour. Notice that in the experimental set up described in chapter 7, this OH onset corresponds to the fuel side contour line monitored experimentally. In turbulent opposed flames the OH maximum is believed to be a marker less reliable than the onset because super-equilibrium concentrations [6] of OH due to turbulent transport might affect the contour of the maximum rather than the onset of the OH concentration.

In turbulent opposed jet flames, parameter of interest also includes measurement of instantaneous spatial structures. Information on flame-front characteristics such as flame front wrinkling, area, length, spatial extension of the reaction zone and of regions containing hot combustion products were also investigated. These measurements were applied on turbulent opposed jet flames ranging from combustion mode of partially-premixed to premixed.

4.2.1.2 Visualization of Reaction Rate

Another and more recent application of flame-front topology was to predict the location of peak heat release rate in turbulent premixed flames. Studies showed that the peak heat release rate correlates well with the destruction rate of methane. Several species can be utilized to either correlate or track the destruction rate of methane during combustion. As can be seen from the reaction chain in the figure 4.2, destruction rate of methane can be determined by the formation rate of formaldehyde molecule in the stoichiometric methane-air flame (taken from [25]). Even the reaction rate of methyl radicals and oxygen atoms may be used to predict the heat release rate.

Finally, Najm [56] presented detailed chemical kinetic computations and experimental measurements in premixed methane/air flame, and studied the utility of several other species as the indicator of heat release rate. Signal from species * such as OH*, C_2*, CH*, CO_2*, OH and CH PLIF imaging were investigated. In the same paper, it was found that the formyl radical (HCO) concentration is also dependent on formaldehyde formation rate which correlates well with the

"X" indicates the chemiluminescence signal from molecule "X"

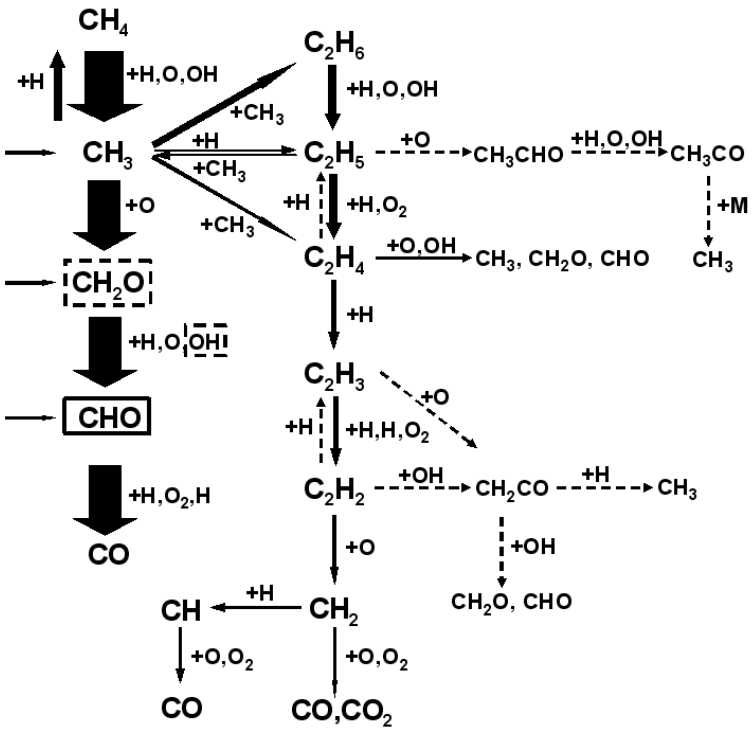

Figure 4.2: Reaction mechanism of methane/air stoichiometric premixed flame at P=1 bar and T=298 K. Production rate of formyl molecule [CHO] is associated with reduction of formaldehyde [CH_2O] and hydroxyl molecule [OH].

heat release rate. But, due its low abundance in the reacting flows, single-shot measurement of the HCO distribution using laser induced fluorescence is not feasible. Thus results have to be averaged in order to achieve good signal-to-noise ratio. The two photon excitation scheme of HCO molecules further increase the complexity for its easy detection.

Instead, Paul [55] showed that the product of hydroxyl (OH) and formaldehyde (HCHO) concentration is directly proportional to the reaction rate $HCHO + OH \rightarrow H_2O + HCO$ and, therefore, yields an estimate for the production rate of HCO. This reaction proceeds at a forward rate proportional to $RR \propto n_{OH} n_{HCHO} k_f(T)$, where n is the number density and k_f is a rate coefficient.

Same paper revealed that the product of hydroxyl [OH] and formaldehyde [HCHO] LIF signals taken at the same spatial location may be written as $Si_{OH} Si_{HCHO} \propto n_{HCHO} n_{OH}$ g(T), where g(T) is a known function of temperature. Over a limited temperature range, transitions can be properly selected such that g(T) sufficiently

mimics k_f(T). Due to the high abundance of HCHO and OH molecules near the flame front region and their large fluorescence cross-sections, this approach enables single-shot measurements in the highly turbulent reactive flows.

Recently, Fayoux *et al.* [57] also confirmed that the product of the molecule yields a result closely related to the heat release in counter-flow laminar flame. Stefan [24] applied the simultaneous single-pulse imaging technique of OH, HCHO and temperature in a bunsen burner and a turbulent swirl flame. It was shown in the same work that the product of OH and HCHO LIF signal closely follows iso-lines within the temperature field. Which justifies the neglect of the influence of temperature on the fluorescence intensities and the direct use of the product of the LIF intensities instead of the product of concentration [55]. All above mentioned comparison lead to the conclusion that the experimental imaging of simultaneous OH and HCHO molecule via planar laser induced fluorescence, seemed to be a reasonable tool for the identification of peak heat release location in the turbulent flame.

A part of the thesis is motivated from the work from Paul.et.al and thus, reaction zone imaging using simultaneous OH/HCHO PLIF on technical relevant turbulent swirl premixed flame was realized in the Institute for Energy and Powerplant Technology (EKT).

4.3 Molecules Investigated

Theoretically, there are approximately 180 intermediate species taking part in combustion process but only few are accessible and can be detected using modern techniques. In turbulent combustion, selection of molecules to be investigated is driven by the following criteria:

- Its presence in significant amount during combustion
- Possibility of single-shot detection and state of art planar measurement (2D or 3D measurement)
- Its presence over a very large temperature range
- It should be easily accessible with existing and cheap laser systems
- Detection scheme must not be very complex

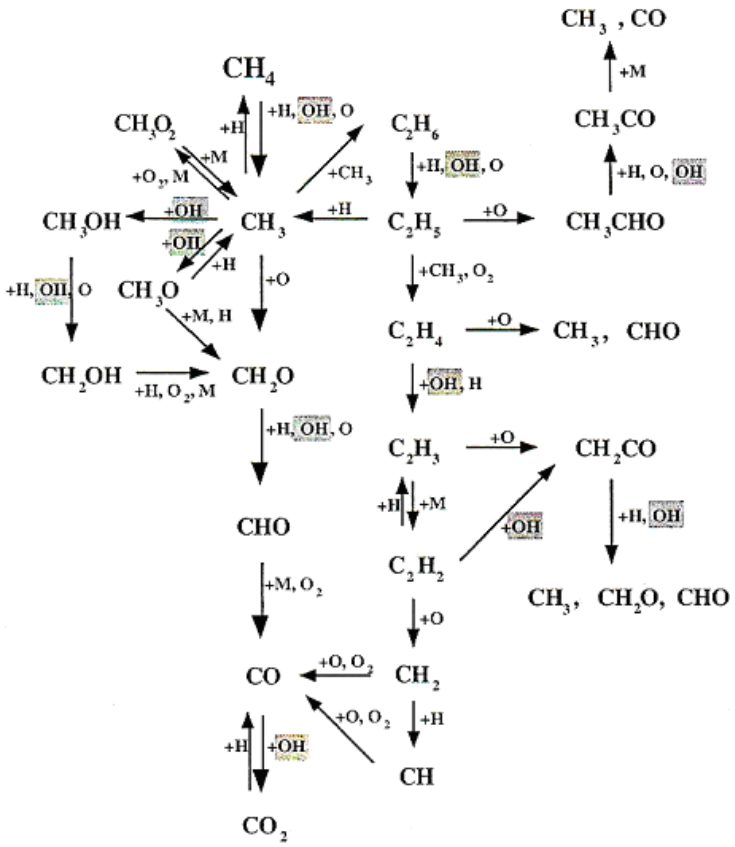

Figure 4.3: Oxidation of methane, showing the significance of hydroxyl molecule in the combustion process.

4.3.1 The Hydroxyl Radical

Hydroxyl is an important and most common intermediate species in combustion where oxygen as oxidizer is involved [58], as can be seen from figure 4.3. Same figure, as well depicts that the hydroxyl radical is involved in many reaction pathways, and also causes propagation in the oxidation process of methane. OH is formed by fast two-body reactions, such as the attack of H radicals on O_2 molecules, and is then consumed by slower three body recombination reactions. Such reactions are the primary sources of energy and involves three reacting species to successfully carry out the reaction. The probability of a three-body collision is small, therefore, recombination reactions are much slower than other

flame reactions. Radicals such as hydroxyl, therefore, relatively long-lived in a flame and may diffuse significant distance before they undergo reaction.

This long-living behavior was successfully utilized previously for analyzing turbulent flame structures, where a clear detection from pre- and post flame region is required. Additional properties such as occurring near the flame front, high concentration [ppm range] and high signal intensity in a flame makes it a favourable flame front marker. Also sufficient contrast (good signal-to-noise ratio) from higher spatial (2D or even 3D) topological measurement thus undoubtedly makes it a good choice for extracting information on spatial structures in a turbulent flame.

4.3.2 Formaldehyde

Formaldehyde is another important intermediate in the hydrocarbon combustion and has experienced growing interest in the recent years as an important molecular species to monitor combustion events. This interest is due to several reasons, on the one hand CH_2O is formed by oxygen attack on primary fuel radicals (e.g. CH_3) and, therefore is indicative as a center for the occurrence of oxidation reaction. It is destroyed by the hydrogen abstraction resulting in the production of HCO, another intermediate species that correlates best with the peak reaction rate in methane-air combustion [56].

In combustion, LIF measurement of native HCHO in the laminar Wolfhard-Parker slot burner flame was first reported by Harrington and Smyth [59]. This was followed by several studies for the detection of formaldehyde molecule (HCHO) using point and planar measurement techniques in combustion flames, both experimentally [60]-[66] and numerically [55],[67].

Also, formaldehyde is chemically very active species and spectroscopically accessed with ease in the near-UV spectral region using existing laser sources. At excitation wavelengths shorter than 290 nm, the dissociation phenomenon becomes so fast that the fluorescence is undetectable. Because of pre-dissociation, the lowest energy vibronically allows one-photon transition. $\tilde{A} - \tilde{X}4_0^1$, is the strongest fluorescence band. This band is well suited for diagnostics applications, extending from about 352 to 357 nm in the absorption spectrum [see figure 4.4] [68]. Some literature have also accessed the electronic band at 339 nm, which can be easily accessible from state-of-the-art tunable laser system.

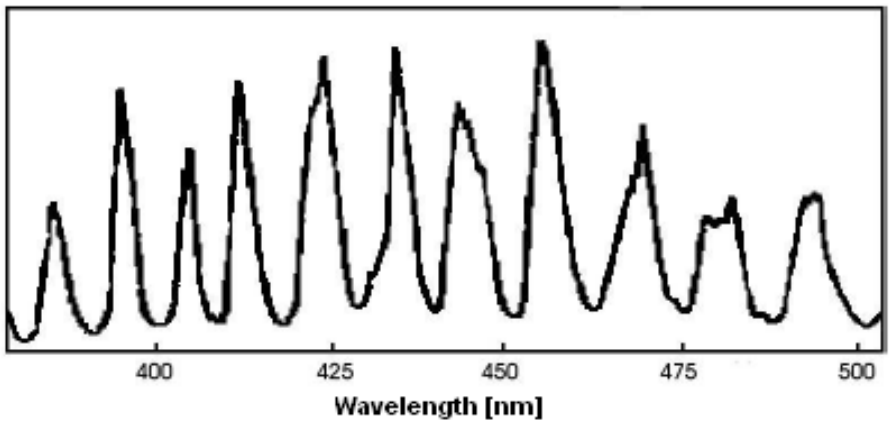

Figure 4.4: Emission spectrum of formaldehyde CH_20 taken from literature.

Two-dimensional imaging of HCHO in an spark-ignition engine has been reported by Bäuerle *et al.* [60] and Graf *et al.* [63]. In both cases, excitation via band $\tilde{A}^1A_2 - \tilde{X}^1A_1$ (near 353 nm) was chosen. Other excitation wavelength at 338 nm [30], or at 370 nm [64] were also used for various application in flames. These transition was accessed with a tunable dye laser pumped either by a XeCl excimer or an Nd:Yag pulsed laser. Not many literature have reported an excitation wavelength of 355nm, due to its weak excitation scheme. Even though the laser light at this wavelength is easily accessible using a non-linear crystal that generates 3^{rd} harmonic from an Nd:Yag laser. Recently, Fayoux *et al.* have measured planar laser induced fluorescence of formaldehyde molecule in a counter-flow premixed laminar flame by exiting it using laser light at wavelength of 355 nm [57]. We have also chosen this 355 nm weak excitation scheme for formaldehyde detection in the turbulent flames.

The emission spectrum of the formaldehyde molecule was determined in a laminar flame and compared with the available literature spectrum. The measured spectrum was found to match well with the literature spectrum. The details of the burner configuration, flame parameter and the location of measurement is provided in the next section. The emission spectrum from the flame was registered using point laser induced fluorescence and the signal was detected using a detected that was attached to the spectrometer.

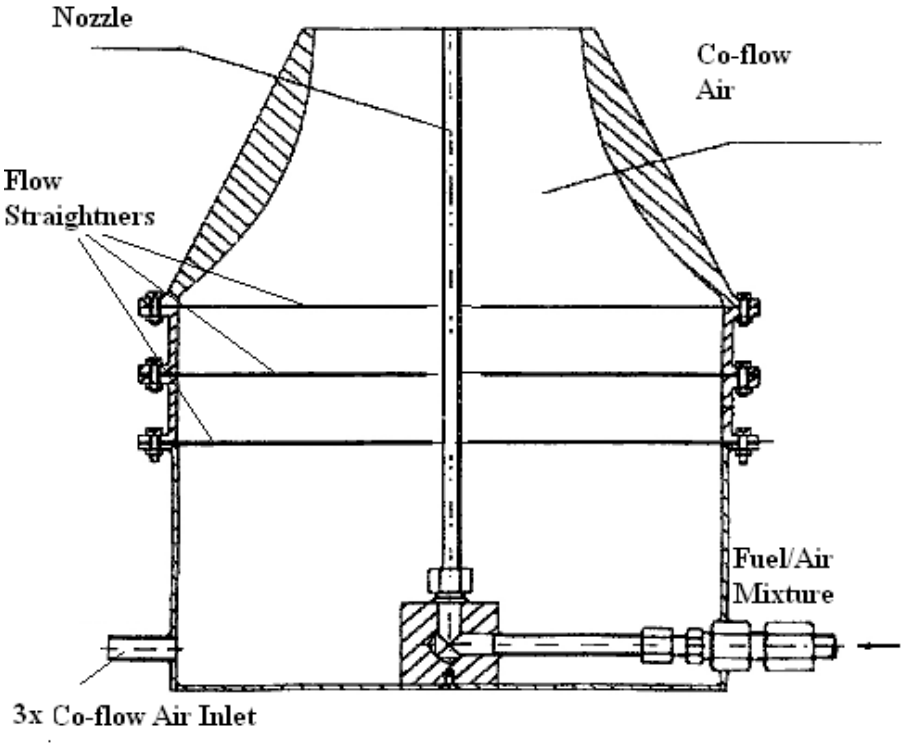

Figure 4.5: Schematic figure of EKT standard burner.

4.3.2.1 Burner Configuration and Flame Measured

Investigation and confirmation for the formaldehyde molecule was done in a laminar methane-air premixed flame from EKT standard burner. As can be seen from the figure 4.2, most of the carbon in the flame chemistry reduce through single C species and not through C_2 species at the stoichiometric mixture [25]. Also, the approximation that the simultaneous measurement of HCHO and OH molecule compares well with the local temperature gradient, is valid between $\lambda_B = 1.0$ to $\lambda_B = 1.2$ [55]. Therefore, flame with an $\lambda_B = 1.2$ was chosen for testing purpose.

A schematic of EKT standard burner with nozzle diameter of 11 mm, is depicted in the figure 4.5. A mixture of fuel and air flows through the center tube of 500 mm in length and the fluid exits at the nozzle end of 11 mm in diameter. The flame chosen was a laminar flame with Re=500, $\phi = 0.88$. The mass flow of surrounding co-flow (air) was 4800 lt/hr. The locations above the burner, where

the formaldehyde spectrum was taken using the point laser induced fluorescence technique are shown in the figure 4.6.

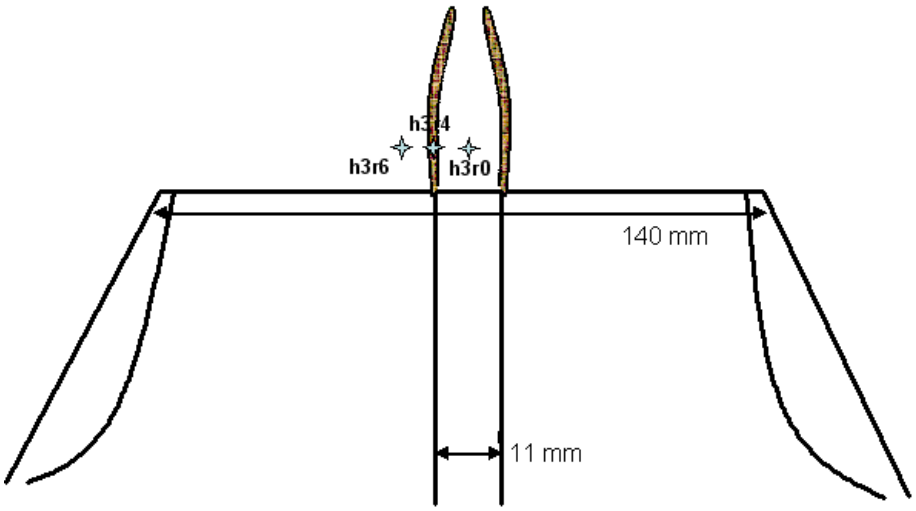

Figure 4.6: Location of point measurement for the formaldehyde spectrum in the standard burner, h is the height in mm and r is the radial distance from the center burner axis. h3r0 indicates center point at height 3 mm above the nozzle.

4.3.2.2 Spectrum Analysis

Figure 5.11 shows the result from the spectrum measurement of the formaldehyde molecule excited through a Nd:Yag laser beam at an excitation wavelength of 355 nm in a methane/air laminar premixed flame. A spectrum between 405-515 nm was captured through a two-dimensional charge coupled intensifier located at the exit of the spectrometer. The details on the experimental set-up and the equipment used for spectrum measurements are provided in chapter 5. The formaldehyde spectrum is reproduced very well in comparison with the literature spectrum shown in figure 4.4. The resultant profile is the result from the accumulation of 1500 single-shot spectrums acquired by the detector (ICCD).

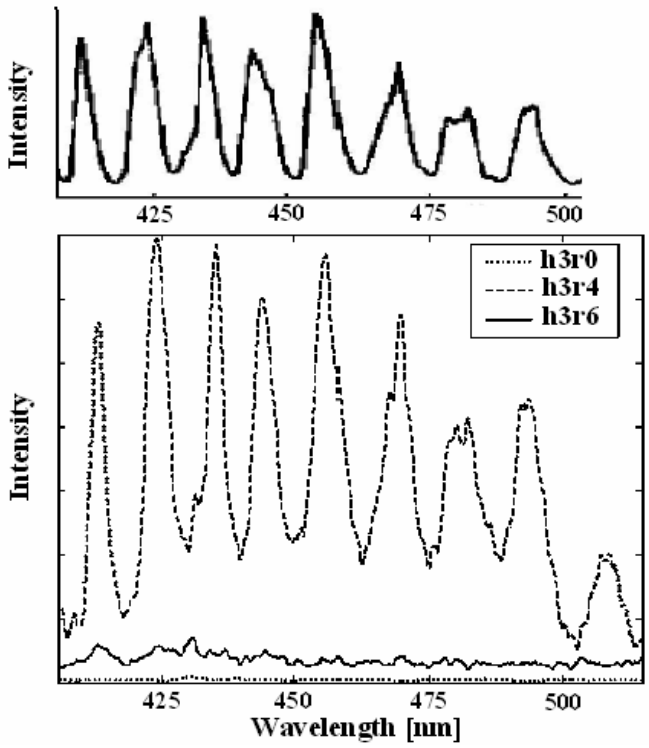

Figure 4.7: Measured spectrum from the formaldehyde in Methane/Air premixed flame at the locations given in figure [4.6]. Comparison of measured spectrum (lower) is shown with the literature spectrum (upper).

5 Experimental Methods

This chapter outlines the experimental methods utilized for the application of laser induced fluorescence (both point and planar technique) in the turbulent flame diagnostics. A detailed description is provided on the experimental set-up and the instrumentation required for the successful completion of experimental measurement.

5.1 OH-PITLIF in Opposed Jet Flames

5.1.1 Introduction

The PITLIF system consisted of a mode-locked laser and a photon counting system that records the individual fluorescence decay, with temporal resolution and bandwidth sufficient for time series measurement in turbulent flames. The PITLIF technique in combination with the time-resolved instrumentation, facilitates the registering of the exponential decay from the hydroxyl molecule during the emission process of laser induced fluorescence.

5.1.2 PITLIF Laser System

The lasers used in the PITLIF system are a large-frame Spectra-Physics argon-ion laser and a Ti:Sapphire * laser from Spectra-Physics. The Ti:Sapphire laser is pumped by the argon-ion laser and the output beam power of the argon-ion laser is tunable upto 25 W. A simplified detailed sketch of the laser system and the experimental set-up is illustrated in figure 5.1.

The Tsunami (Ti:Sapphire laser) is characterized by a typical laser cavity composed of Brewster windows, a two- or three-plate birefringent filter, a Gires-Tournois Interferometer (GTI) and a host of high precision mirrors and lenses.

*a regeneratively mode-locked

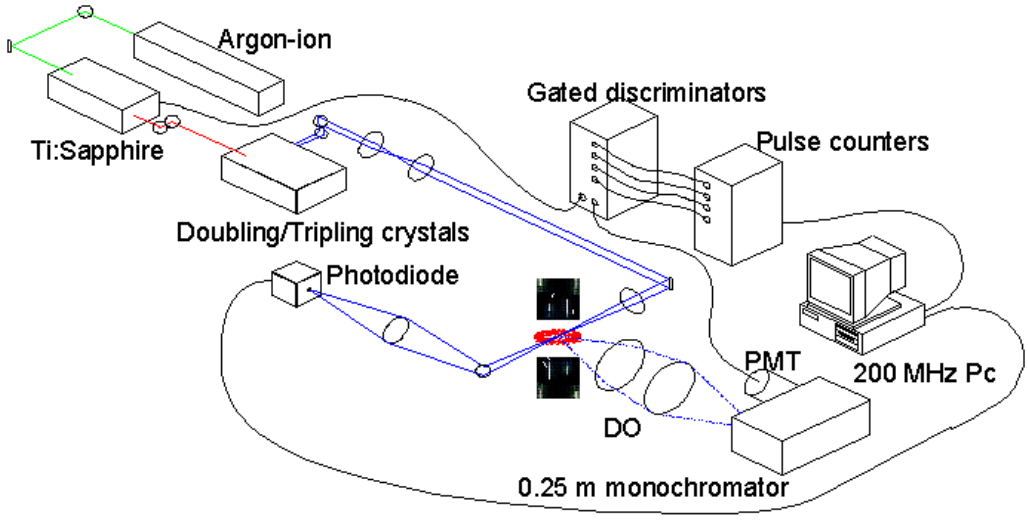

Figure 5.1: Experimental set-up of OH-PITLIF in opposed jet flames: DO, detection optics; PMT, photomultiplier.

To change the repetition rate of the laser, the cavity length can be adjusted by translating a mirror on a piezoelectric mount through a photodiode feedback loop. This controller can be locked to an input reference frequency, so that the repetition rate of the laser can be matched with that of any other laser or a characteristic frequency of the desired measurements. This controller can also be turned off and the laser repetition rate can be allowed to vary. The repetition rate of the laser during our measurements was set at 80 MHz.

The birefringent filter can be adjusted to give continuously tunable, low-IR radiation from 840 to 1000 nm. The cavity of the Tsunami laser is sealed and a nitrogen purge is constantly applied to reduce internal contaminants. Consequently, frequent cleaning is avoided and water vapour (with strong absorption lines around 940 nm) is continuously removed from the cavity. The typical output power of the Tsunami is 1.0-3.5 W for argon-ion pump powers of 12-25 W. The GTI provides an output temporal pulse width of 2 pico-second.

After leaving the Tsunami, the infra-red beam frequency is tripled to 306.5 nm for OH excitation via a CSK SuperTripler (Model 8312). The SuperTripler

consists of an LBO* doubling crystal and a BBO† tripling crystal. A polarization rotator is used after the Tsunami to ensure horizontal polarization before the beam enters the doubling crystal. To achieve a highly efficient tripled beam, the doubled beam from the LBO crystal and the residual fundamental beam must be focused and overlapped, in both space and time in the BBO crystal. The conversion process is non-linear and is proportional to square of the peak power in the doubling crystal and cubed for the beam from the BBO crystal. Hence a small change in the temporal pulse width of the laser beam can cause a very large change in the required UV. The beam from the SuperTripler is re-collimated by a pair of UV lenses, and focused by a 200 mm focal length, 50 mm diameter UV lens, through the probe volume. The focused beam was tilted at 20° angle from the horizontal plane to avoid beam steering. The laser beam is then dumped onto a photodiode (Thor-Labs $DET-200$), which records the average laser power. A 2 pico-second GTI was used for all measurements of OH reported. For this GTI, the average power at the probe volume varied from about 18 mW to 30 mW.

5.1.2.1 OH-Line Selection

Figure 5.2 illustrates a simulated excitation scan using the spectral code developed by Seitzmann for the actual spectral width of the Tsunami laser beam. This code accounts for all rovibronic lines in the $(0,0)$ vibrational band of the $X^2\Pi$ - $A^2\Sigma^+$ system of OH up to $j^{''}=90$. For each ground level, several transitions are available (Q-branch, P-branch, R-branch). Figure 5.2 depicts that the chosen transition $R_1(11)$ was selected for excitation of hydroxyl molecule. The ground level for this transition is properly chosen to minimize any dependence of the fluorescence signal on temperature fluctuations. For minimal temperature dependence, the Boltzmann fraction should be constant over the range of temperatures present in the flame. It can be seen from the figure that the variation of the chosen transition with temperature is negligible. Thus, fluorescence signal can provide the information on the number density of the investigated species. The best of these transitions is selected based on the strength of each transition and their isolation from possible interferences. The wavelength of the chosen excitation line is $306.5nm$.

*Lithium Triborate, nonlinear crystal
†Beta Barium Borate, nonlinear crystal

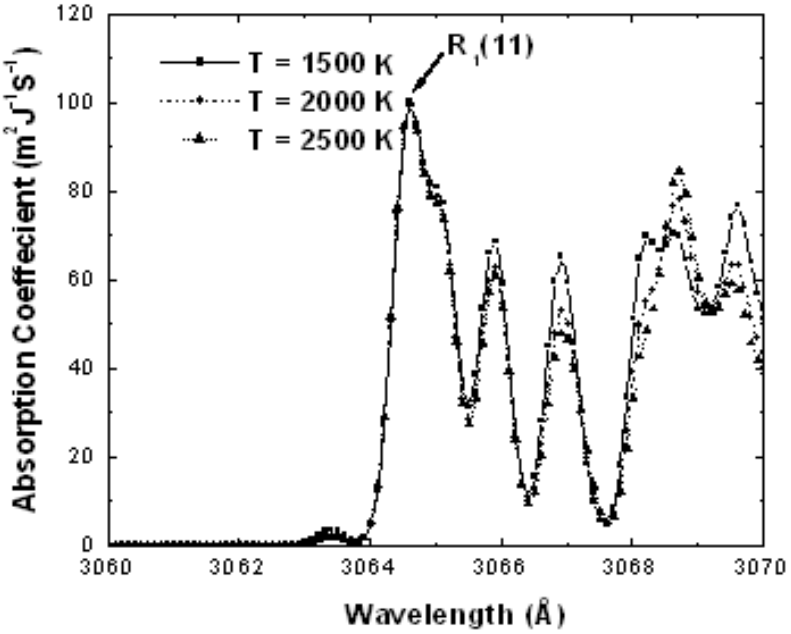

Figure 5.2: Simulated OH absorption spectrum as a function of temperature. The selected transition $R_1(11)$ is insensitive to the temperature range between 1500 K to 2500 K. Wavelength is depicted in Angstrom, visible light covers the range of 4000 to 8000 Angstrom. For hydroxyl molecule wavelength of 3065 was chosen, which corresponds to 306.5 nm.

5.1.3 Detection Optics

The arrangement of the detection optics for the PITLIF system is shown in figure 5.3. Fluorescence from the excited molecules was collected by a lens tilted at a 20° angle from the burner axis, which was at 90° to the incident laser beam. This was done to avoid viewing through the complete flame and hence reduce the background emission. The optimized detecting angle would be at 0° angle to the burner axis (bottom of the flame), but this was impossible. The focal length and diameter of the lens (L1) are 150 mm and 51 mm, respectively. A pair of mirrors reflect the collimated fluorescent rays onto a focusing lens. The diameter of the collimating and focussing mirrors was 51 mm.

The fluorescent rays were then focused onto the slit of a PTI $0.25-m$ monochromator using a lens (L2) with a focal length of 200 mm. An adjustable slit at the entrance to the monochromator allows the probe volume in the flame to be limited to specific dimensions. For the current measurements, the spatial resolution was $100 \times 100 \times 60$ μm^3 based on the beam diameter and the monochromator entrance slit width. The slit was aligned vertically to define the probe volume dimension along the laser beam path. The laser beam diameter itself defines the other two probe volume dimensions. The monochromator grating was blazed at 400 nm, 1200 lines/mm and can be rotated to scan the spectrum. For the hydroxyl measurements reported in this investigation, the slit was set to result in total bandwidth of 10 nm centered at 306.5 nm.

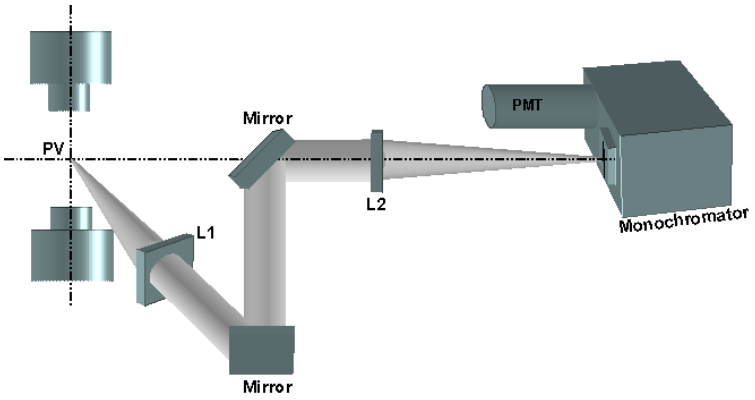

Figure 5.3: Detection side of the PITLIF set-up. FV is the focal volume and the location of measurement and L1, L2 are the detecting and focusing lenses respectively.

5.1.4 PITLIF Photon Counting System

This section describes the instrumentation that was designed after the success of gated photon counting technique that is explained in section(3.5.3). In order to register the fluorescence decay from the OH molecule in flames that is excited by the pico-second laser pulse, a novel photon-counting system and a fast PMT capable of monitoring single-photon events in the exit plane of the monochromator, is utilized. The detection scheme is based on the three-bin arrangement temporarily apart, that act as the detecting window for registering

the complete decay [see figure 3.3]. Decay from the radiating molecule is saved in these three bins and a fitting routine is applied to achieve the exponential function, which is further evaluated to get the total number density and lifetime of the molecule. Total counts in each bin, when registered with time, provides time-series measurement of the fluctuating molecule from the measured location.

A Hamamatsu HS5321 photomultiplier tube attached at the exit of the monochromator detected the fluorescence. The PMT was powered by a high-voltage power supply from Stanford Research Systems (Model PS325), which was set at -2500 volts. The HS5321 PMT has a rise-time of 700 ps and a transit time spread of 160 ps.

The wire schematic for the designed photon counting system is illustrated in figure 5.4 [42]. The output of this designed photon counting system is the information stored in three sperate bins delayed temporarily apart. The electronics from photon-counting system consists of two LeCroy model 4608C octal discriminators connected to four EGG Ortec logic-pulse counting boards. These two discriminators decide whether the pulse from the PMT is above the threshold and is detectable, whereas counting boards counts the incoming pulses and store in three separate bins temporarily delayed apart.

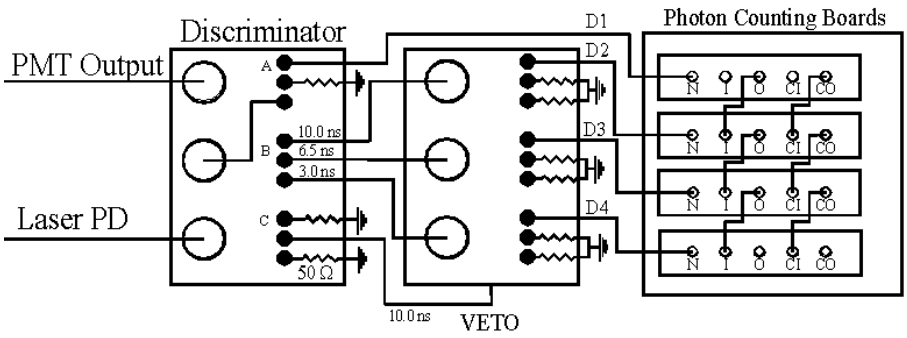

Figure 5.4: PITLIF photon-counting system. N is the NIM input from the discriminator, I is the start signal input, O is the start signal output, CI is the channel advance input, and CO is the channel advance output. Unused signals are 50-ohm terminated while 10.0, 6.5, and 3.0 ns represent the delays placed in each line.

The output from the photomultiplier tube (PMT) is directed to one of the discriminator channels and the output from photodiode (PD) of the laser is

directed to another that act as a trigger (start pulse) for the whole system. For each current pulse from the PMT, the discriminator emits a 5 ns nuclear instrumentation methods (NIM) pulse. Likewise, each cycle in the laser PD signal produces a 9 ns NIM pulse.

There are three NIM outputs for each discriminator channel. One of the three outputs is rerouted to the first photon counting board(A). The second output is terminated (50Ω) and the third is rerouted to yet another discriminator channel(B). This re-discrimination allows the NIM pulse to be amplified and split into three identical NIM pulses without causing any timing error. The three outputs are delayed separately (10 ns, 6.5 ns, 3 ns) with 50-ohm delay cables and are directed to three separate discriminator channels on the second octal discriminator. These delays cause the fluorescence decay signal to arrive at the chosen times so as to be gated simultaneously.

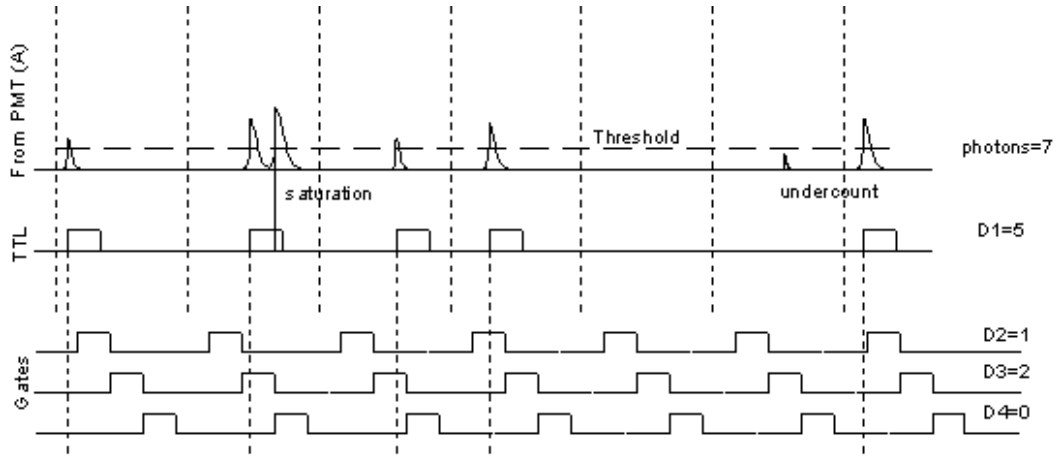

Figure 5.5: PITLIF Timing diagram. This shows the typical distribution of photons that arrive from the PMT and the way they are gated by the photon counting system. D1, D2, D3, D3 are the integrated temporal bins.

The second octal discriminator is gated by a VETO input. The VETO input is the 9 ns NIM pulse generated from the laser photodiode. The VETO line is delayed 11.5 ns to account for the difference in the PMT and laser photodiode cable lengths. This delay must be changed when the optical path length of the laser changes. The VETO input allows the second octal discriminator to output NIM pulses for only 3.5 ns.

The outputs of these gated channels are sent to the photon-counting boards and thus represent the integrated counts D2, D3, and D4 as can be seen from figure 3.3. The first photon-counting board (D1) is triggered to start the counting process. Once the first board is initiated, it sends a start signal to the second board. Likewise, the second board sends a start signal to the third and so on. D1 is the total decay which is the sum of D2, D3 and D4 respectively.

Figure 5.5 shows an outlined diagram for the timing of the PITLIF system. The PMT emits a pulse for every photoelectron detected. The pulse height typically is 20 mV but with obvious shot-to-shot variations. The arrival time of successive photons is not equal. Typically, a photon arrives at the PMT every six or seven laser pulses. In some cases, two photons may arrive at the same time. As a result, the discriminator counts them as a single pulse thereby reducing potential counts in the corresponding bin. Sometimes, the pulse height of the incoming photon may also be less than the threshold limit. In this case, the discriminator does not recognize this pulse and thus it goes uncounted by either of the bins. The analog PMT pulses are passed through the first discriminator, which converts them into TTL pulses * with a $6.5ns$ 'dead' time. The discriminator operates against a threshold voltage, detects and converts PMT pulses above that particular voltage.

5.1.5 PITLIF Data Processing and Signal Calibration

The conversion of the measured bins D1-D4 to fluorescence lifetime, concentration, and flame emission background, is a time consuming process. Because of the dual pulse resolution (DPR) of the discriminators, photon pile-up can occur in the discriminators and pulse counters, causing the measured bins to be non-linear with signal. Hence, a detailed consideration of pile-up statistics must be undertaken to account for saturation effects at large fluorescence signals and for accurate recovery of decay parameters. Renfro *et al.* [69] presents a derivation of the pileup statistics, which iterate to a solution based on the measured bin counts and a simulated saturated fluorescence decay based on a Poisson distribution of photon arrivals and on the DPR of the discriminators.

The result of this derivation is an iterative "saturate-and-compare" solution to recover the fluorescence decay parameters from the measured data. A program which encompasses this solution was written in FORTRAN [40]. The time-series

*Transistor-Transistor Logic Pulse

stored in each bins are then converted into a single time-series and the code typically requires 2-5 minutes for conversion of a 4096 point time series when using a 200 MHz PC with 32 MB of memory.

After pulse pile-up corrections by the "saturate and compare program", the resulting time series were calibrated with the known environment to obtain quantitative results and to decrease the uncertainty in the experiment. For the OH measurements investigated here, the quenching-corrected fluorescence measurements are calibrated against an opposed-flow, laminar diffusion flame with $35\%CH_4$ / 65% N_2, a strain rate of 40 s^{-1} and the the Reynolds number of 800. Reynolds number is calculated from the ratio between inertia force with the viscous force of the flowing fluid. Measurements were taken at various axial locations along the jet centerline and the calibration factor was determined by equating this measurement to the concentration profile recovered from the OPPDIF code using the GRI 3.01 kinetic mechanism [70]. The measured and computed axial OH profiles for the calibration flame are shown in figure 5.6. The measured OH profile has a FWHM (full width half maximum) of $2.0mm$ in comparison to a FWHM of $1.4mm$ predicted by OPPDIF. The peak [OH] value predicted by OPPDIF is $2.57 \times 10^{-8} mol/cm^3$. All turbulent flames were then calibrated by comparing to this extracted value from the OPPDIF code.

5.2 OH-PLIF in Opposed Jet Flames

This section details on the experimental set-up and instrumentation required to successfully accomplish PLIF measurements in a turbulent opposed jet flame. The importance of hydroxyl molecule in topological studies of the turbulent flames was detailed in the last chapter (see section 4.2.1). To provide a sound basis for statistical analysis, 3000 single-shot OH distributions were monitored for each flame configuration.

5.2.1 Laser System

The laser system for experimental measurements includes following components: Nd:Yag laser (Quanta Ray GCR-4), dye laser (Spectra Physics, PDL-3) and a wavelength extender (WEX). For the two-dimensional excitation of the OH molecule laser pulses of high peak power, high temporal and spatial resolution

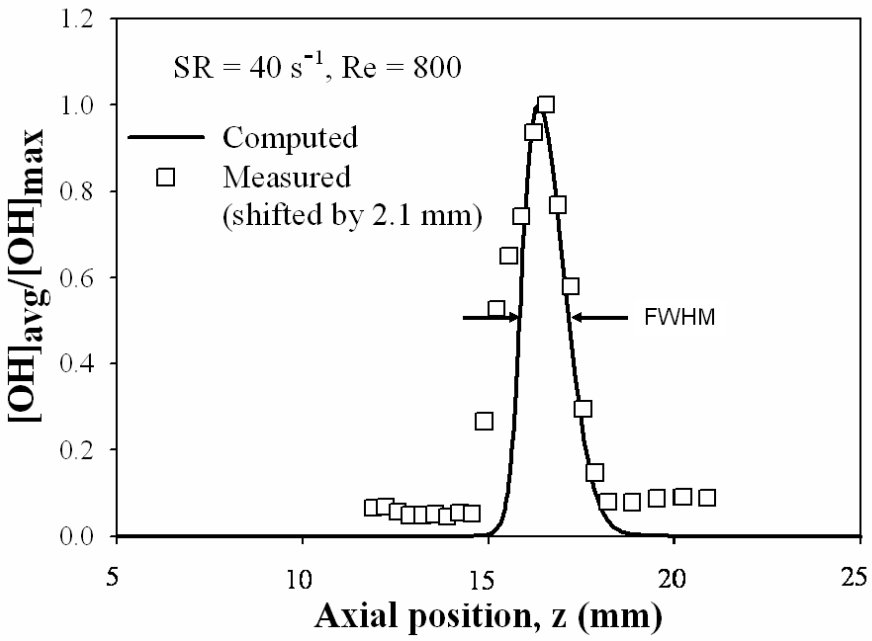

Figure 5.6: Measured and simulated axial OH profiles for a counter-flow flame with $SR = 40 s^{-1} and Re = 800$. Stagnation plane for the opposed jet geometry is at z equal to 15 mm. Full width at half maximum (FWHM) is shown with the arrows.

and at fixed absorption transition are required. Conventional Nd:Yag laser system in combination with dye laser is used mostly for OH excitation, even though transition of hydroxyl molecule could also be excited by excimer laser. High peak power permits wavelength conversion through several nonlinear processes, such as: frequency doubling, frequency mixing, or dye laser pumping. For these experiments, the heart of the laser system was an Nd:Yag laser with a repetition rate of 10 Hz, pulse duration of 10 ns FWHM and an energy per pulse of approximately 900 mJ at a wavelength of 1064 nm. This Nd:Yag laser acts as a laser light source to pump a dye laser.

A infra-red pulse from the Nd:Yag laser was frequency-doubled with the help of a nonlinear crystal situated in a harmonic generator module. The output beam from the harmonic generator contains both fundamental* and second harmonics† laser beams. A high energy laser mirror ($R > 99\%$) splits the pump beam (532

*IR beam = $\lambda_w at$ 1064 nm)
†Pump beam = $\lambda_w at 532nm$)

nm) after the harmonic generator module, whereas the infra-red was blocked with a beam dump situated outside the Nd:Yag laser. A small fraction of pump beam, after the beam splitter was sent to excite the dye* that is flowing through oscillator cuvette and the remainder excites the dye flowing through the amplifier. The oscillator cuvette is the part of a precision monochromator that consists of output coupler, a six-prism beam expander and a grating. In the oscillator, the grating disperses the light, allowing only a narrow wavelength to be reflected back to the oscillator cavity. The laser beam from the oscillator was passed through amplifier cuvette leading to the augmentation in energy of the laser beam.

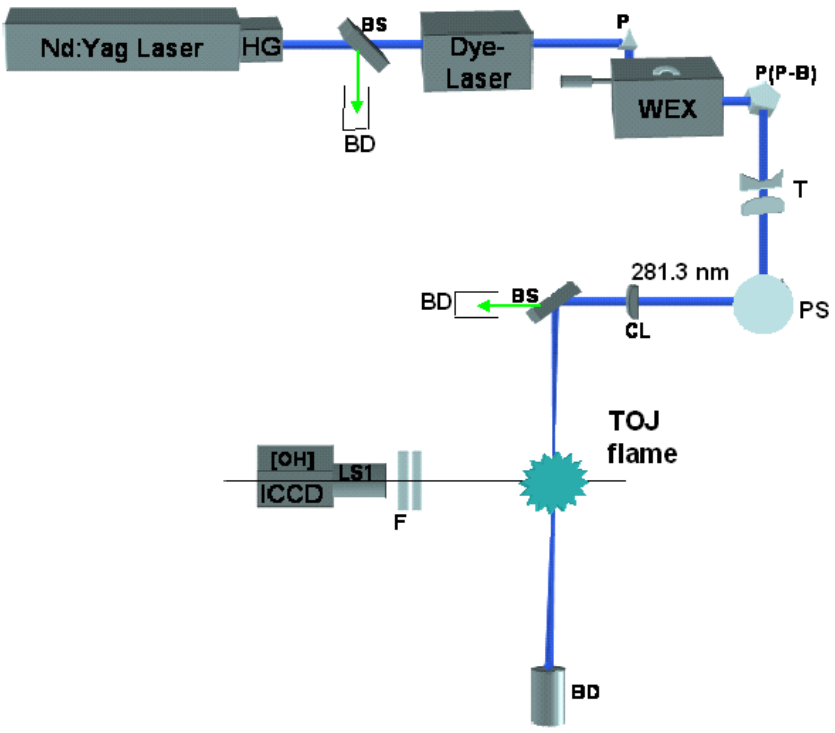

Figure 5.7: Schematic diagram of the OH-PLIF set-up. P: prism, WEX: wavelength extender, P-B P: pellin-brocca prism, T: telescope, PS: periscope, CL: cylindrical lens, F:filter, LS1: focusing lens, BD: beam dump.

The wavelength of the laser beam from the output window of the dye laser was tuned to 562.6 nm. The output beam from the dye laser is then steered into the

*Dye = Rhodamine 6G

wavelength extender (WEX) with the help of a fused silica prism. This beam was frequency-doubled with the help of nonlinear crystal (KD*P crystal) situated inside the WEX. The resultant output UV beam ($\lambda_w \cong 281.3nm$) from the WEX was used to excite the OH radical in the test section. The UV beam was tuned to the $R_1(8)$ line of the $A^2\Sigma^+$ ($\nu' = 1$) $\longleftarrow$ $X^2\Pi$ ($\nu'' = 0$) band of OH with the help of counter that is attached to the precision motor that drives the tilt of the grating situated inside the dye laser. This choice ensures lowest population distribution variation in the pumped energy level with respect to temperature.

5.2.2 Optical Set-up

The output beam from the WEX mainly consists of UV (281.3 nm). In order to achieve the pure UV laser beam, the output UV laser beam from the WEX was passed through a pellin-broca-prism that disperses the incoming laser beams. In order to cover the complete flame height centered between the burner nozzles, the height of the laser beam was expanded to a factor of 1.8 with the help of a telescope optics. The telescope assembly includes the combination of a negative lens (f1 = -100 mm) and a convex lens (f2 = 180 mm). The height difference between the measurement volume and the laser beam was about half a meter. Therefore, the laser beam was brought to an adjustable height between the burner nozzles with the help of a periscope that consists of two high energy laser mirrors. The laser energy was found to be reduced to 0.8 mJ before the measurement volume, which was due to the use of high reflecting mirrors in the periscope that were meant specifically for excimer laser beam (designed wavelength at 248 nm).

A laser sheet was formed with the help of a cylindrical lens (f=250 mm). This cylindrical lens focused the laser sheet to the investigated volume without altering the height. The dimensions defined by the laser sheet focused in the measurement volume was 27 mm (L) X 9 mm (H) X 0.25 mm (W). Extra height from the laser sheet was blocked by the circular mask placed at 100 mm before the focussing cylindrical lens. The fluorescence from the A-X (1,1) and (0,0) bands ($\lambda_w = 307 - 330nm$) was collected and imaged by a detector located perpendicular to the laser sheet (see figure 5.7). A dichroic filter was used in front of the detector to avoid detection of flame luminosity and spurious light scattering. The recorded area of OH fluorescence is 9 mm high, limited by the laser sheet.

5.2.3 Image Detector

Generation IV intensified charge couple device from Princeton Instruments (384 X 576 pixel / 16 bit) was used to detect the two-dimensional fluorescence from the excited molecule (here OH), which was placed at 90° to the focused laser sheet. ICCD was cooled to $-35°C$ to reduce noise due to dark current. To focus the incoming fluorescence to the CCD, a UV-Nikkor objective of focal length $f = 105mm$ and "f-number" of 4 was used. An "f-number" is defined as the ratio of the focal length with the diameter of the optics. The CCD chip contains 384 X 576 pixels, which corresponds to the area of 17.1 mm X 25.6 mm of the laser sheet. This implies that an object of about 44.5 μm in size was resolved in our measurements.

High speed gating of micro-channel plate and shutter control of the detector was provided by a gate pulse generator (model FG-100). Exposure time (Δt gate) of 100 ns was used to detect fluorescence from the focal volume, which was controlled from above mentioned pulse generator. Since the background noise and read out noise was very low, increase in exposure time had no effect on signal-to-noise ratio. It was possible to take 10 images per second which corresponds to the pulse frequency of the laser. But the read-out time for the camera electronics (controller ST-130) was high that restricts the capture rate of each frame to 0.5 Hz.

5.2.4 Synchronization: OH-PLIF

In order to carry out meaningful measurements, exact synchronization in time of individual instruments in the experimental set-up was required. For that purpose, a variable quality switch (q-switch) pulse-out from Nd:Yag Laser was used as a master trigger [see figure 5.8]. Q-switching is a technique by which a laser can be made to produce a short laser pulse with a very high peak intensity. It is acheived by putting a variable attenuator inside the laser's optical resonator. Variable q-switch was a TTL * pulse that acts as a pre-trigger and was used to synchronize the detector with the incoming laser light pulse. A delay generator DG-535 provided required delay in the set-up, which is triggered from the variable q-switch output pulse of the laser. Once pulse generator FG-100 detects the trigger

*Transistor-Transistor Logic Pulse

from DG535, it sends the high voltage pulse that opens the internal shutter of the detector (ICCD).

The detector was left open for a defined exposure and the incoming light was registered in the CCD. After the detector had finished registering photons, the captured light in the CCD wells were transferred to the analog-to-digital converter for the read-out process. During the read-out process the camera controller sends the not-scan pulse to the pulse generator FG-100, which restricts the detector to register new images during read-out process. Once the read-out was done, camera controller frees the pulse generator to send the high voltage pulse to the detector and the next image is taken. The schematic of the trigger system is depicted below.

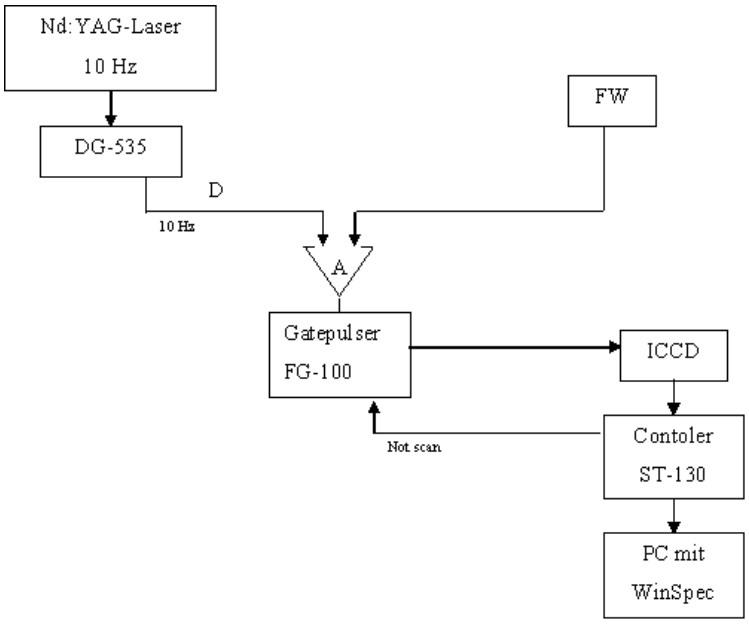

Figure 5.8: Schematic showing the trigger system used for PLIF measurement. DG535: delay generator, FW: flame watcher, A: logical AND, FG-100: High voltage pulse generator, ICCD: Intensified charge couple device (detector), ST130: controller for the detector.

Normally DG535 and pulse generator were triggered at 10 Hz, similar as Nd:Yag laser. However, time required during read-out process was long, which lets the detector to register at the rate of half the frames per second. For the

measurement of extinguishing flames, a flame watcher was installed in the set-up that triggers an output TTL signal only when it detects flame. This was required since some of the high turbulent flames extinguished every 10 sec, thus making experiments almost impossible without flame watcher. A flame-monitoring device F-150 in combination with a flame sensor FFS 05 from LAMTEC Leipzig GmbH & Co. KG was used as a flame watcher. It detected the flame emission within the spectral range of 210-400 nm. To remain in the "flame in" stage the sensor required a pulse amplitude of $\geq 30mV$ by viewing to the flame.

The flame monitoring device, which was connected in series with the flame sensor is able to distinguish between the "flame in" and "flame out" states of the flame. It also outputs the TTL signal that can be used to synchronies the flame ignition system which is controlled with LABVIEW software. Logical "AND" was used in between DG535 and the pulse generator FG-100. The output of DG535 delay generator was connected to the one end of the logical "AND", whereas the other end was connected to the TTL output from the flame watcher. Trigger to the pulse generator is initiated once the high peak of TTL signal from both delay generator and the flame watcher was detected. Pulse generator then sends high voltage signal to the detector for initializing frame capturing process. The high peak of TTL from flame watcher corresponds to the "flame on" condition and therefore, image was captured only when flame watcher detected signal.

5.3 Multiple Scalar Measurements in Swirl Flames

This section elaborates the experimental set-up for simultaneous measurement of radicals [OH][HCHO] in turbulent premixed swirl jet flames. Most of the previous reports have chosen separate laser systems to excite individual molecules in order to extract meaningful single-shot planar images [57]. We have used a single Nd:Yag laser system to excite both molecules for our measurement. Several literature have been reported that used a laser wavelength of 338 nm [30] and 353.4 nm [60], but only few have used a laser wavelength of 355 nm to excite the formaldehyde molecule for point and planar measurement in combustion flames [57]. This is because the excitation wavelength of 355 nm lies on the weak transition, which results in bad signal to noise ratio and does not permit single-shot measurements. We have been able to successfully carry out planar,

single-shot measurements inside the turbulent flame with sufficient contrast to identify the formaldehyde molecule.

5.3.1 Experimental Set-up

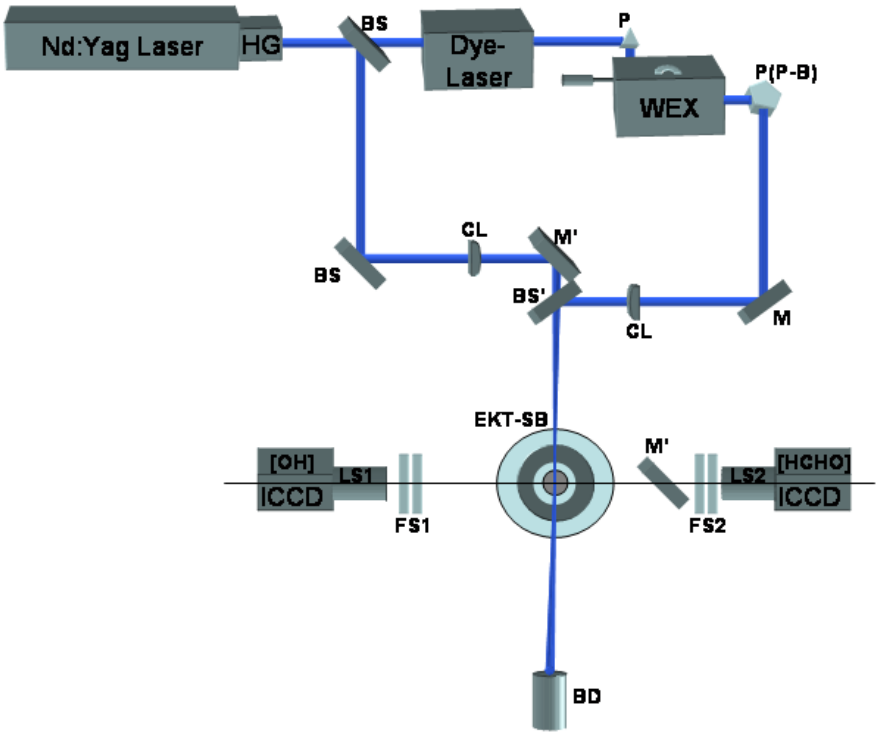

Figure 5.9: Schematic of experimental set-up for multiple scalar measurement. P: prism, WEX: wavelength extender, P-B P: pellin-brocca prism, CL: cylindrical lens, BS: beam splitter, M,M': mirror, FS1,FS2: filter set, BD: beam dump, EKT-SB: EKT-Swirl Burner.

The laser system for multiple scalar measurements was similar to that used in [OH]-PLIF, except an additional non-linear crystal (3^{rd} harmonics) was used to generate a laser pulse at wavelength 355nm from the same laser system. Harmonic generator module inside the laser for multi-scalar measurements contained two non-linear crystal that outputs laser light at 2ω (532 nm) and 3ω (355 nm) from the laser system. Where ω is the natural frequency of the laser light and

higher values are its harmonics. The green laser beam at wavelength 532nm was used to pump the dye laser to generate 568 nm, which is then frequency doubled using another non-linear crystal inside wavelength extender to generate 283.1 nm.

The output beam from wavelength extender was used to excite the A-X band (transition) of the hydroxyl radical inside the flame. Laser beam generated from third harmonics was reflected with the help of high energy laser mirrors with a reflection greater than 99.5 % situated just before the entrance of dye laser. This beam was redirected to the measurement volume and was used to excite the weak transition of the formaldehyde radical in the targeted flame. An schematic of the experimental set-up used for this measurement can be seen in figure 5.9. The hydroxyl molecule was excited with the laser beam generated from wavelength extender at 281.5nm.

5.3.2 Optical Set-up

As shown in figure 5.9, a laser beam 355 nm and 532 nm is generated inside the harmonic generator with the help of non-linear crystals. UV laser beam at 355 nm was reflected using a beam splitter BS just before the dye laser. An IR laser beam was blocked and a laser beam at 532 nm was used to pump the dye laser [Rodamine 6G], that generates laser at 563 nm. The output laser beam from the dye laser is reflected with the help of a prism to the entrance of wavelength extender. Laser beam at 563 nm is then frequency doubled with the help of *KDP crystal inside the WEX generated laser beam at 281.5 nm, which is then filtered with the help of Pellin-Brocca prism. This laser beam at 281.5 nm is used to excite $R_1(8)$ band of OH molecule. Before required laser beams at 355 nm and 281.5 nm is launched to the focal volume, they are transformed to laser sheets with the help of cylindrical lens with focal distance of 1000 mm.

The emission was collected at 90° of the laser sheet, and imaged on a gated intensified ccd camera with an UV-Nikkor objective lens of focal length $f = 105mm$ and a "f" number 4. Suitable spectral band-pass filters were interposed in front of the individual detector to reject elastic scattering (Rayleigh scattering) at the laser wavelength and to select the suitable fluorescence. Filter set [FS1] on the hydroxyl detection side includes dichroic short pass filter(T $\geq$ 95% between 305-330 nm). Whereas, filter set [FS2] on the formaldehyde consists of GG-

420 and CP-AB-505-2X. The transmission curves for FS2 filters are checked till 800 nm because no laser induced emission was detected from the combustion flame beyond this limit. In short, hydroxyl ICCD can only detect laser-induced emission ranging from 305 nm to 320 nm, whereas formaldehyde ICCD is made to detect the light within the wavelengthrange 420 nm to 500 nm.

5.3.3 Image Detector and synchronization

Image detector for OH molecule was used as mentioned in the starting of this chapter. For detecting signal from formaldehyde molecule, a similar intensifier CCD device as the OH molecule was used.

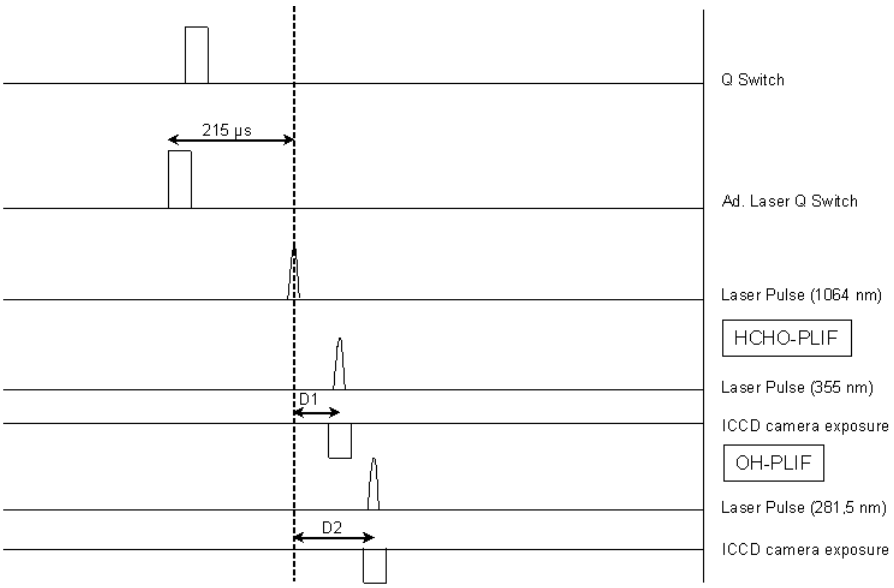

Figure 5.10: Schematic diagram showing delay between laser and detector trigger pulse for simultaneous measurement. laser pulse(1064nm): laser pulse out, laser pulse(355 nm): laser pulse at focal volume (D1=150 ns), laser pulse(281.5 nm): laser pulse at focal volume (D2= 650 ns).

Trigger system looked very similar to the one that was used during the OH-PLIF measurement, except one extra detector and its controller was added and that was also controlled with the same delay generator DG535 mentioned in OH-trigger schematic. Laser trigger was used as a master trigger for the complete experimental set-up, other electronics utilized was a delay generator DG535,

pulse generators for intensifier charge couple devices (ICCD's) and computer for data acquisition that captures and stores the captured images. A pre-trigger pulse from the laser triggered the delay generator, that controls the delay of H.V.pulse to the individual ICCD detector. A pulse generator FG-100 was used to pulse the ICCD detector [OH-side] once a TTL pulse from DG535 is detected. Another pulse generator from Stanford instruments was used to pulse the other detector[HCHO-side]. Both delays were controlled from the DG535.

As shown in figure 5.10, there is a small delay between D_1 and D_2. This delay was about $500ns$ and since the smallest scale of turbulence (Kolmogorov scale) in the flame was much larger than this value, these measurements can be still called as simultaneous measurements.

5.3.4 HCHO spectrum analysis

Initially a planar image of the flame was captured in order to get an idea on the location of excited molecules inside the laminar flame by the laser light at 355 nm. In order to confirm for the formaldehyde molecule, emission spectrum at the high intensity location was registered using a spectrometer and a two dimensional detector array. This measured spectrum was then compared with the spectrum available in the literature [68] (see figure 4.7). The combination of Planar measurement and spectrum analysis confirmed us that we were exciting and detecting the formaldehyde molecule.

5.3.4.1 Planar Measurement

Formaldehyde molecule was excited using a laser light at 355 nm that can be easily accessible by using a 3rd harmonic non-linear crystal before the fundamental beam (1064 nm) from an Nd:Yag laser. Details on the laser system used for these measurement are provided in the section(5.2.1).

An ICCD detector of chip size 384 X 576 pixels was used and each pixel size was equal to 44.5 μm X 44.5 μm, which means that the whole chip thus corresponds to 17.1 mm X 25.6 mm approximately. This detector was gated with the help of a pulse generator FG100, and was set at 50 ns opening time, which was enough for fluorescence signal to be captured. This gated time was kept low in order to reject the unwanted stray light from the reflecting surfaces near the measurement space. Synchronization of such experimental set-up was done, which was almost

similar to the trigger system used in OH-PLIF measurements in opposed jet burner.

As can be seen from the figure 5.11 (a), the output beam from the harmonic generator was redirected with the help of dichroic mirror and was turned into a laser sheet with the help of a cylindrical lens of focal length 1000 mm, which is then focused to the focal volume above the burner nozzle. The two-dimensional fluorescence signal was captured by the detector placed 90° to the incoming beam. Rayleigh signal from the laser beam was rejected using a long-pass filter GG-420 [Schott glass filter] in front of the detector.

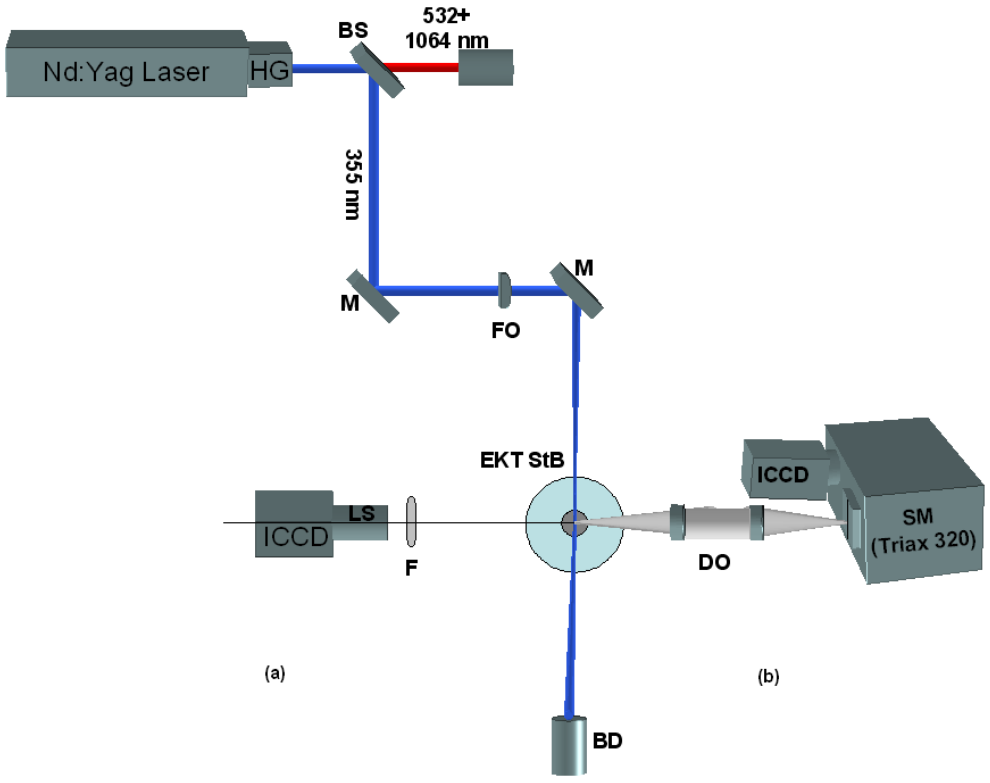

Figure 5.11: Side(a): Experimental setup for HCHO-PLIF measurement in EKT standard burner. Side(b): Experimental setup for point measurement for HCHO emission spectrum in EKT standard burner. FO: focussing optics, DO: detection optics, F: filter, M: mirror, BS: beam splitter, BD: beam dump.

5.3.4.2 Spectrum Measurement

For spectrum measurement, the laser beam was focused to the single point in the measurement volume by a spherical convex lens of focal length 500 mm. Fluorescence signal from a point was collected with the help of collecting lens (L1) of 200 mm. The collimated beam was then focused to the entrance slit of the spectrometer with another lens (L2) of 250 mm. This combination confirms the f-number of the collection system is less than the f-number of the spectrometer, which is important to capture the maximum signal inside the spectrometer. The grating of the spectrometer was having the resolution of 600 line/mm and had the spectral dispersion of 2.64 nm/mm. The signal from the grating was then redirected to the exit of the spectrometer and then to the ICCD detector as can be seen in figure 5.11(b).

6 Data Image Processing

Image processing can be understood as the transformation of the "raw image" to a meaningful "processed image". An image is defined as a function u on $\Re^2$ raster, where u(x,y) represents the gray value or intensity at point (x,y). Accurate detection of relevant object accurately and extraction of required data has a central importance in image processing. This relevant object must be clearly distinguished from background or other interfering objects.

This assumption is however seldom met in real world application due to factors like limited dynamic range of detectors, dark noise etc. Therefore, correction procedures should be implemented to compensate for these experimental defects. Introduction on image processing for scientific application is available from a well known handbook from Jähne [71]. In this chapter, details on post-processing algorithms that include correction, noise rejection and image enhancement of structures are described. Strategy applied for the image post-processing is divided into following steps:

1. Correction
    a) Background correction
    b) Correction of the intensity of laser profile
2. Noise reduction
3. Edge enhancement
4. Binary image generation
5. Evaluation of topological flame characteristics (flame area, flame length etc.)

6.1 Correction

6.1.1 Background Subtraction

Experimental images have to be compensated for the background noise. It consists of constant positive level accumulated during read out process from the detector and experimental background intensity level. The background noise was determined by taking the images without any illumination, which was approx. 350 counts on the detector of 16 bit resolution. Background image was subtracted from acquired raw flame and laser intensity images to compensate for the background noise.

6.1.2 Laser Profile Compensation

Every laser based techniques requires normalizing of the data with the laser profile, in order to correct for the laser inhomogeneities. Therefore, the background corrected flame images were normalized by the average laser sheet to correct for the effect of laser fluctuations and inhomogeneities. Since hardly any change was observed in long term fluctuation of laser profile, the average over 50 accumulated images was used for compensating this defect. An averaged laser profile was captured between every 500 flame images.

Figure 6.1 shows the raw image, the laser sheet and corrected normalized image. Ideally after background subtraction of the acquired flame image, the intensity where molecules are not present should be zero. That would result in no surrounding noise spikes after laser profile compensation (normalization). But practically non-zero values lead to the noise spikes which can be clearly seen in normalized image. For eliminating these noises, further image post-processing techniques such as suitable filtering and edge enhancement was applied to this normalized image.

6.2 Noise Rejection and Edge Enhancement

Improving signal-to-noise ratio and reducing spurious pixel intensity values in unprocessed image is an important step in image processing. Normalized images (mentioned above) suffer from bad signal-to-noise ratio and require smoothing

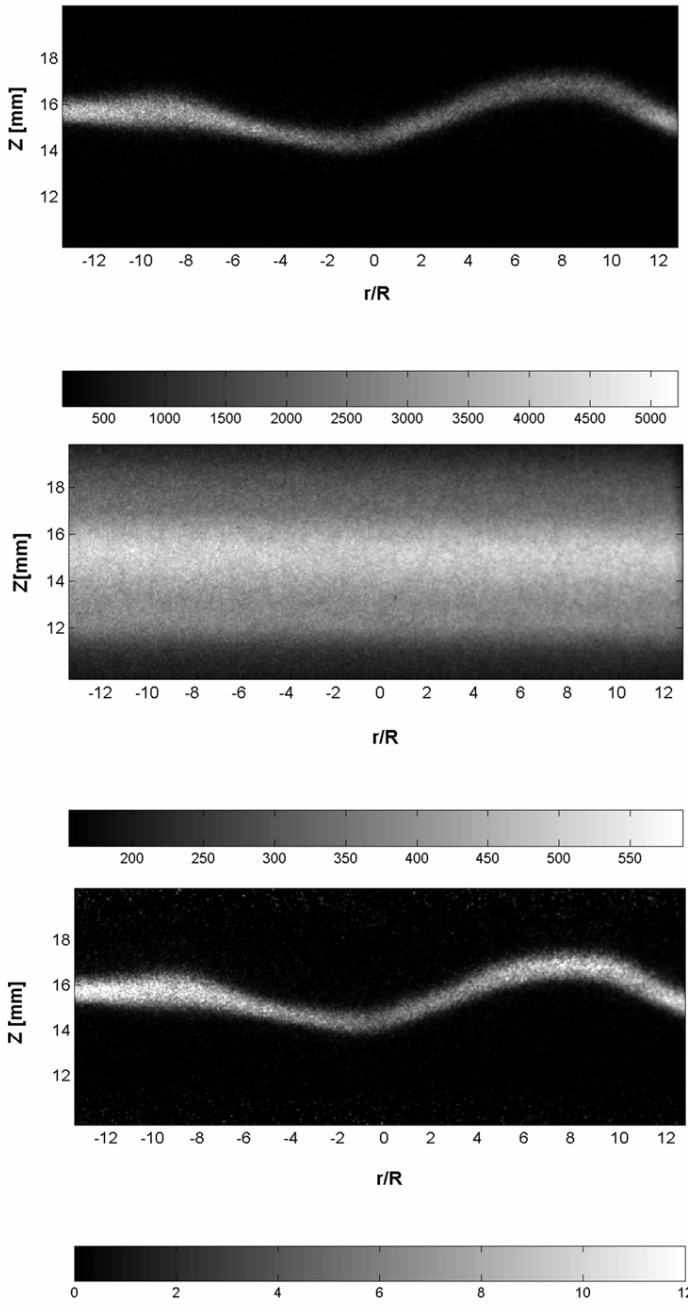

Figure 6.1: Laser profile compensation. Raw flame image(top), Laser Profile Image(center), Corrected Normalized Image(bottom). Gray value bar is shown in bottom to show the intensity profile.

of high frequency noise as well as enhancing of relevant structures before any topological studies are made. Several linear and nonlinear filters are available, but their application is restricted to the type of distortion in the given image. While linear filters work well within flat regions, they are questionable near the gradients. They tend to smooth all types of gradients independent, if they carry useful information or noise. Thus, applications of such filters are restricted to the images where the issue of gradient preservation and edge enhancement is not critical.

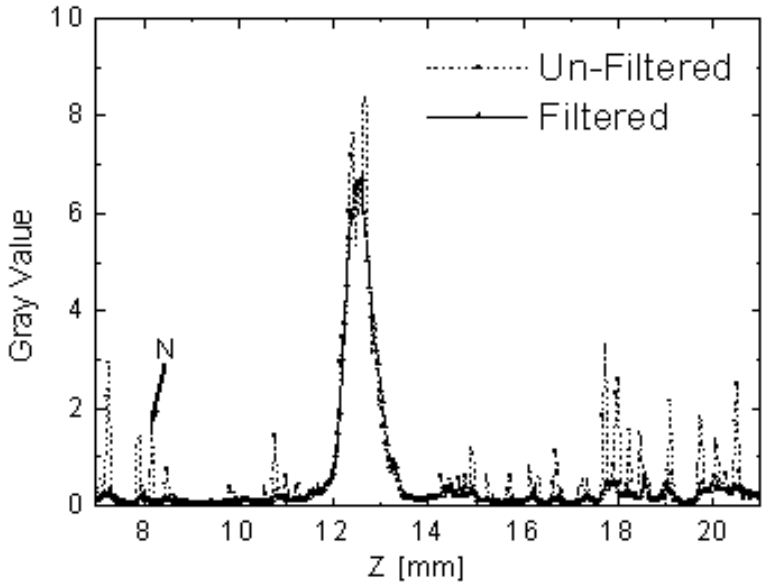

Figure 6.2: Graph displaying the profile filtered with two dimensional median method with mask size [5x5].

Non-linear filters can overcome such problem if user defined parameters are suitably applied to the given image. Objective choice of user defined parameters relies upon sensitivity analysis which will be discussed in the later part of this chapter. In this work only nonlinear filters were used for noise reduction since gradient preservation and edge enhancement is critical for detection of the flame front.

6.2.1 Median Filter

Experimental LIF images contained several high amplitude single-distorted pixels near gradient of intensity "u" of the detected species, which require smoothing before relevant information is extracted. Median filter was found as well-known approach to smooth out such pixels. In the case of median filter, the pixels of a sub-area defined by the neighborhood are sorted for their amplitudes. The value of the central pixel of the sub-area is then re-defined by the amplitude, which is in the middle of this arrangement. In this process, it efficiently removes the solitary pixels with highest and lowest amplitudes emerging near the gradient without altering the gradient itself. The effect of median filter in a test profile is depicted in figure 6.2.

6.2.2 Non-Linear Diffusion method

Next step of image processing after unwanted noise is diminished, is to enhance the relevant structures. This is best done by using an edge enhancement routine. Here, non-linear operation based on partial differential equation known as nonlinear diffusion method was applied. Non-Linear diffusion has deservedly attracted much attention in the field of image processing for its ability to smooth noise locally, within regions defined by boundaries. Smoothing stops as the discontinuity such as boundaries are reached, which leads to amplification of boundaries or edges in the given image.

It is adapted from an approach originally formulated by Perona and Malik [72][73]. A good introduction to nonlinear diffusion can be found in lecture notes of J.Weickert of Dept. of Computer Science. Weickert [74][75] also gives a comprehensive survey of the literature. Malm [76] applied NLDF filtering in the images taken from planar laser induced fluorescence spectroscopy.

To apply a diffusion process to an image, we regard the gray value u as the concentration of a chemical species. Equation 6.1 shows the solution of the linear diffusion equation, where D is a scalar constant known as diffusion coefficient. Perona & Malik (1987) proposed to exchange this diffusion coefficient D in eq. 6.1 with a scalar-valued function g of the gradient ∇u of the gray values in the image [eq. 6.2]. This non-linear equation is solved iteratively till the desired result is achieved.

$$\partial_t u = div(D\nabla u) \tag{6.1}$$

$$\partial_t u = div[g(\nabla u)\nabla u] \tag{6.2}$$

The diffusion coefficient is made dependent on the edge strength as given by the magnitude of the gradient, thus making diffusion process non-linear. The function g is required to be smooth and non-increasing with g(0)=1 and g(s)→ 0 for s → ∞, where s is equal to ∇u. We used the diffusivity function proposed by Weickert. Figure 6.3 shows comparison of Weickert's and Perona & Malik diffusivity function. Weickert's diffusivity function reads as:

$$g(s) = 1 - exp[-c_m/(s/\lambda)^m] \tag{6.3}$$

where m is a positive integer and a constant. It is a process specific constant which governs the shape of the function "g". Big values of 'm' make the flux of the function change quickly. The constant c_m is calculated to make the flux function $(s * g(s))$ ascending for $s < \lambda$ and descending for $s \geq \lambda$. That means the diffusion in the direction across the edges will be a forward diffusion when ∇u < λ and a backward diffusion when ∇u > λ. Lambda is the contrast parameter, that separates regions where forward diffusion occurs from those where backward diffusion takes place. In other words, if the gradient is inferior to lambda the flux is increasing with the gradient and if the gradient is larger then lambda the flux decreases as the gradient grows.

Figure 6.3 shows the three different diffusivity function formulated by Perona & Malik and Weickert. The solid curve corresponds to Perona & Malik, the dotted (m=2) and dash-dot (m=8) curve corresponds to diffusivity function of Weickert. The flux rises to its maximum at λ=1, then falling again for increasing gradient ∇u. Parameter selection for edge detection was done in such a way that maximum diffusion occurred for the gradient exhibited by noisy features and minimum for the edges. This selection helps in clearly distinguishing the regions across the gradients. Weickert diffusivity function with greater m shows sharper peaks in the flux, which directly means less iteration required for desirable results. It also has a drawback that the function becomes sensitive to proper choice of λ.

Influence of various critical user defined parameters used in non-linear diffusion

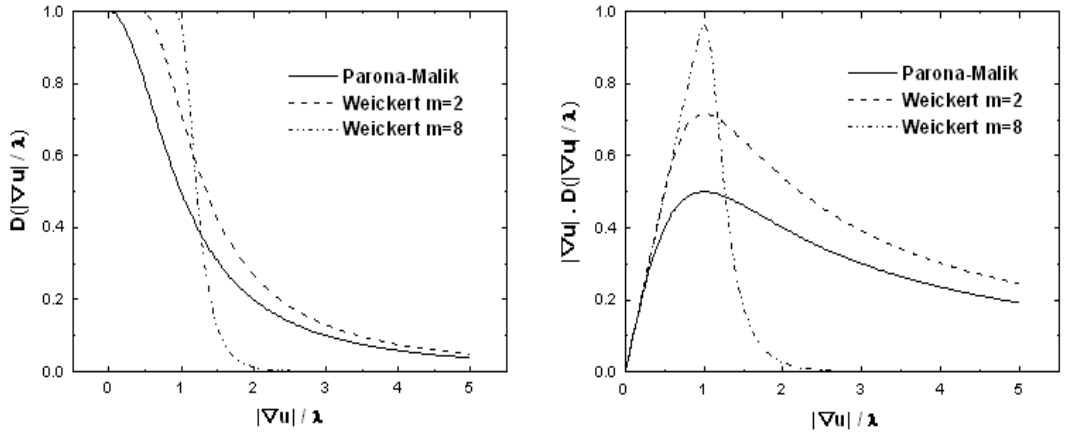

Figure 6.3: Diffusivity (left) and Flux (right) for three various function proposed by Perona and Malik and Weickert.

method are discussed in this paragraph. A test image was generated for this purpose with random noise of high intensity. A noisy, original and one dimensional profile (vertical position "y"=98) of a test image is shown in figure 6.4. This noisy test image was filtered and enhanced with nonlinear diffusion method.

Influence of various parameters such as contrast parameter "λ", constant "m", width of gaussian kernel "σ" are discussed. Left column of the figure 6.5 shows the effect of contrast parameter on test image. Lower value of lambda leads to the noisy image, this is because noise gradients which are larger than the user defined lambda are preserved. Larger values of lambda cause in blurring of crucial structures to such a degree that physical information is lost. Thus choice of contrast parameter is very critical to the image simplification. Center column depicts the influence of parameter "m". Parameter m defines the shape of the diffusivity function and lower value cause in constant diffusion in all gradients thus causing in smoothing of important structures along with noise.

Parameter "m" does not show any significant changes in images between 8 to 14 and therefore is not critical in present situation. The impact of Gaussian kernel width was also found constant between values of 0.8 and 1.4, although a lower value of σ leads to the noisy structures. This is because the important structures that needs smoothing are larger than the chosen width and therefore are not smoothed completely, resulting in the noisy image. Number of iteration

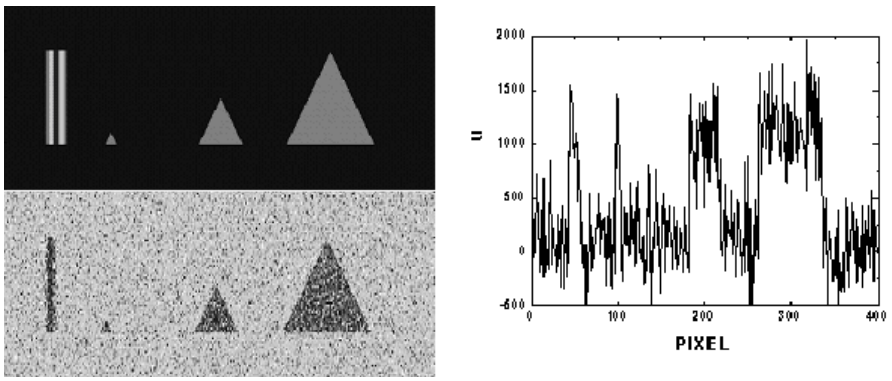

Figure 6.4: Original test image, random noisy test image and its one dimensional profile is shown.

for evaluation of these images was taken as 100. Contrast parameter "λ" is the only critical parameter and is the weakness of this method. Edge enhancement of this method is the advantage of this method, which leads to better distinguish between important structures and noise. Figure 6.6 shows a noisy intensity profile and its gradient. Corresponding filtered intensity profile and its gradient is also depicted. Also gradient enhancement can be clearly seen in the same figure.

6.3 Binary Image Generation

For the identification of structural quantities the amplitude information of the images is of no importance. Therefore, the gray scale images might be transformed into binary images without basic loss of information. Within the binary image, information is reduced to 'pixel inside the gradient' or 'pixel outside the gradient'. For this distinction, a simple threshold method is applied. Pixels with amplitude below a user set threshold are defined as OFF pixels and those with amplitude above the threshold are defined as ON pixels. Naturally, the settings of the threshold influence the results.

A threshold value which is too low generally implies inclusion of noise in the result, whereas a threshold too high results in a loss of relevant information by cutting away locations with lower signal intensities. Thus, the threshold derived from the objective analysis was chosen to meet both requirements i.e. noise rejection and information preservation.

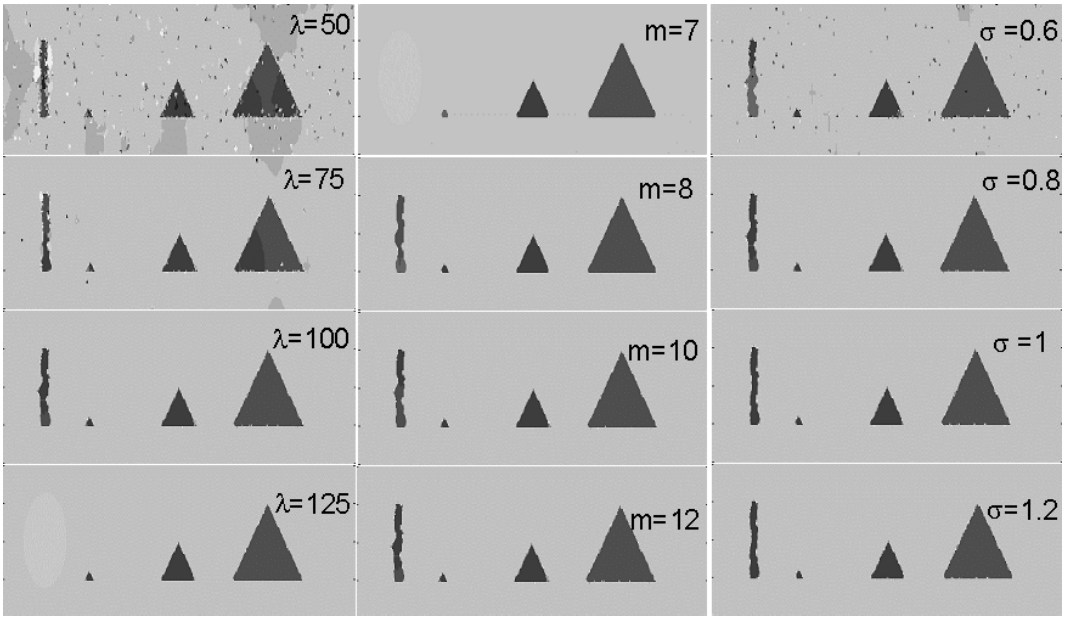

Figure 6.5: Influence of various parameters on test image after nonlinear diffusion method is depicted. Left column shows the effect of contrast parameter "λ" on test image. Middle column shows the effect of parameter "m" and the right column the gaussian kernel "σ".

6.4 Algorithms Applied

In qualitative topological studies, results are strongly dependent on the selection of filters and edge enhancement routines. Algorithm selection depends upon various factors such as computational speed, sensitivity to noise and user defined parameter. Therefore two algorithms are discussed that comprises suitable filter, edge enhancing routine and routine that generates binary image marking the flame front. Firstly median-threshold-majority method and secondly median-nonlinear diffusion-threshold method were tested. Both algorithms and there impact on results will be discussed later.

6.4.1 Median-Threshold-Majority Method

This algorithm includes two dimensional median filtering in LIF images, which is then followed by binary image generation. Median filter worked well to remove surrounding noise in the given image but was partially able to remove high

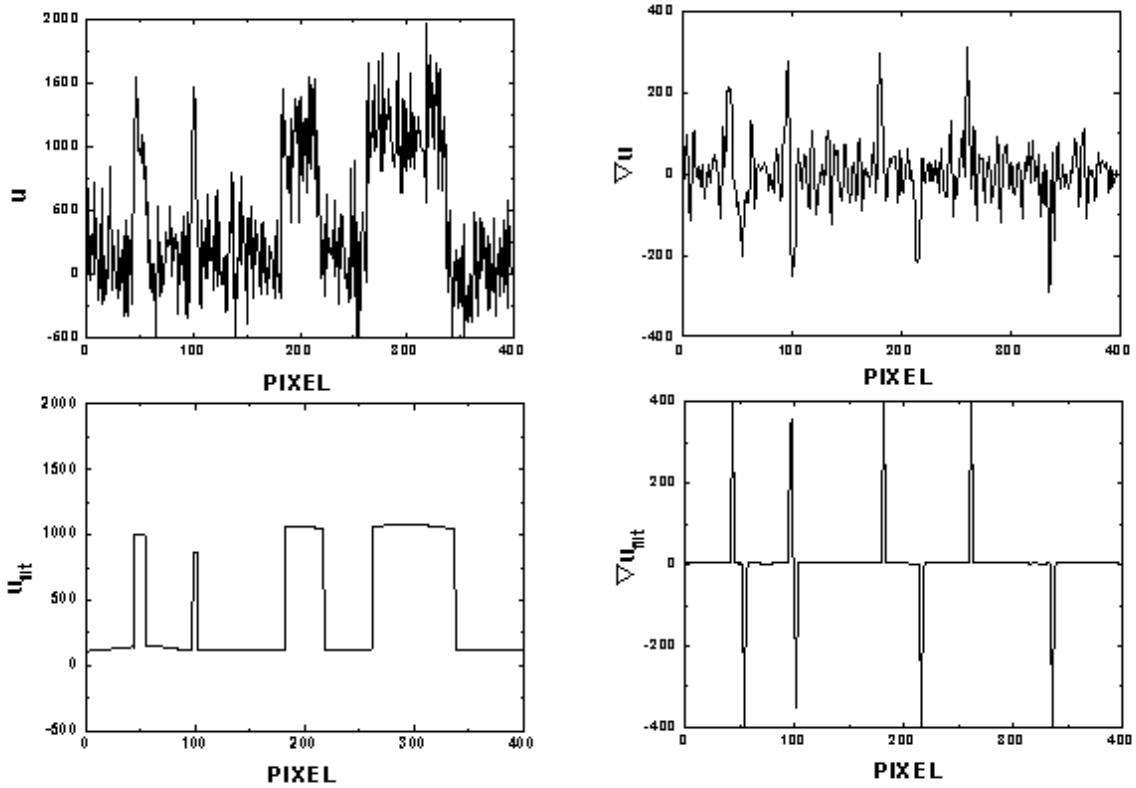

Figure 6.6: Figure shows Edge enhancement property of nonlinear diffusion method in a test profile. Top: Noisy profile from the test image and corresponding gradient of the intensity. Bottom: The filtered profile using non-linear diffusion method and the corresponding gradient of the intensity from filtered profile. Clearly edge enhancement of the profile can be seen from the gradient plot after the application of NLDF method.

frequency components attached to the edges. They are later removed by the application of an iterative process known as majority method. This method is an edge smoothing algorithm and is applied directly to the binary image.

Figure 6.7 shows the noisy contour after median filtering, which is smoothed by majority method. If the majority of the surrounding pixels defined by the kernel widths (defined as mask) possess the value 1 the central pixel, which undergoes the transformation process, is set to 1, otherwise it is set to 0. In this process, noise attached to the edges of a large structure becomes isolated and thus diffused

via iterative procedure.

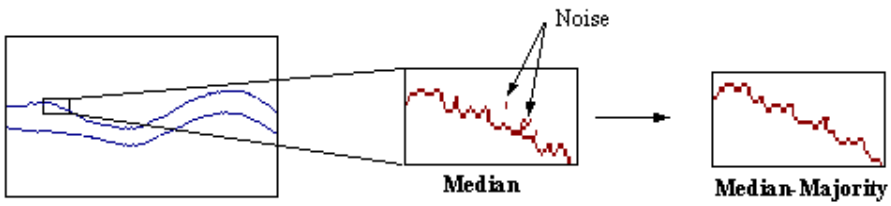

Figure 6.7: An example showing the removal of noise attached to the edges of the flame front via majority method

6.4.1.1 Sensitivity Analysis

An appropriate set of user defined parameters $\overrightarrow{k}$ (like filter kernel widths and signal intensity threshold) must be defined before applying algorithms to the given image. The choice of an optimized parameter set is crucial for the discrimination between noise and structural information and thereby for the identification of the topological flame characteristics $\overrightarrow{c} = \overrightarrow{c}(\overrightarrow{k})$. One possible way to quantify the influence of these parameters on the result is a sensitive analysis. This analysis yields the sensitivity $\mathrm{E}(\overrightarrow{c}, \overrightarrow{k})$ in dependence of topological flame characteristics with respect to the variation of each of the parameters, as shown in eq. 6.4.

$$E_{i,j} = \Delta c_i / \Delta k_j \tag{6.4}$$

If the selected quantity is insensitive to the variation of the parameter the sensitivity is small, which means the choice of the parameter is non-critical for the flame characteristics. The optimal parameter is located where the transition from a low to a high sensitivity is found. This is a point of maximum bending, or the maximum of the 2nd derivative of c_i with respect to k_j.

Naturally, this method is only applicable if c_i is not linearly dependent on the parameter k. Figure 6.8 shows the result of a sensitivity analysis. In this example the quantity c_i is the flame area that is defined as the total number of "on" pixels in the binary image. Both median kernel size k_1 and the threshold for binary image generation k_2 is varied. It is obvious that kernel size k_1 does not influence the results, whereas for $k_2<1$ a high sensitivity and for $k_2>1$ a small sensitivity

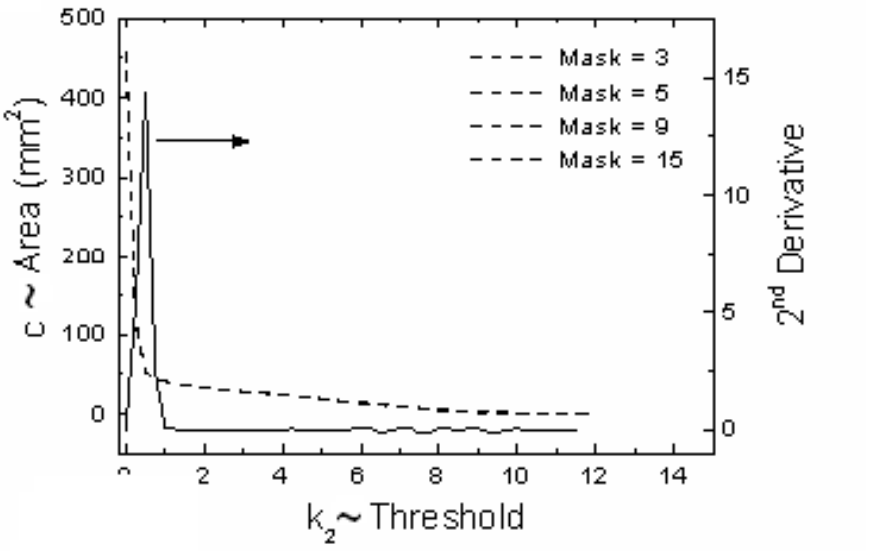

Figure 6.8: Sensitivity of flame area with threshold is depicted. Flame area verses threshold, also included is the 2^{nd} derivative of the OH area with respect to threshold.

is observed.

An optimal choice of k_2 is obviously approximately 1, slightly above the value where the second derivative of c_i shows a maximum. This maximum marks the transition from low to high sensitivity, as visible in figure 6.8. Notice, that the sensitivity analysis in this case additionally shows that k_1 and k_2 are statistically independent. From sensitivity analysis, it was concluded that threshold of value 1 is the proper choice for our [OH] PLIF images. Also kernel width is insensitive to the parameter of interest therefore, mask size 5x5 was chosen.

6.4.2 Median-Non-Linear Diffusion-Threshold

Figure 6.9 shows the LIF image before and after the application of nonlinear diffusion filter. Parameter that are not critical for LIF images are the parameter "m" ($8 \leq$ m ≤ 12), width of gaussian kernel "σ" ($0.8 \leq \sigma \leq 1.4$) and number of iteration (> 75 iteration). These limits of the user-defined parameter can also be concluded from the test images from figure 6.5. The set of parameter chosen for

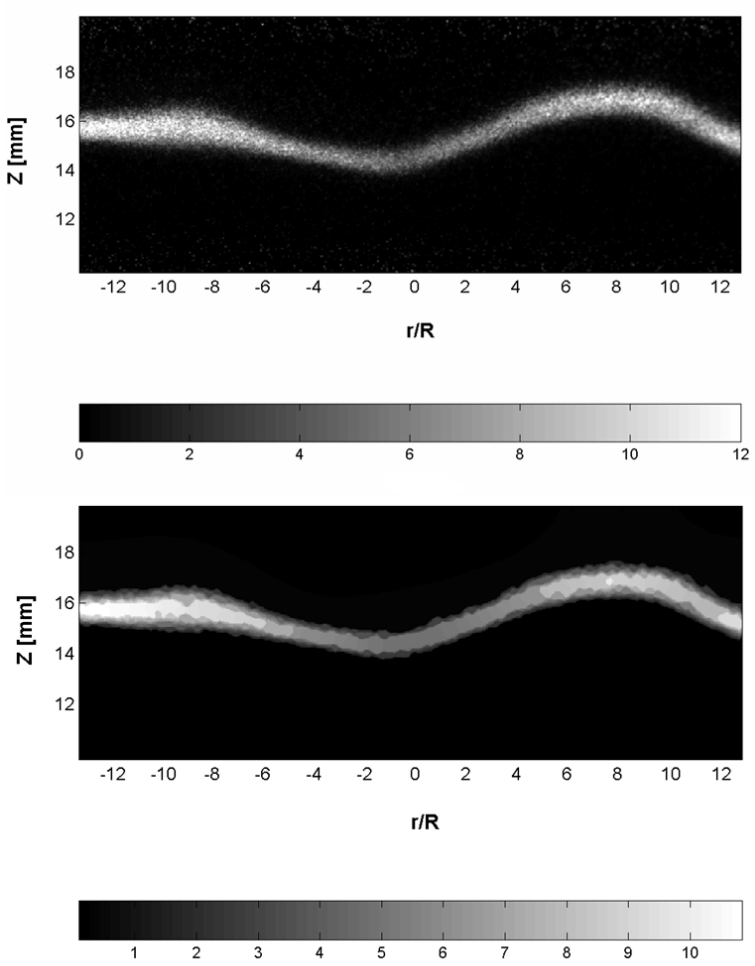

Figure 6.9: OH-LIF image before and after application of nonlinear diffusion method. Gray value bar is shown in bottom to show the intensity profile.

OH-LIF images from opposed jet burner were λ=0.2, m=8, no. of iteration=100, σ=0.8. Important features such as flame boundaries are clearly enhanced after nonlinear fusion filter as shown below.

6.5 Conclusion

It is always hard to say, which algorithm is best in image processing. It totally depends upon the features one has to preserve and unwanted noise. The worst case is when the noise are similar and distributed throughout the image along

with the important gradients that needs to be preserved. It is well known that it is impossible to define a single algorithm, which is suited for all types of features. Comparison of various algorithms for image post processing is discussed in details by Schiessl.et.al [77].

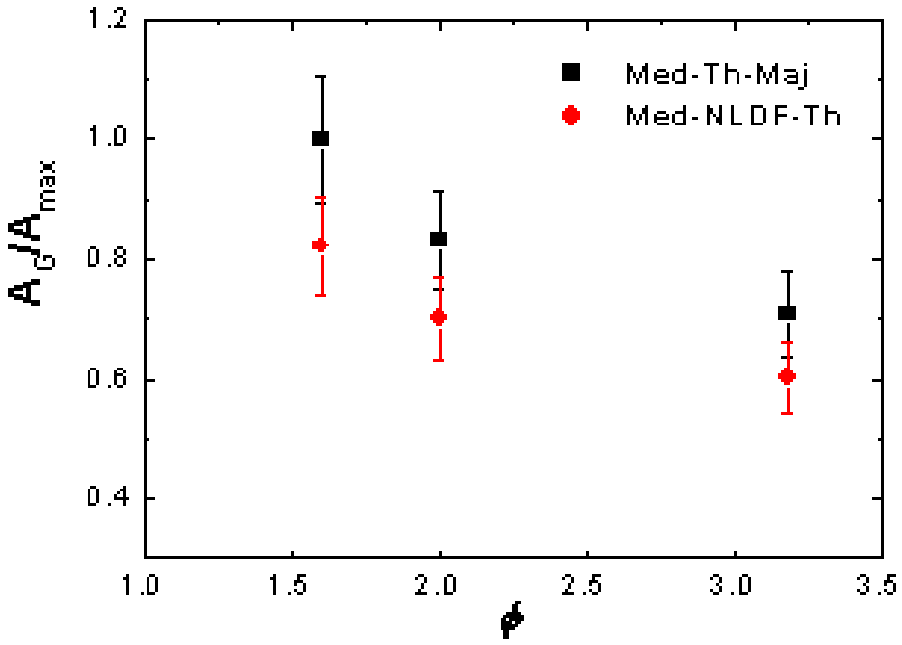

Figure 6.10: Global area extracted using two different algorithms of image post-processing from OH-LIF images. ϕ represents the equivalence ratio, A_G is global area and A_{max} is the mean global area value for flame with $\phi = 1.2$ and with algorithm "Med-Th-Maj".

Figure 6.10 shows the effect of different post-processing strategies to extract global flame area defined by OH molecule. Global area (A_G) is calculated as the total number of "on" pixels in the binary image, which is generated from the OH-PLIF raw images by applying a threshold. Statistics have been generated from 3000 instantaneous binary images. All global area values have been normalized with the mean global area value for flame with equivalence ratio 1.2 and algorithm type "median-threshold-majority". The results evaluated from two

different algorithms applied in image processing of images is also depicted. The trend remains the same for both the algorithms but the mean values are different. However, qualitatively trends and shapes of the results are important. Thus similar trend from both algorithms shows that the global area is insensitive to the type of algorithm applied.

For our LIF images, we have chosen the second algorithm (Median-nonlinear diffusion-threshold) because of its better efficiency in noise reduction, even in the presence of severe noise levels. Also it promises gradient enhancement, which is important for clear distinction between the burned and unburned regions of the flame. Although this method is time consuming and harder to implement numerically than the first algorithm (Median-threshold-majority method).

7 Opposed Jet Flames

The main results obtained on the turbulent opposed jet flames using laser induced fluorescence is presented. Chapter starts with the review on literature survey on stagnation point stabilized flames. Which is then followed by the detailed description of the EKT opposed jet burner and properties of the flames that have been measured in this work. Thereafter, characterization of the EKT opposed jet burner is provided, that includes survey and plots from the previous measurements using various non-intrusive techniques. Last section provides the outcome of the measurement and discussion on the major findings from the current study.

7.1 Introduction

The reasons for investigating counter-flow stagnated flames are manifold. Firstly these flames are relatively easy to control in the laboratory. Secondly with the same burner set-up, flames from the diffusion to the premixed limit can be studied while varying parameters like Reynolds numbers, strain rates, turbulence intensities and length scales, which is convenient from the experimentation point of view. Advantages for the modelers from using this configuration are the absence of pilots or flame holders, any contact of the flame to walls and the simplicity of its geometry. Therefore, for development and validation of various sub-models, a counter-flow geometry is ideally suited. Due to the rotational symmetry and the limited extension of the flow field, even complex phenomena such as turbulent-chemistry interaction can be explored by using advanced chemistry models or more sophisticated models of the turbulent flow like LES [78],[13].

Turbulent flames stabilized in a counter-flow geometry have been studied to gain insight into two major issues i.e. turbulent mixing and flame stabilization. In non-premixed flames, it is important in order to keep the combustion chamber compact and light in weight. Fast mixing between the two fluids is important

to restrict the flame length and enabling a more intense combustion. Premixed as well as non-premixed configurations have been investigated in the opposed jet geometry with various experimental methods for example by [79]-[96] and with numerical techniques, such as [78],[97],[98],[13].

Investigation on flame stabilization or the understanding of extinction mechanism is one of the fundamental issue in turbulent non-premixed flames. Therefore, most of the literature have been focussed on the understanding of the extinction events and the properties influencing it. Parameters like flow structure, flow properties, scalar dissipation rate, high strain rate etc. have been found to be influencing extinction events in such flames.

Kitajima *et al.* attempted to deduce the effects on extinction limits by varying turbulent characteristics of the air and fuel stream individually. This was done by the means of a laser tomographic technique [82],[83] and later more accurately by planar Rayleigh imaging. Kostiuk *et al.* [99] introduced the effects of small-scale eddies to the extinction of turbulent counter-flow premixed flames. It was shown that the extinction occurred when the sum of the bulk flow stretch rate and small-scale stretch rate caused by Kolmogorov scale exceeded a certain limit. Where flame stretch is defined as the fractional rate-of-change of flame area and expressed exactly as the sum of tangential strain rate and flame curvature. Similar criteria was applied for the extinction of partially premixed and non-premixed flames of opposed jet burner by Mastorakos *et al.* [87].

Mastorakos *et al.* [88] also confirmed another criteria initially proposed by Peters and Williams for the extinction of turbulent non-premixed flame. They identified the scalar dissipation rate as the central parameter controlling turbulent reactive flows and their extinction. It was also shown that the mean scalar dissipation rate increases with increasing bulk and/or turbulent strain rates, which implies that both strain rates have to be low to ensure non-premixed flame stability in the counter-flow geometry.

Thermocouple measurements of temperature, and its radial and axial dissipation, by Sardi *et al.* [93] demonstrated that scalar residence times in the mixing layer are shorter than large-eddy turn-over times and that fluctuations are strongly correlated with scalar dissipation rate. Results in the current thesis indicate the presence of "young turbulence" or in other words, turbulent flow is not fully developed during the mixing process. Also large scale motions are found to be the driving factor for extinction events in the investigated turbulent

opposed jet flames. Which implies that the flame stability is compromised by total flame stretching and not by small-scale wrinkling.

Recently, information on velocity field, scalars, and scalar dissipation of turbulent reacting and non-reacting opposed jets were obtained using 1D Raman/Rayleigh scattering and LDV in two dimensional flow field [13]. These experimental results were supported and accessed by results from numerical modelling (LES). Mixture-fraction and scalar dissipation rates were represented very well along the center-line. Same group also estimated the performance of mixing models on turbulent opposed jet flames similar to above [80]. These models were validated with the experimental results obtained from scalar and velocity field measurements. The numerical results were extracted from one-dimensional Monte Carlo PDF simulations with a 12-step reduced chemistry and reduced chemistry. Simulation in general showed a very good agreement for scalar and flow field properties in the physical space. However, extinction limits computed with the mixing models were overestimated by a factor of more than 2 in terms of bulk strain rates [80].

Laser tomography has been applied to study spatial flame structures of premixed [100] and non-premixed flames [82], but no studies exist with emphasis on turbulent partially-premixed flames. Furthermore, flame fronts detected by tomography are ambiguous since non-uniform distributions of seeding spray, size and spatial distribution of the spray have an impact on structural information. Thus, in analogy to extensive studies on turbulent jet flames [23],[101], there is a need of comprehensive data sets on counter-flow configurations especially for combustion LES validation.

7.2 Burner Description

The flow configuration in the EKT opposed jet burner * consists of two identical opposed nozzles, each surrounded with a annular section. A schematic diagram of the burner assembly is shown in figure 7.1 [81]. Each contoured nozzle, is profiled with a contraction ratio of 9:1 and is followed by a straight tube of 50 mm length. The inner nozzle with a diameter of D_{in}=30mm is surrounded by a concentric co-flow (D_{cf}=60mm) of N_2, which provides a flame stabilizing curtain in order to prevent pre-reaction of partially premixed fuel upstream of

*©Dirk Geyer(TU-Darmstadt)

the stagnation plane. For these measurements nozzle separation distance is kept constant, which is equal to D_{in}.

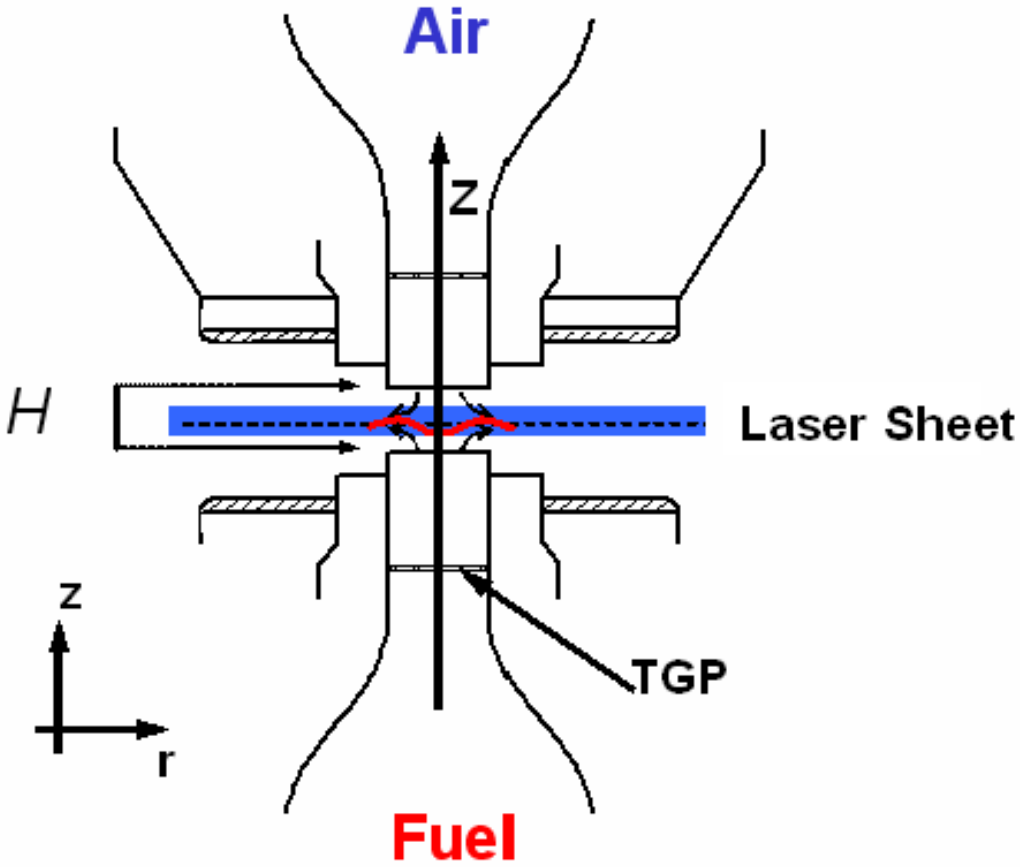

Figure 7.1: Schematic diagram of the Darmstadt Turbulent Opposed Jet Burner. Z is the burner axis, lower and upper nozzles are located at Z equal to 0 and 30 mm respectively. The burner stagnation plane Z_{st} is situated at the center between the nozzles, Z_{st} equal to 15.

A rich fuel-air flow exiting from the lower nozzle impinges on a pure air flow coming from the upper nozzle, resulting in the stabilization of a turbulent flame in the vicinity of half the distance between the burner nozzles. The nozzles are separated by a distance H=30 mm resulting in a ratio H/D_{in}=1.0. The fluid flows through perforated plates located at 50 mm upstream of the nozzle exit and acting as turbulence generators. They consist of hexagonally arranged round

holes with a blockage ratio of 45 % and a hole diameter of 4.0 mm. Contoured nozzles upstream of the perforated plates ensure uniform inflow condition at the perforated plates.

7.3 Flames Measured

Premixed and partially premixed methane/air mixtures at different equivalence ratios (i.e. ϕ=3.18, 2.0, 1.6, and 1.2) are used as fuel. Without additional mixing with air from the upper nozzle these mixtures are outside the flammability limits, except for the ϕ=1.2 case, and therefore burning is similar to non-premixed flames. Using an equal momentum for the flow rates of the two opposing flows the stagnation plane is established half way between the nozzle.

Reynolds numbers (Re), based on the bulk velocity at the oxidizer nozzle exit and the nozzle diameter D_{in} are varied between 3300 and 7200 as shown in table 7.1. The highest Re-number for the respective equivalence ratios ϕ=3.18 and 2.0 correspond to flames that do not burn for a time duration longer than 30 seconds in 100 subsequent runs. These flames are described as extinguishing.

Re_{air}	$a_m(1/s)$	$\phi\equiv$3.18	$\phi\equiv$2.0	$\phi\equiv$1.6	$\phi\equiv$1.2
3300	115	TOJ1A	-	-	-
4500	158	TOJ1B	TOJ2B	-	-
5000	175	TOJ1C	TOJ2C	TOJ3C	TOJ4C
6650	235	TOJ1D	TOJ2D	-	-
7200	255	-	TOJ2E	-	-

Table 7.1: Progression of turbulent opposed jet flames (TOJ) investigated in this study. The mean strain rate a_m is based on bulk velocity of the air side.

Table 7.2 shows flow field parameters for flame TOJ2D. Integral time scales are deduced from hot-wire anemometry measurements performed at the nozzle exits. Since the momenta of the two opposing jets were equal the stagnation plane was established at the half nozzle distance H/2. Accordingly, the bulk strain rate, $a_b = (U_{b,Ox} + U_{b,Fu})/H$, estimated with the bulk velocities U_b of both

Integral turbulent time scale τ_I	Integral turbulent length scale l_0	Turbulent Reynolds number Re_t	Kolmogorov length scale η_k
	l_0=u̇τ_I	$Re_t = \sqrt{k} l_0/\nu$	$\eta_k = l_0/{Re_t}^{0.75}$
1.1 ms	3.8 mm	95	0.13 mm

Bachelor Length scale η_B	Resident time t_{res}	Large eddy turn over time t_{ov}
η_B=$\eta_k/Sc^{-0.5}$	t_{res}=${a_m}^{-1}$	t_{ov}=$l_0/(2k)^{0.5}$
0.15 mm	4.3 ms	7 ms

Table 7.2: Flow field quantities for configuration TOJ2D.

gas streams was 231 1/s and the residence time in the mixing layers, $t_{res}= a_m^{-1}$, was 4.3 ms. The integral time scale τ_I=1.1 ms of the turbulent flow field 1 mm above the nozzle exit was computed from the autocorrelation function of hot-wire anemometry data. Utilizing Taylor's hypothesis the integral length scale, l_0, was calculated as 3.8 mm, which agrees favorably with the hole diameter of the perforated plates.

The turbulent Reynolds number, Re_t, for the air stream at the centerline is 95 based on l_0 and the turbulent kinetic energy, $k = 12(u'^2 + 2 * v'^2)$, where u' and v' are the axial and radial velocity fluctuations respectively, by assuming that radial fluctuations in both directions are similar. Note that velocity fluctuations in both directions double until the flow reaches the stagnation plane. Since the large-eddy turnover time, $t_{ov} = l_0 \ /(2k)^{\frac{1}{2}}$, $(t_{ov} = 7ms)$ is distinctly larger than the residence time in the mixing layers t_{res}, a 'young turbulence' emerges where the large eddies have not lost a significant part of their kinetic energy, which in turn leads to states of 'unmixedness'. Based on the Reynolds number and the integral length scale a Kolmogorov length scale, η_k, of 0.13 mm and the corresponding Batchelor length scale, η_B, was estimated as $\eta_B = \eta_k \ Sc^{\frac{-1}{2}} \approx 0.15$ mm (Sc Schmidt number).

7.4 Characterization of the Burner

A comprehensive experimental data set of turbulent partially premixed methane-air flames stabilized on a counter-flow geometry were investigated under project

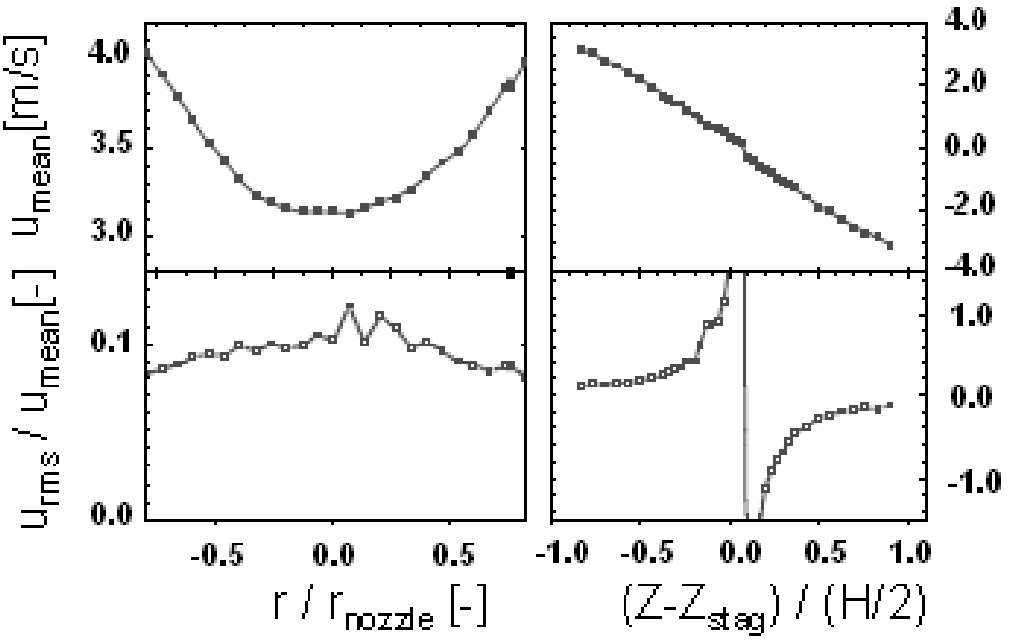

Figure 7.2: Axial velocity profile at nozzle exit (left side) and along centerline (right side) for Re=6650, $\phi = 2.0$. Upper part shows mean velocity, lower part normalized rms velocity [102].

SFB 568 in EKT [102]. This data set comprises information of the flow field, temperature, main species concentrations, scalar dissipation rate (in axial direction) and turbulent time scales. For these measurements a variety of diagnostic techniques have been used, including single-shot one-dimensional spatially resolved Raman/Rayleigh-scattering, Laser-induced Fluorescence and laser Doppler velocimetry.

Mean velocity flow field both at nozzle exit and along centerline along with normalized rms. velocity for flame TOJ2D are depicted in figure 7.2. Radial symmetry has been verified for both nozzles. Mean mixture fraction f and temperature T along center line is shown in figure 7.3. Experimental data set evaluated from this burner via various non-intrusive laser-based techniques serves as a basis for numerical validation.

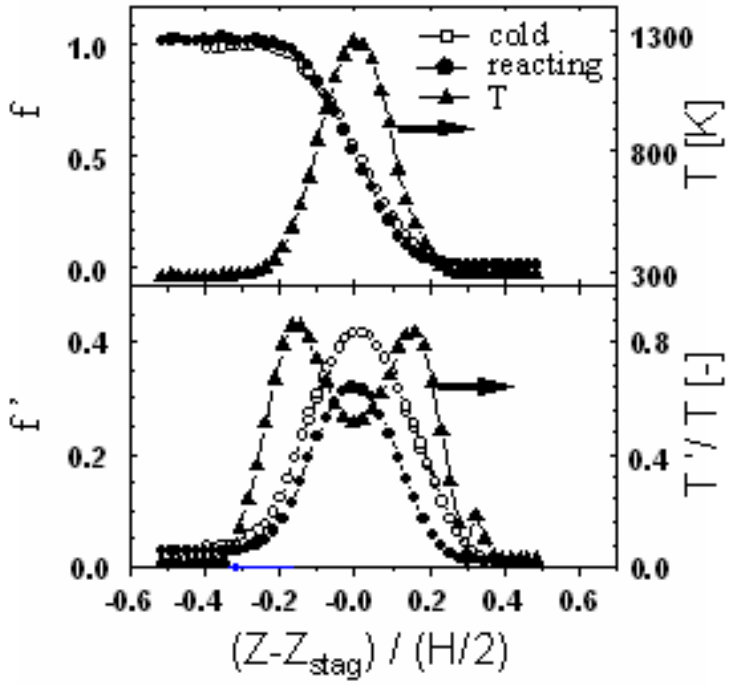

Figure 7.3: Mean and fluctuation of the mixture fraction f and temperature T along center line. Temperature fluctuations are normalized by the maximum temperature T = 1289K [102].

7.5 Result and Discussion

7.5.1 OH-PLIF

Figure 7.4 shows an example of processed flame image in a stable and extinguishing mode of combustion, that has been acquired during these measurements. Several flame characteristics have been evaluated to get an idea on the interaction of turbulence in a reacting scalar field.

7.5.1.1 Flame Area

Information about flame properties such as global and local areas of the spatial OH distribution, were obtained. Transient information about turbulent structures were obtained from the binary image, which was generated from a pro-

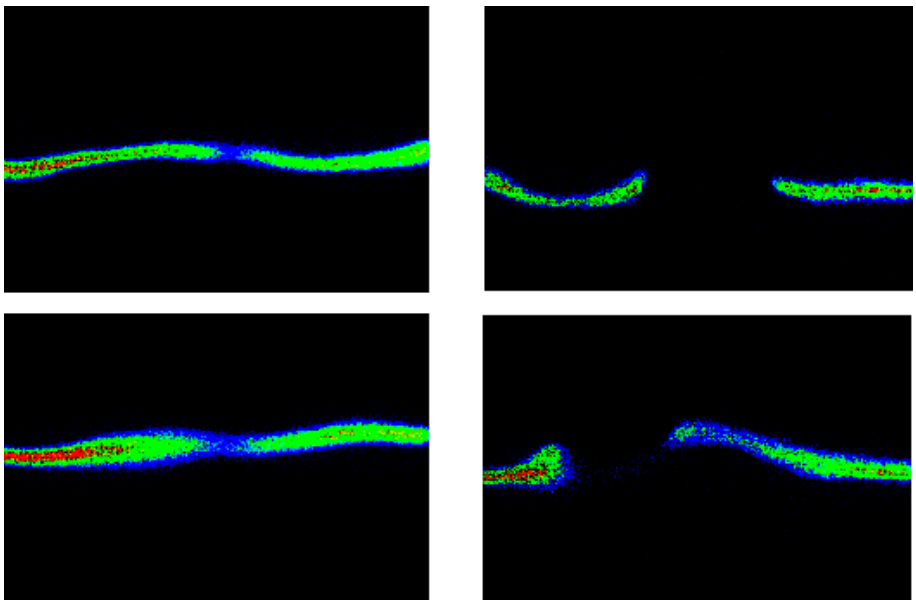

Figure 7.4: An example of typical two-dimensional images acquired from hydroxyl molecule from a opposed jet flames. Left column shows the flame defined by hydroxyl molecule in a stable configuration, whereas the effect of high turbulence that lead to flame extinction, can be seen in the right columned images.

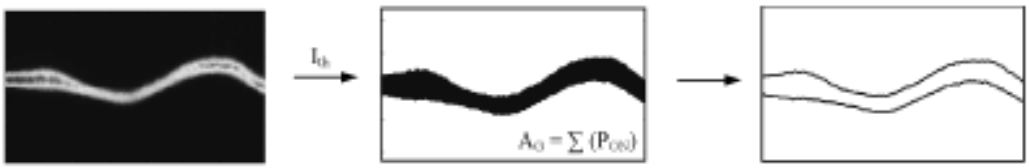

Figure 7.5: Processing of a binary image and contour of the OH layer from an intensity image. Threshold value applied is $I_{th} = 1$. Contour image shows both lower and upper OH contour

cessed image by applying a suitable threshold value on gray scale (see figure 7.5). Global flame area is calculated by counting all the "on" (pixel with value 1) pixels which are inside the flame front boundary.

The effect of Reynolds number variation for the case $\phi = 3.18$ and $\phi = 2.0$ is shown in figure 7.6(a). With increasing Reynolds number the global OH area decreases as expected, this is due to the increase in strain rate due to bulk

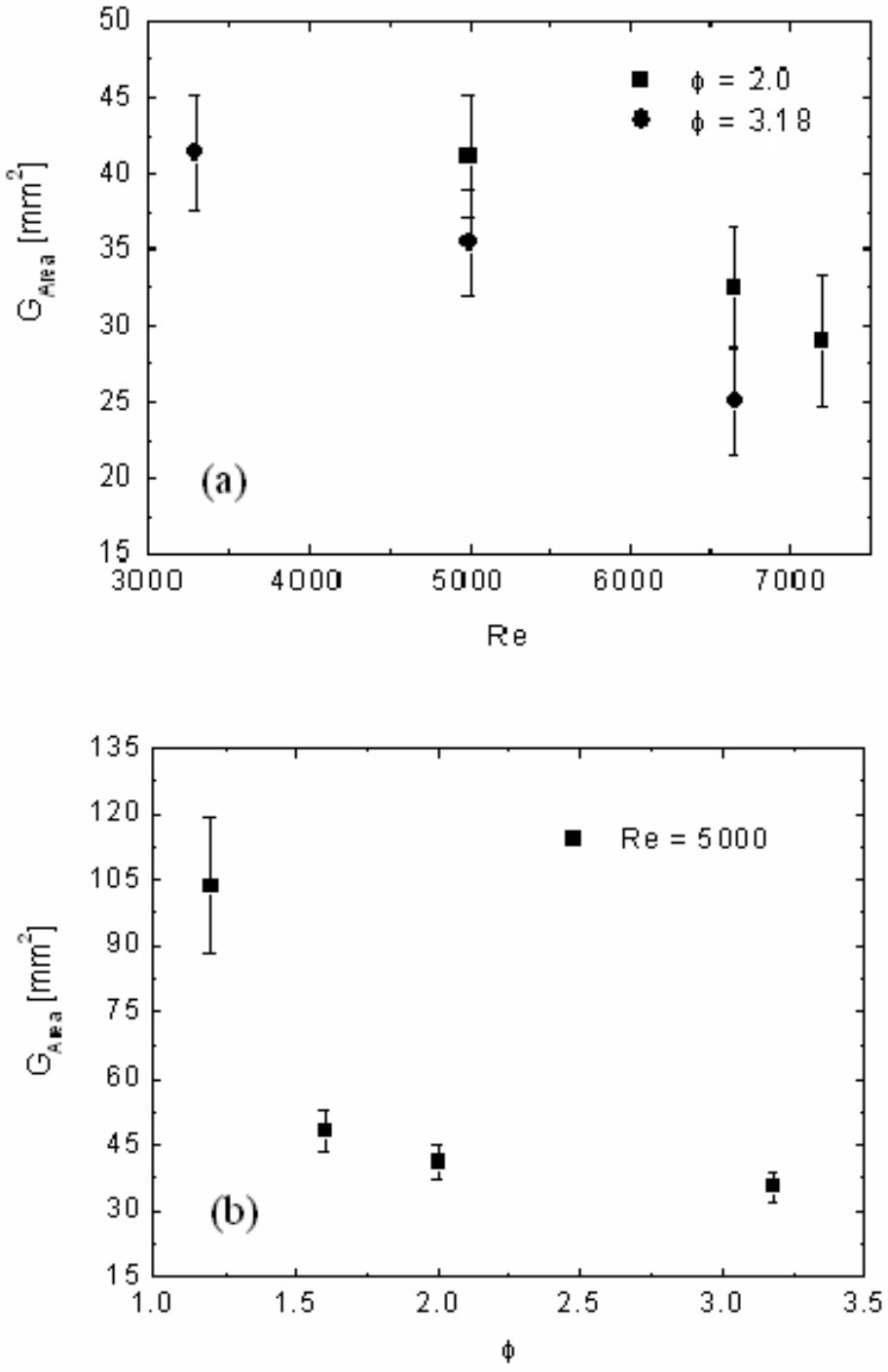

Figure 7.6: (a) Global OH area for varying Re-number at $\phi = 2.0$ and 3.18. Standard deviations are assigned by vertical bars (b) Global OH area for various flame configurations at Re = 5000.

velocity that results in compressing of the reaction zone and hence OH detection area. Taking $\phi = 3.18$ and Re =5000 and 7200 as an example, this decrease is approximately 20 %. In analogy to laminar opposed flames, the strain rate based on the bulk velocity increases with Reynolds number, in this example from $a_m = 175s^{-1}$ to $255s^{-1}$, compare table 7.1. Increasing strain rates stretches the turbulent flame and thereby increases scalar gradients, as exemplarily shown for laminar flamelets in figure 4.1.

Figure 7.6(b) shows the effect of different fuel compositions for a fixed Reynolds number of 5000 on the global OH area for a radial extension of 26 mm. The effect of premixing on global flame areas of partially-premixed flames was not pronounced. Only a small increase from 40 mm^2 for $\phi = 3.18$ to around $60mm^2$ for $\phi = 1.6$ was found, demonstrating that the last flame, that is still inside the rich flammability limit, shows a similar behavior compared to the partially premixed ones. Evidently, this effect can be attributed to short resident times due to mean strain rate as well as turbulent mixing. In contrast to this observation, a sharp increase in global flame area to approximately $105mm^2$ was found for the flame with the equivalence ratio of $\phi = 1.2$. That increase clearly indicates the transition from the regime where flame burns similar to non-premixed ones to the premixed regime. Two reaction zones exist where OH is created, first a rich premixed branch that supplies unburned hydrocarbons as fuel for a second non-premixed branch.

Standard deviations of global flame area are similar for all partially premixed flames (the configuration with $\phi = 1.6$ was also assigned to partially premixed), while again a significant increase is found for the premixed flames. It might be speculated that high transient strain rates of the turbulent flow occasionally cause a merging of the described two reaction branches to a single one, which would result in more extended OH distribution. Naturally, a broader distribution of the post flame gases will also contribute to the increased standard deviation and the flame itself.

To investigate the effect of flame stretching in more details, figure 7.7(a) shows local areas of the OH distribution that assign areas of hot combustion products. Local distribution was calculated using the progressing technique in horizontal direction of the PLIF images. First value of the distribution was calculated by taking a window of 4 column and averaging the pixel values (on pixels), this window was then shifted by a single pixel every step and the next averaged value

was generated. Various sizes of windows were tested for this case and the analysis showed that the results were not sensitive to the window size. The width of the window in terms of number of columns averaged was chosen as 5, 11, 15 and 25. This progressing procedure provides the complete local area distribution along the horizontal axis and provides the knowledge on flame front distribution.

For $\phi = 2.0$ and $\phi = 3.18$, figure 7.7 presents radial profiles for various Reynolds numbers. For all flame configurations an axisymmetric distribution was observed. This indicates radial symmetry of the flames and the burner. For all cases a local minimum was observed at r/R=0 and an increase of the local areas up to r/R=0.4. This spatial modulation in general was more pronounced for lower Reynolds numbers.

It can be concluded that the small increase of local flame area from the centerline outwards is most likely caused by the transport of hot combustion products in radial direction. Notice, that for $\phi = 2.0$ switching from Re= 6650 to 7200 the OH thickness at the centerline is nearly constant but for increasing radial position the Re= 6650 case shows increasing values. At higher strain rates the assumed transport process of the hot reaction products seems to be of less importance at larger radial positions for both fuel compositions, probably due to the decreasing overall width of the reaction layer. However, in order to verify these assumptions and in particular to explore the sharp drop for the $\phi = 2.0$, Re = 6650 configuration a simultaneous examination of the 2-D velocity and scalar field must be investigated.

The variances of local OH areas are spatially independent and only marginally influenced by the Reynolds number. By varying the equivalence ratio from $\phi = 3.18$ to $\phi = 2.0$ the variance is increased by the small factor of 1.5 that was already found for the global area and explained above. For a fixed Reynolds number of 5000, figure 7.8 exhibits local OH areas for equivalence ratio ranging from $\phi = 1.2$ to $\phi = 3.18$. A similar trend as presented for global OH areas in figure 7.6(b) was observed.

7.5.1.2 Flame Length

The position of the flame front is derived directly from binary images by an edge finding algorithm. The output of the algorithm is the contour of separate flame fronts from the binary image. Flame length in radial direction was calculated by

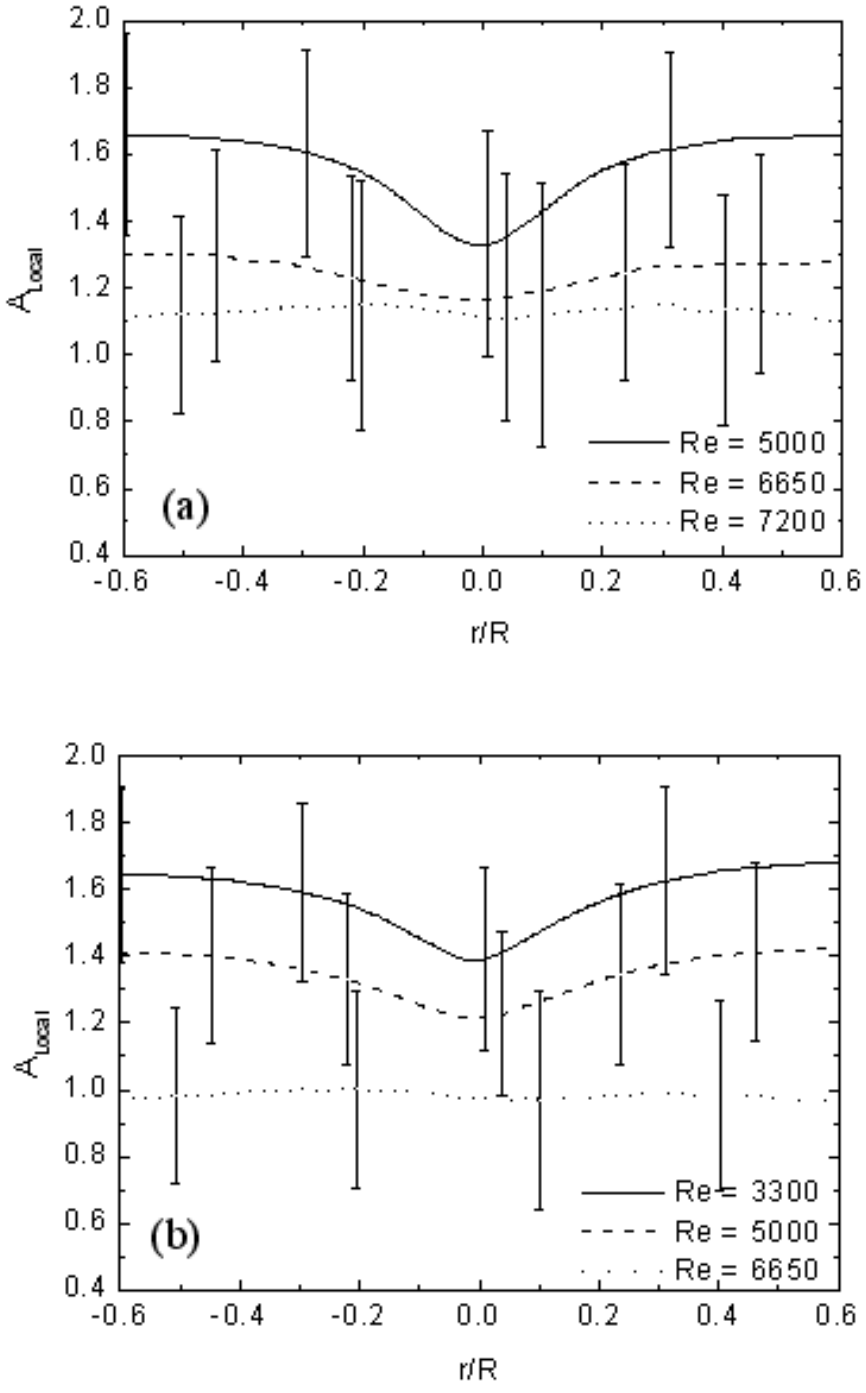

Figure 7.7: (a) Local area distribution in radial direction for varying Re-number at $\phi = 2.0$. (b) Local area distribution in radial direction for varying Re-number at $\phi = 3.18$.

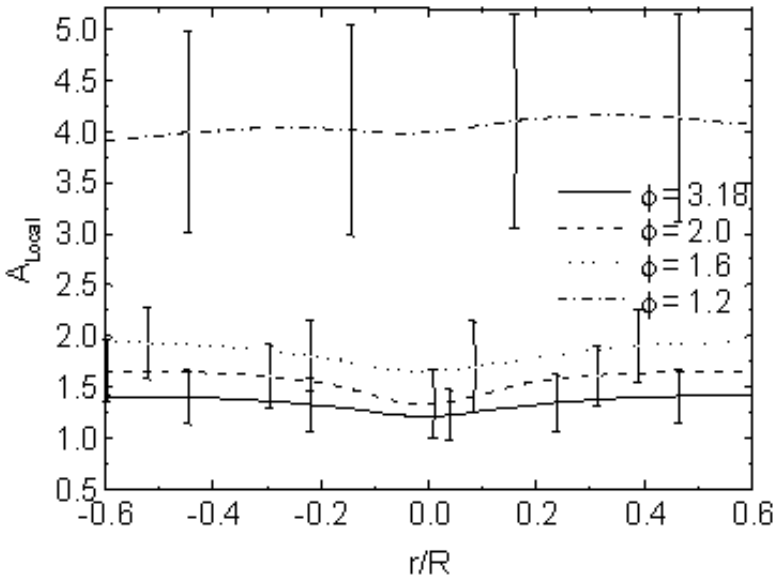

Figure 7.8: Variation of local area distribution in radial direction for different equivalence ratios at Re = 5000

counting the connecting pixel along the contour generated from the binary image. The algorithm used for this purpose is well known as matrix counting method. An example for counting the length of the flame front with this algorithm is depicted in figure 7.9.

This algorithm starts from the one edge and finds the position of the start pixel. In the next step it finds the connecting pixel by checking all the neighboring pixels in a clockwise direction as depicted and the length between the two connecting pixel is counted. Once it has located the connecting pixel, it fills the old pixel with the value that is not recognized in the forward step. This procedure assures that the algorithm counts only in forward direction. In addition, it avoids the algorithm routine to track and count reverse path. This algorithm progresses till the other edge of the frame is reached thereby giving the total length counted during the process.

For the total length of the stoichiometric contour line within the 26 mm wide monitored region the average length increases from 31.5 mm for Re=4500 to 33

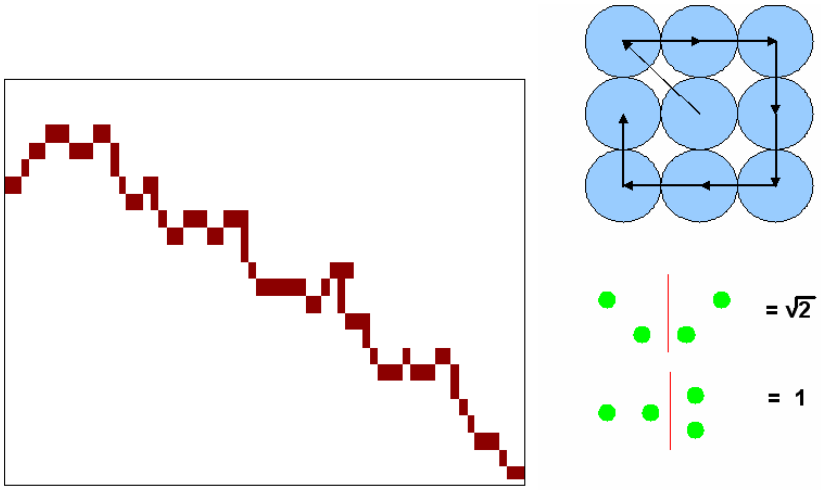

Figure 7.9: Matrix counting method for extracting length of the OH contour.

mm for Re=7200 respectively, using fuel with $\phi = 2.0$ (figure 7.10). Increasing the Reynolds number by a factor of 1.6 enhances global length of the contour line by only ~ 5 %. This observation is noticeable, because flame stability changed drastically from stable to extinguishing.

This result, however, indicates that flame stability is decreased not by small wrinkling but by the total flame stretching. Consequently, large scale eddies are the reason of flame extinguishing rather than small eddies that disrupt the reaction zone. This finding is in agreement with the time ratio $t_{res}/t_{ov} < 1$ indicating "young turbulence". For the $\phi = 3.18$ case very similar results are observed.

7.5.1.3 Position of Stoichiometric Contour

As discussed in chapter 3, the lower flame front defined by OH molecule can be used as a good approximation for predicting the location of stoichiometric contour. Therefore in this work, the mean stoichiometric contour as defined by lower flame front was extracted from OH-PLIF images. This is done by plotting all the perimeters of the lower flame front from instantaneous images on top of each other.

In contrast to the local area distribution (see figure 7.7 and 7.8), the averaged

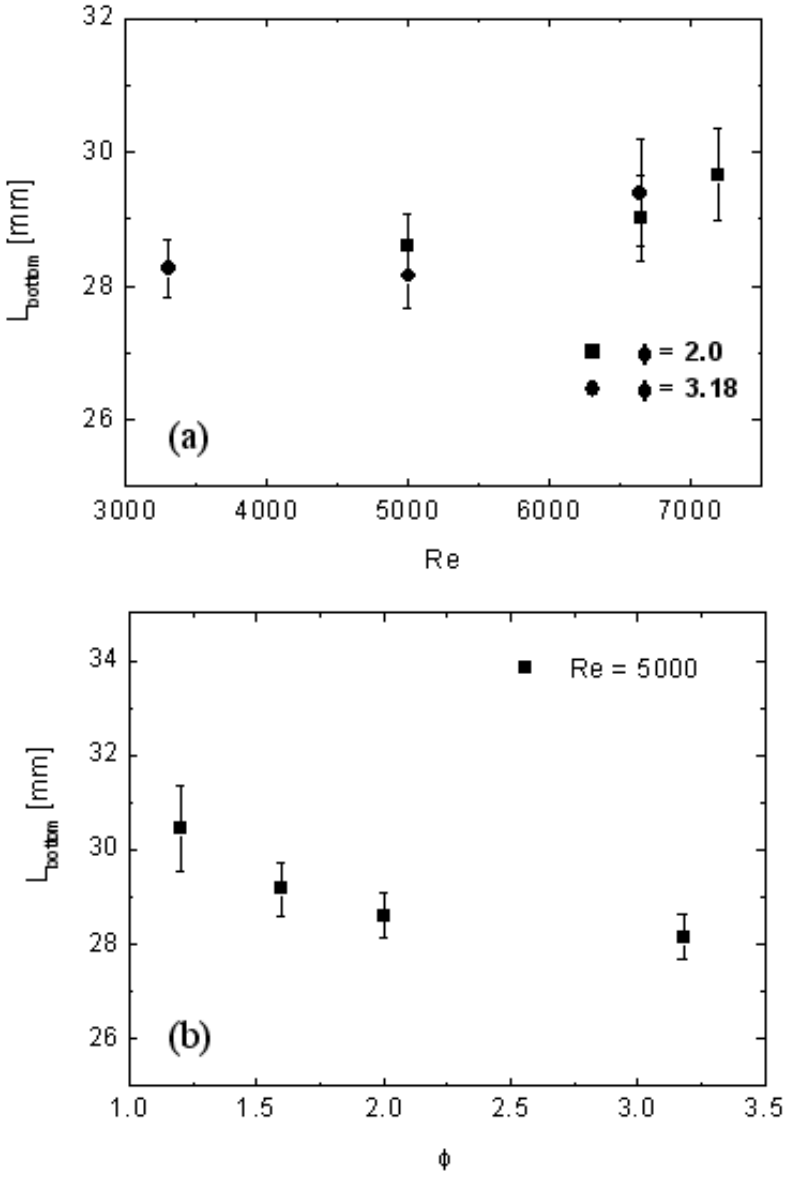

Figure 7.10: Mean flame length evaluated from a window of 26 mm in radial direction for (a)Various Reynolds number for equivalence ratio at 2.0 and 3.18, (b)different equivalence ratios at Re = 5000.

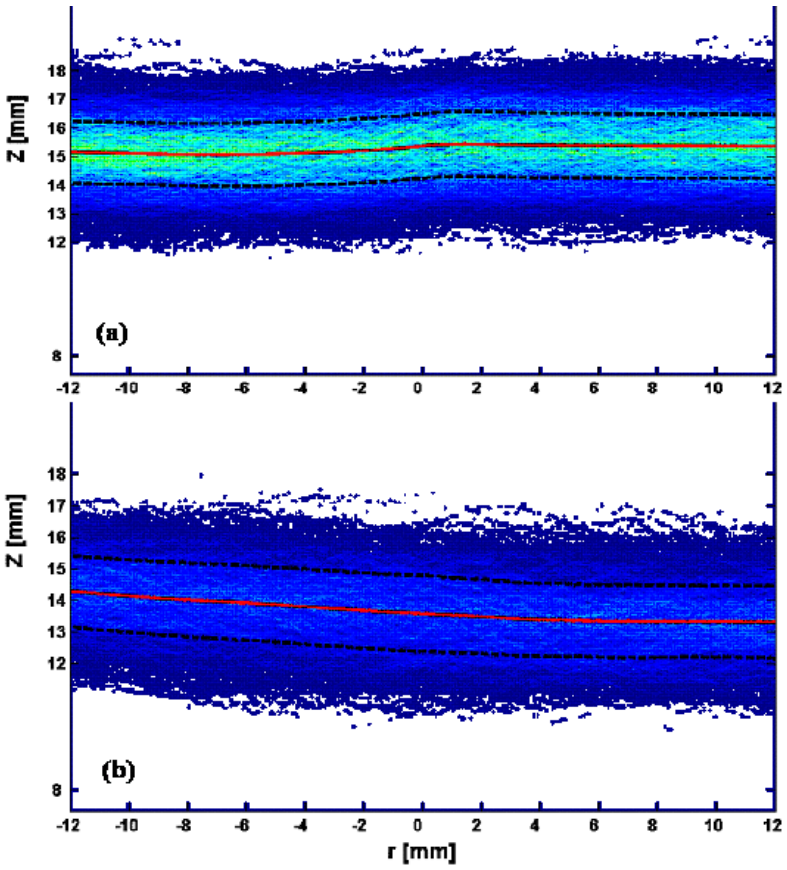

Figure 7.11: Two-dimensional probability of occurrence of the stoichiometric contour line for the $\phi = 2.0$ case. (a) Re = 5000, (b) Re = 7200. Highest probability correspond to dark-grey. Solid line marks mean position, dashed lines standard deviation.

shape of the lower OH contour in figure 7.11 that serves as an estimate for the stoichiometric contour, shows a flat appearance. This indicates a flow field that is also flat in average.

The transient position of the contour line is used to extract the two-dimensional probability of occurrence (2D PDF). For $\phi = 2.0$ and Re = 5000, in figure 7.11 a 2D PDF is presented including the mean location and plus/minus one standard deviation of the stoichiometric contour in centerline direction. For the Re = 5000 case the mean as well as the constant standard deviation of 1.1 mm are horizontally aligned, the first coincides with the geometric stagnation plane (z = 15 mm). Simulations with statistical turbulence models in counter-flow flames

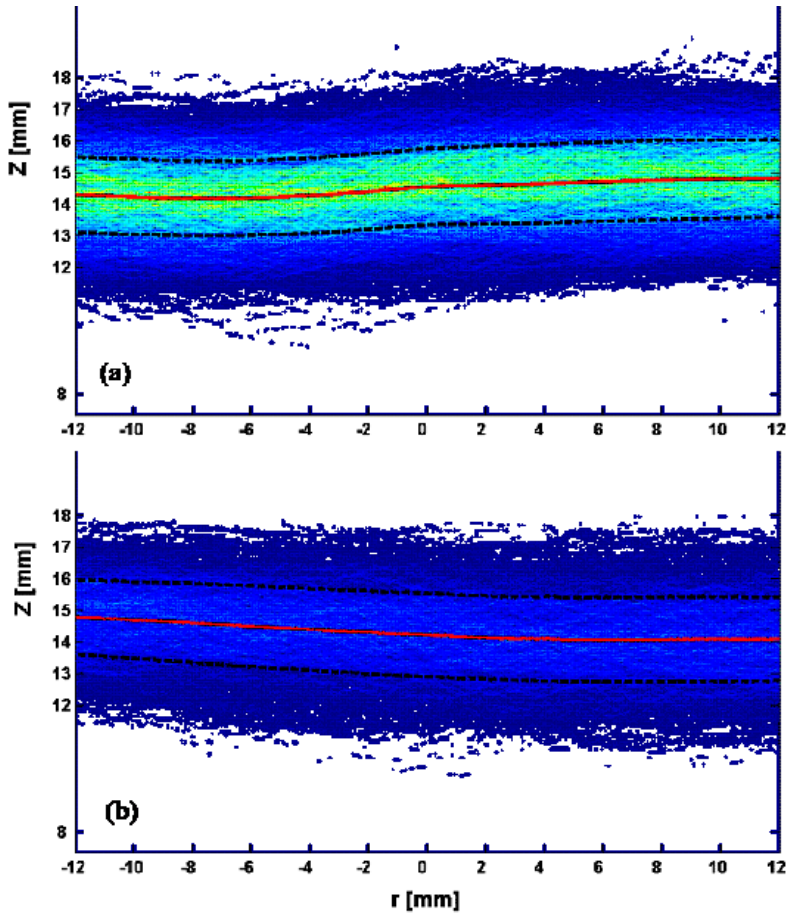

Figure 7.12: Two-dimensional probability of occurrence of the stoichiometric contour line for the $\phi = 3.18$ case. (a) Re = 3300, (b) Re = 6500.

are based on the assumption of a flow and scalar field that is only a function of the centerline coordinate [89],[97]. This assumption is in excellent agreement for the whole radial range of OH distributions shown in figure 7.11(a). Even if the OH distribution is slightly tilted for the configuration with Re = 7200 (figure 7.11(b)), the flame is at the extinction limit, the distribution of OH around the mean position is again parallel aligned for the whole radial range.

Compared to the upper figure, an increase of the turbulence level is reflected by a wider distribution of the OH contour around the mean position, the standard deviation is about 10 % higher. The finding that strain caused by transient large scale eddies as the most important reason for extinction in the presented counter-

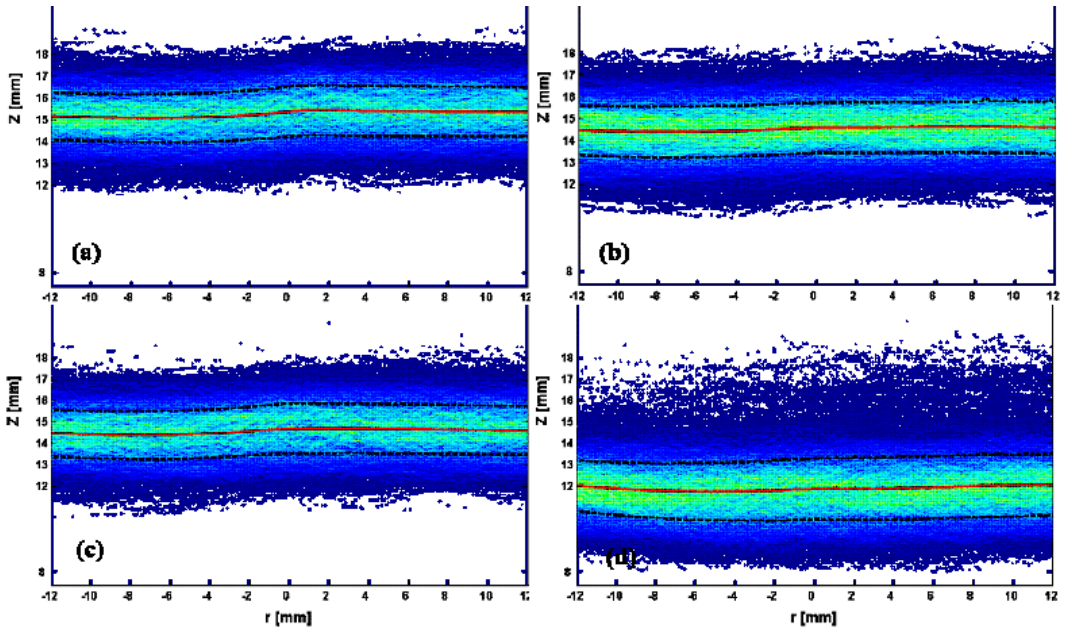

Figure 7.13: Two-dimensional probability of occurrence of the stoichiometric contour line for the Re = 5000. (a)$\phi = 3.18$, b)$\phi = 2.0$, c)$\phi = 1.6$, d)$\phi = 1.2$

flow configuration is thereby supported, since only large scale eddies will be able to enforce the motion of the stoichiometric contour, for instance by compressive straining. This enforced motion leads to increased strain rates and gradients of the mixture fraction causing local and global flame extinction.

As the length of the stoichiometric contour line is nearly independent of the Reynolds number and the equivalence ratio, the results indicate that the mechanism of flame extinction is driven by strain effects rather than severe wrinkling. This finding is supported by the fact that residence times are relatively small compared to large eddy turn over times. Therefore, turbulence is not fully developed.

7.5.1.4 Local Flame Angle

Instantaneous flamelet orientation angles have been previously calculated from the OH-PLIF images by Lachaux *et al.* and I.G. Shepherd in the turbulent premixed methane-air flames [103] [94] [104]. This angle is defined as the angle between the normal to the flame front surface and the plane tangent to the

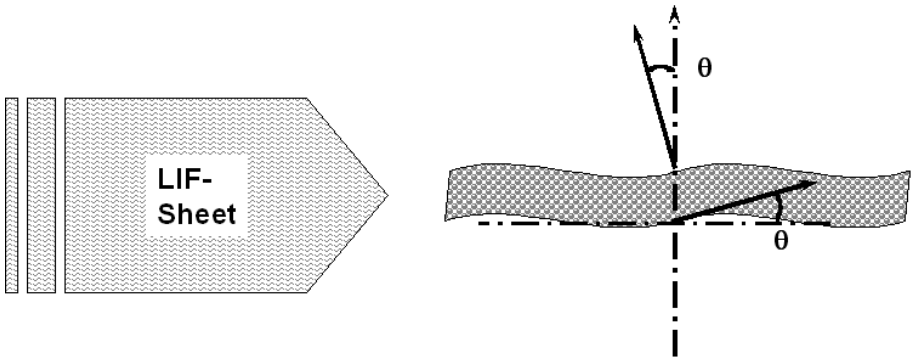

Figure 7.14: A schematic figure representing the flame angle at a point on a flame contour

contoured surface. In these measurements flame orientation angle is taken as the angle between the fixed laser horizontal sheet and local tangent of the flame front as can be seen from the figure 7.14. Additionally, the mean contour of the stoichiometric contour defined by the lower OH layer of the current flame are horizontally flat for the flames measured, which can be well concluded from the previous sub-section.

The local tangent of the instantaneous flame front was obtained in the following manner:

1. A window was chosen in the bottom flame front contour
2. Flame front was checked for any discontinuity
3. Parameterizing the points chosen in the flame front
4. Fitting and interpolating with B-Spline curve
5. Calculating the tangent angle from the first derivative of fitting curve

Once the window is chosen for the fitting routine and the check for the broken flame front is made, second-order parameterizations of the flame front was done along the distance s. Parameterizations includes the extraction of x(s) and y(s) for more than 100 points along the flame front, where s is the distance along the flame front. More points were taken in order to get the better fit with the evaluated points.

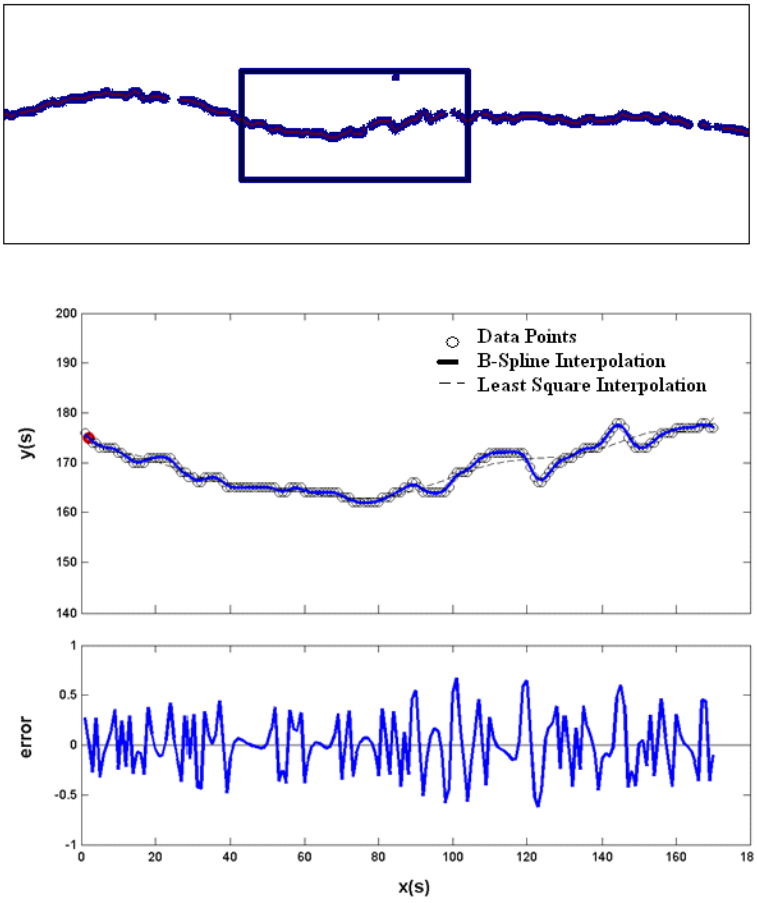

Figure 7.15: An example of fitting function applied on the bottom contour of the OH-PLIF image.

A step-wise B-spline fitting routine was applied to the single values in x(s) and y(s) direction's. The choice of B-spline was made as fitting functions for two reason, firstly the B-spline remains smooth along the edge points in contrary to other polynomials thus adding to the error in calculation. Secondly the B-spline is not biased towards any offset single point but follows the path of the chosen points since it is a stepwise and progressing fitting function. Once the function is defined, angle at a point in the function is defined by (eq.7.1).

$$\theta = tan^{-1}(\frac{df(s)}{ds}) \tag{7.1}$$

where f(s) is the fitted function for the given set of data points x(s) and y(s)

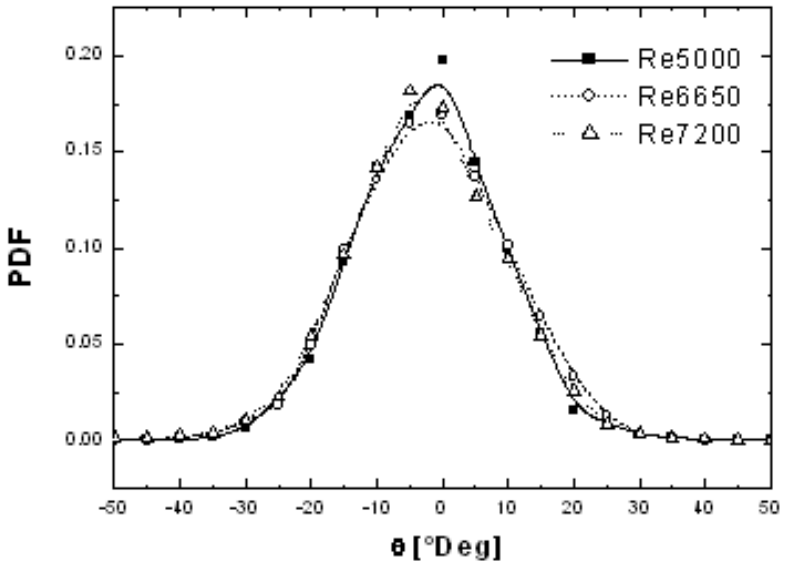

Figure 7.16: PDF of angle distribution at the burner center-line for varying Reynolds number for $\phi = 2.0$

directions. Since we were interested in calculating the angle at the center-line of the burner axis, no further smoothing of the profile other than non-linear filtering was done. The flame front in the region of the center-line was more wrinkled than the flame region radially outwards. Therefore, it was presumed that small structure were smoothed out by the application of non-linear diffusion filtering and the stable situation was reached.

Figure 7.15 shows an example of the data points and the fitting routine applied to it. Angle results were highly dependent on the fitting routine. The flame angle for the fuel side flame contour at the point along the burner axis was calculated. The angle PDF was found to be symmetrical for all flames and centered around 0° [figure 7.16, figure 7.17]. Flame angle was also calculated at the distance of 1 mm offset from the burner center-axis and similar symmetry was found [figure 7.18] (see page 100-102).

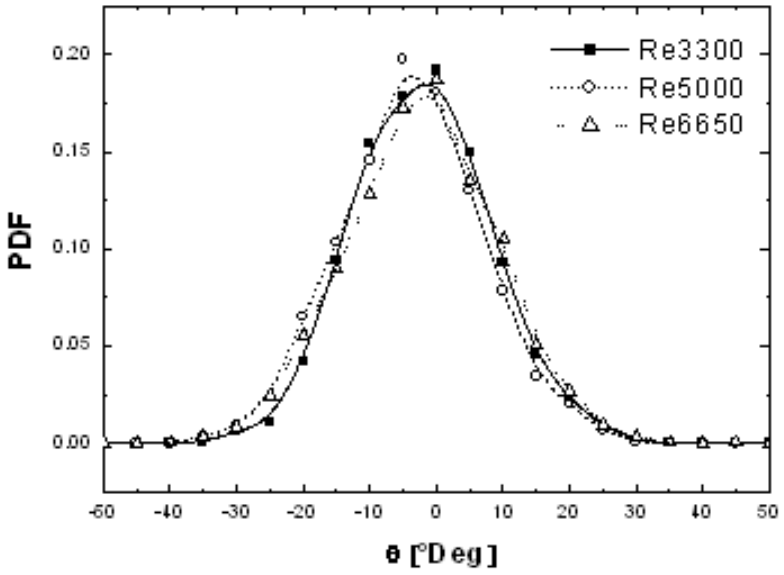

Figure 7.17: PDF of angle distribution at the burner center-line for varying Reynolds number for $\phi = 3.18$

7.5.1.5 Conclusion

Investigating local and global flame front characteristics yielded insight to the flame symmetry, its extinction properties, flame location and flame length. The results indicate that with increasing equivalence ratio the global and local OH area decrease. Decreasing OH areas are showing a higher sensitivity with respect to flame extinction. Results here also shows that flame length alone can provide the qualitative information on the stage of turbulence. As these results show that the diminished influence of small eddies in flame front indicated by no drastic change in flame length, confirms the presence of "young turbulence".

As the length of the stoichiometric contour line is nearly independent of Reynolds number and equivalence ratio, the results indicate that the mechanism of flame extinction is driven by strain effects rather than severe wrinkling. This finding is supported by the fact that residence times are relatively small compared to large eddy turn over time. Therefore, it reconfirms that the turbulence is not

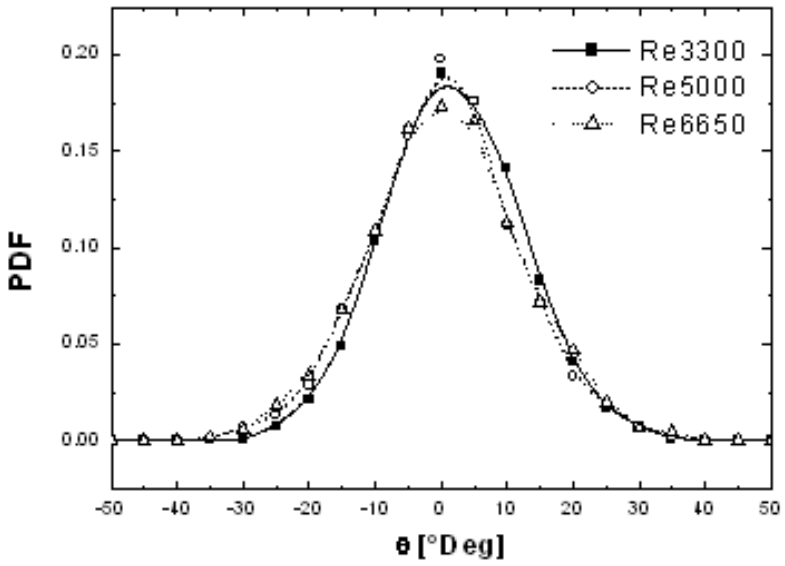

Figure 7.18: PDF of angle distribution at $1mm$ offset from burner center-axis for varying Reynolds number for $\phi = 3.18$

fully developed.

Similarly local area distribution provides the information on radial symmetry and spatial distribution of the flames. All these information can be very useful for model validation purposes, which indirectly can be used to optimize the burner design. These flame front characteristics results have been useful to confirm the good design of the opposed jet burner, which could be used as a standard burner for investigating various phenomenon associated with turbulent combustion such as flame extinction and flame stabilization.

7.5.2 OH-PITLIF

In OH-PITLIF study, time-series measurements are utilized to determine temporal scales for hydroxyl fluctuations in a series of stable and extinguishing turbulent methane/air counter-flow partially premixed flames as listed in table 7.1. The time-series measurements are facilitated by picosecond time-resolved laser-

induced fluorescence (PITLIF), which directly accounts for potential variations in both the quenching rate coefficient and background flame emission.

Since OH is present in the high-temperature regions of the flame, the measured fluctuations in the OH layer represent those of the flame front inside and outside of the probe volume. Time-series statistics are presented that highlight the effects of multiple parameters on the dynamics of flame motion. Flame front crossings are suitably characterized by the OH intermittency, but instead highlights the presence or absence of OH. The presence of successive bursts in the time series can be interpreted as successive flame-let crossings, while the OH intermittency can be used to quantify the percentage of such crossings. The influences of bulk Reynolds number and fuel-side equivalence ratio on fluctuation time scales are then examined using the OH integral time scales.

7.5.2.1 Time-averaged Concentration Profiles

Figure 7.19 shows axial turbulent and laminar profiles of [OH], for different fuel-air compositions, obtained along the opposed-flow axis (z axis). The laminar profiles in mentioned figure are axially shifted to match their peak [OH] locations with the corresponding turbulent profiles. For all these PITLIF measurements the stagnation point is situated at value $z-z_{st}/(H/2) = 0$, lower nozzle and upper nozzle are located at $z - z_{st}/(H/2) = -1$ and $z - z_{st}/(H/2) = 1$ respectively.

Table 7.3 shows the axial location of peak [OH] measured in the turbulent flames and, the profile full-width at half-maximum (FWHM). For the highest degree of premixing (TOJ4C, ϕ_B =1.2), the computed laminar profile indicates the presence of two reaction zones corresponding to two OH peaks, as opposed to a single OH peak for the corresponding turbulent profile. For similar flames (ϕ_B = 3.18-1.60), PLIF measurements indicate that premixing has very little effect on global flame area. However, a sharp increase occurs in global flame area for $\phi_B = 1.2$ (TOJ4C), consistent with the measured axial [OH] region in figure 7.19 and table 7.3.

7.5.2.2 Time-series Statistics

Figure 7.20 shows the first 1s of time-series data collected for three $\phi_B = 2.0$ flames with different Reynolds numbers, ranging from stable to extinguishing, at the axial location of peak OH. These time series, collected at random, are typical

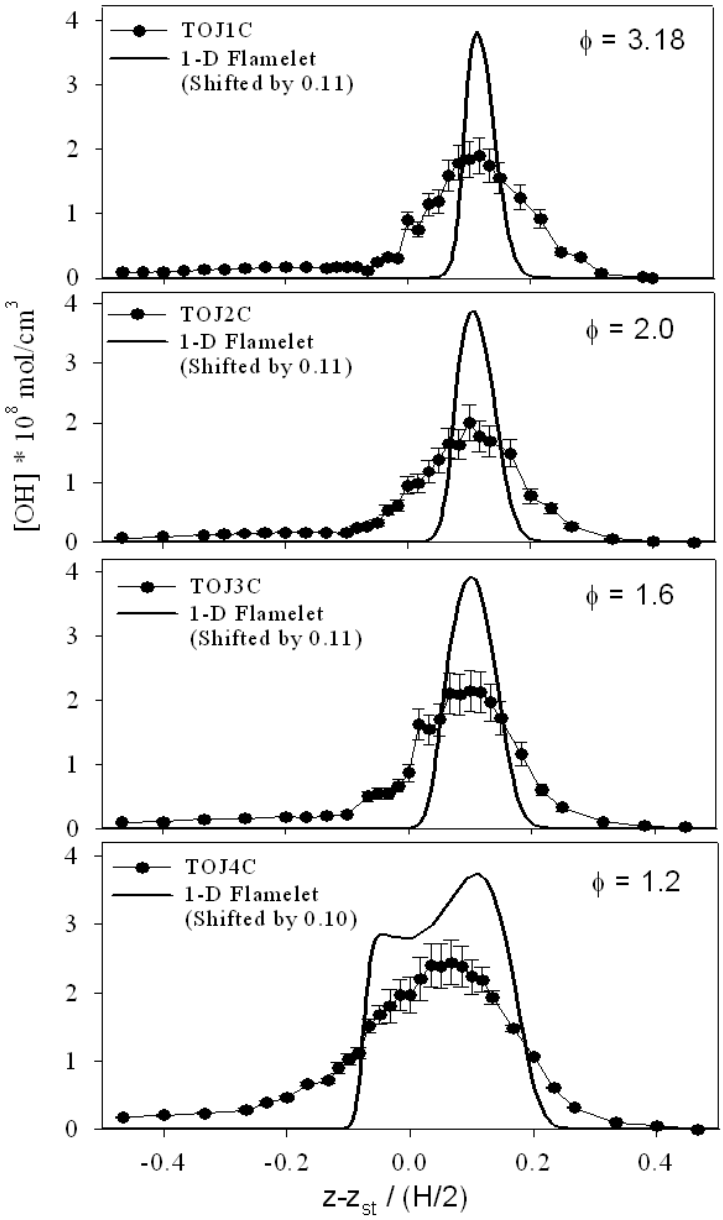

Figure 7.19: Axial profile of time-averaged [OH] for fuel-side equivalence ratios at Re = 5000, as compared with corresponding laminar profiles calculated from laminar code "OPPDIF". H represents the distance between the opposed nozzles. The accuracy for each measured concentration is ±18% (95% confidence interval of the mean). The stagnation point is situated at value $Z/(H/2) = 0$, lower and upper nozzle are located at $z - z_{st}/(H/2) = -1$ and $z - z_{st}/(H/2) = 1$ respectively.

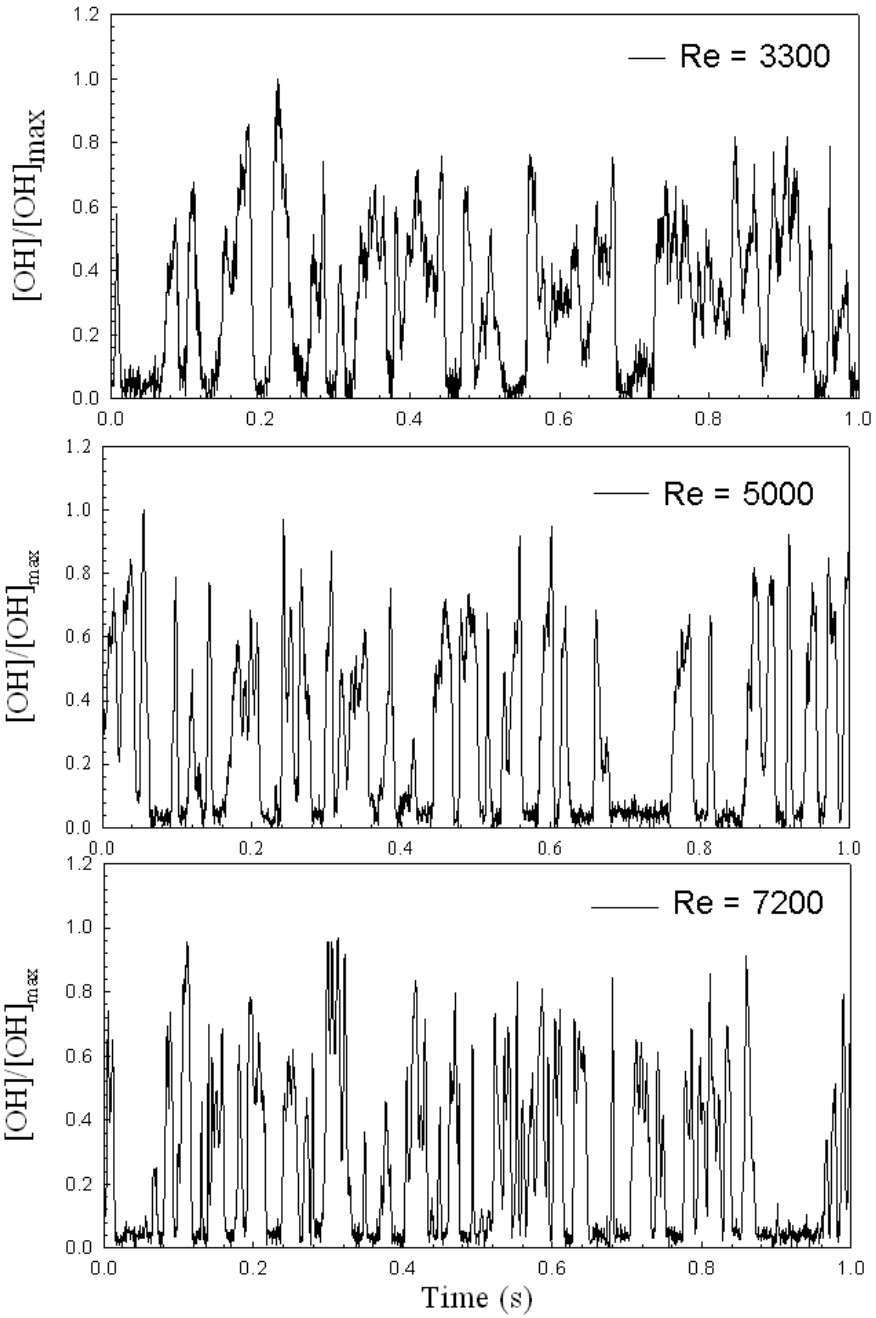

Figure 7.20: A snapshot of time series from flame with ϕ_B=2.0 (a) Re= 3300 (b) Re= 5000 (c) Re= 7200.

Flame	Axial location of peak [OH] z (mm)	FWHM (mm)	I (%)	Number of bursts/s
TOJ1A	15.25	2.70	39.5	31
TOJ2A	15.25	3.10	48.5	26
TOJ1C	15.50	2.54	44.8	43
TOJ2C	15.50	2.78	40.8	41
TOJ3C	15.50	2.70	27.3	32
TOJ4C	15.00	3.71	9.8	31
TOJ1D*	15.75	3.00	43.3	50
TOJ2D	15.25	2.97	40.4	50
TOJ2E*	15.65	2.53	48.0	43

Table 7.3: Time-series statistics at axial location of peak [OH] for different partially premixed flames. FWHMs are determined by Gaussian fits to the mean axial [OH] profiles, intermittency parameter (I) represents the probability of [OH] = 0 occurrences.

of the full 60 seconds of data obtained at each location and are normalized using the maximum [OH] from TOJ2C. The normalized [OH] for the TOJ2A flame typically exists for a longer duration in comparison to the TOJ2C flame. Similarly, the intermittent periods are also longer for the flame at lower Re. Hence, as the Reynolds number rises, the time-series bursts representing OH fluctuations become more rapid with reduced burst duration. Bursts in the OH time series are defined as those regions whose OH intensity values are greater than 15% of the peak intensity. The number of OH bursts per second increases from 26 at Re = 3300 to 43 at Re = 7200.

Time-series statistics for the different flame configurations at the axial location of peak OH are tabulated in table 7.3. The influence of turbulence on hydroxyl fluctuations can be studied by defining an intermittency parameter (I) which represents the probability of [OH] = 0 occurrences, i.e. for $I_{OH} = 1$ [OH]=0 and for $I_{OH} = 0$ high probability of OH occurrence. Intermittency equal to 1 represents the fully turbulent flow and with intermittency equal to 0 represents

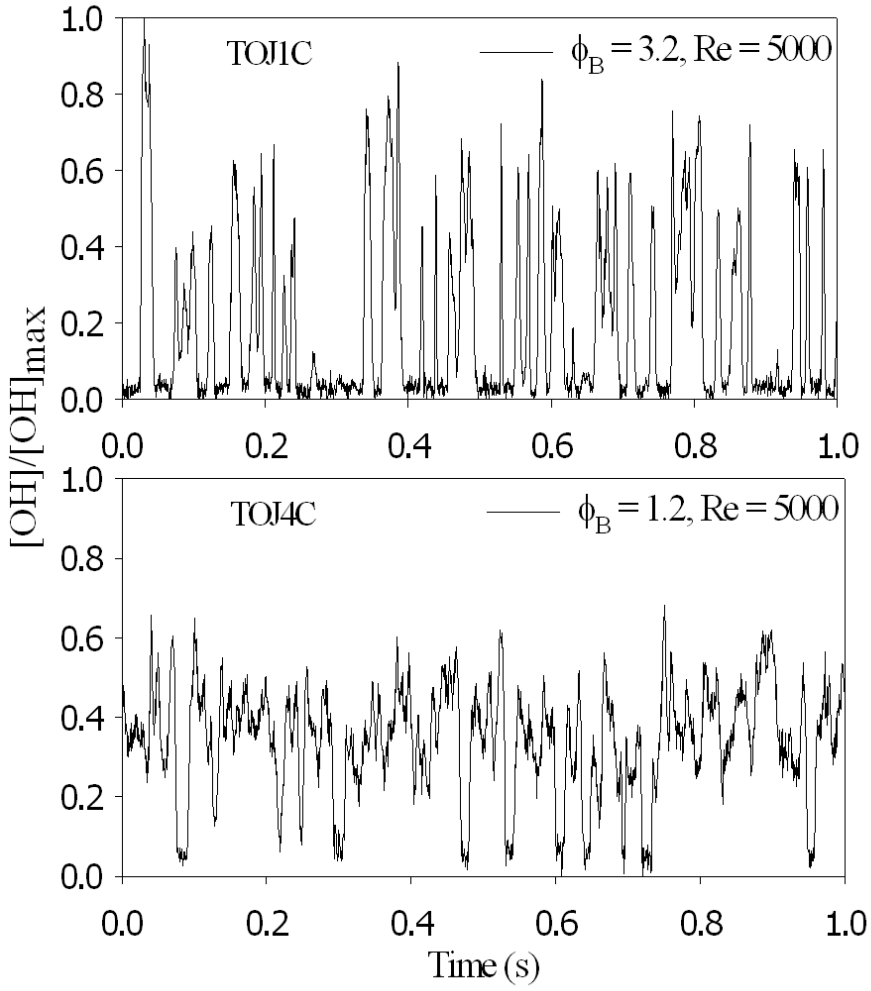

Figure 7.21: Sample time series of OH fluorescence for different ϕ_B at constant Re = 5000. These time series were measured at peak [OH] locations along the jet axis.

laminar flow. Because the time series is affected by shot noise and imperfections in background subtractions, a threshold value of 15% of the peak intensity was set below which the [OH] was assumed to be zero.

The OH intermittency (I) was found to be nearly constant despite a factor of 1.5 increase in Re (see table 7.3). The changes in intermittency parameter and OH profile FWHM, at the location of peak [OH], for various fuel-side equivalence ratios are shown in figure 7.22. Hydroxyl intermittency rises with increasing fuel-

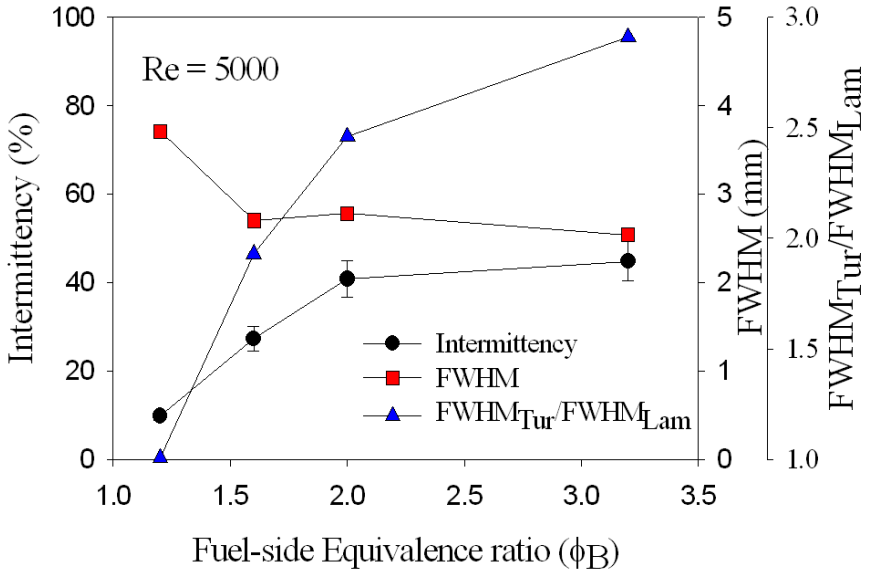

Figure 7.22: Intermittency parameter and turbulent OH profile FWHM and ratio of turbulent to laminar profile FWHM for flames at constant Re and varying ϕ_B

side equivalence ratio upto $\phi_B = 2.0$ and is almost constant for higher values of ϕ_B. As shown in figure 7.19, the flame with $\phi_B = 1.2$ has the broadest instantaneous OH structure owing to flame broadening at the rich premixed front. Since this mixture is within the flammability limit and very sensitive to local variations in strain rate [105],[106], the rich premixed front tends to propagate towards the fuel nozzle thus increasing the instantaneous width of the flame.

Figure 7.21 shows portions of the time series displaying fluctuations for flames with ϕ_B =1.2 and $\phi_B = 3.18$ at a constant Re of 5000. Because OH is present over a large spatial region at lower equivalence ratios, OH exists over a longer duration for the $\phi_B = 1.2$ flame as compared to the $\phi_B = 3.18$ flame. This greater OH presence is indicated by a more continuous distribution of the OH time series about its average. In comparison, for the flame at $\phi_B = 3.18$, the OH time series displays more intense but less frequent peaks. Though there are relatively fewer strong peaks in the time series for the $\phi_B = 1.2$ case, the average [OH] in this flame is higher than that in the $\phi_B = 3.18$ flame. It was also found that OH time series obtained at three axial locations in the TOJ4C (ϕ_B =1.2) flame exhibit

features similar to radial variations across the flame front reported for turbulent premixed jet flames in the thickened preheat regime [106].

7.5.2.3 Autocorrelation

Figure 7.23(a) shows unnormalized and normalized autocorrelation functions for flames at $\phi_B = 2.0$ with three different Reynolds numbers at the position of peak OH. As expected, the autocorrelation functions decay more rapidly with increasing Re. This behavior is due to the increase in fluctuations observed at higher Re, thus making successive OH values less correlated with time. Figure 7.23(b) again shows that the autocorrelation functions collapse onto a single curve when normalized by their respective integral time scales.

Both Renfro *et al.* [53] and Chaturvedy *et al.* [49] have previously reported this feature for turbulent jet flames. Hence, regardless of Reynolds number, the location in the flame and the amount of partial premixing [figure 7.24], the collapse of two-time statistics implies that the relative distribution of fluctuation rates at a single point in these turbulent flows is the same as that at a different point. Consequently, integral time scales are a good general representation of temporal fluctuations for OH (Renfro *et al.* [40]).

7.5.2.4 Integral time scale

The integral time scale τ_I is a function of axial position, fuel-side equivalence ratio (ϕ_B), bulk strain rate a_b, and Reynolds number (Re). If an integral time scale is specified, a normalized PSD or an autocorrelation function can be used to approximate the entire distribution of OH fluctuation time scales for different axial and radial positions in a flame. Hydroxyl integral time scales are found to be independent of radial direction. This result is in agreement with the usual assumption that in opposed-flow geometry, the velocity and scalar fields are only functions of the centerline coordinate (z axis). As seen in the OH-PLIF images, the two-dimensional probability of mean stoichiometric contour was also found to be horizontally aligned across the radial axis of the flame [see figure 7.11 in the section(7.5.1.3)].

The hydroxyl contour line shifts from the stagnation plane with various changes in Re and ϕ_B , but maintains its symmetric and planar structure. Figure 7.25 shows the axial variation of integral time scale and the intermittency parameter

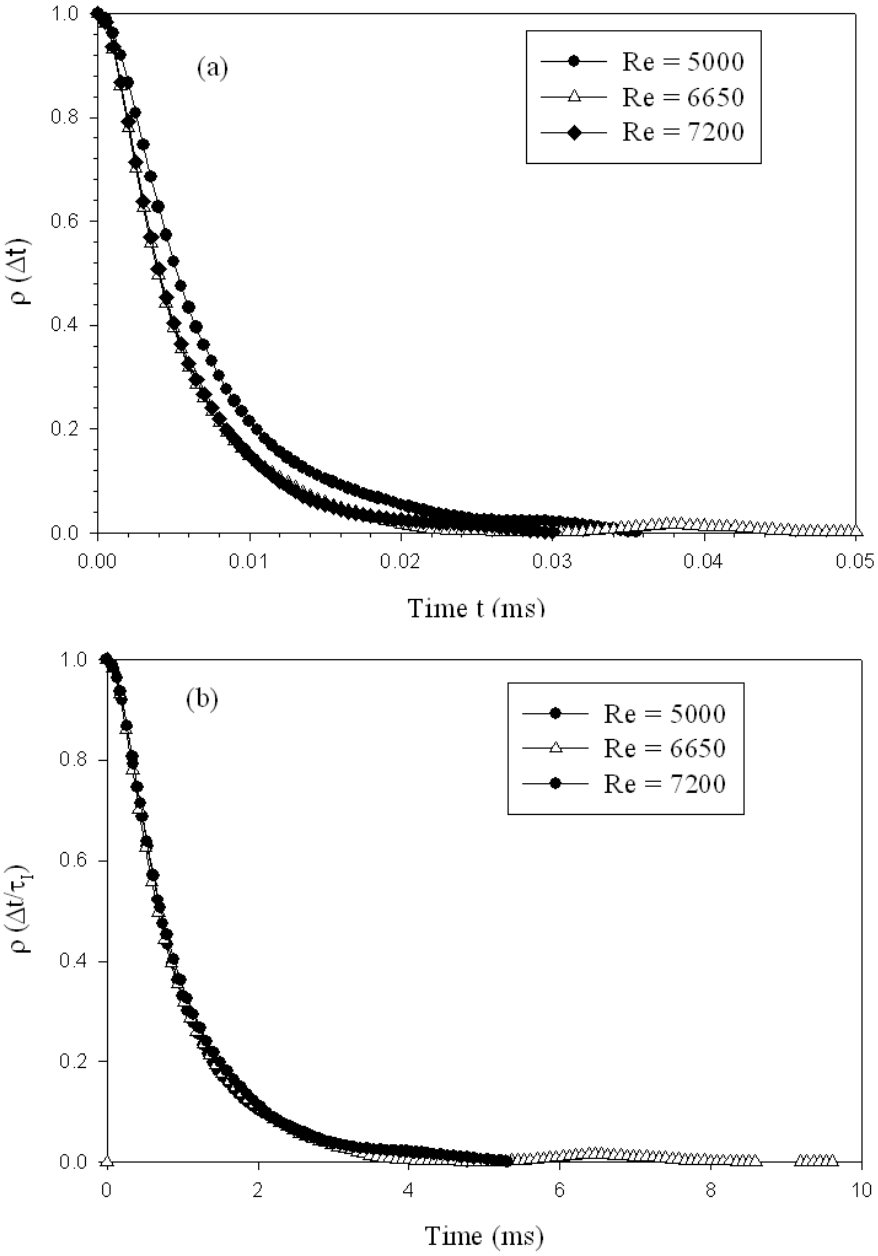

Figure 7.23: Autocorrelation functions for various Re at $\phi_B = 2.0$ (a) unnormalized and (b) normalized by their respective integral time scales.

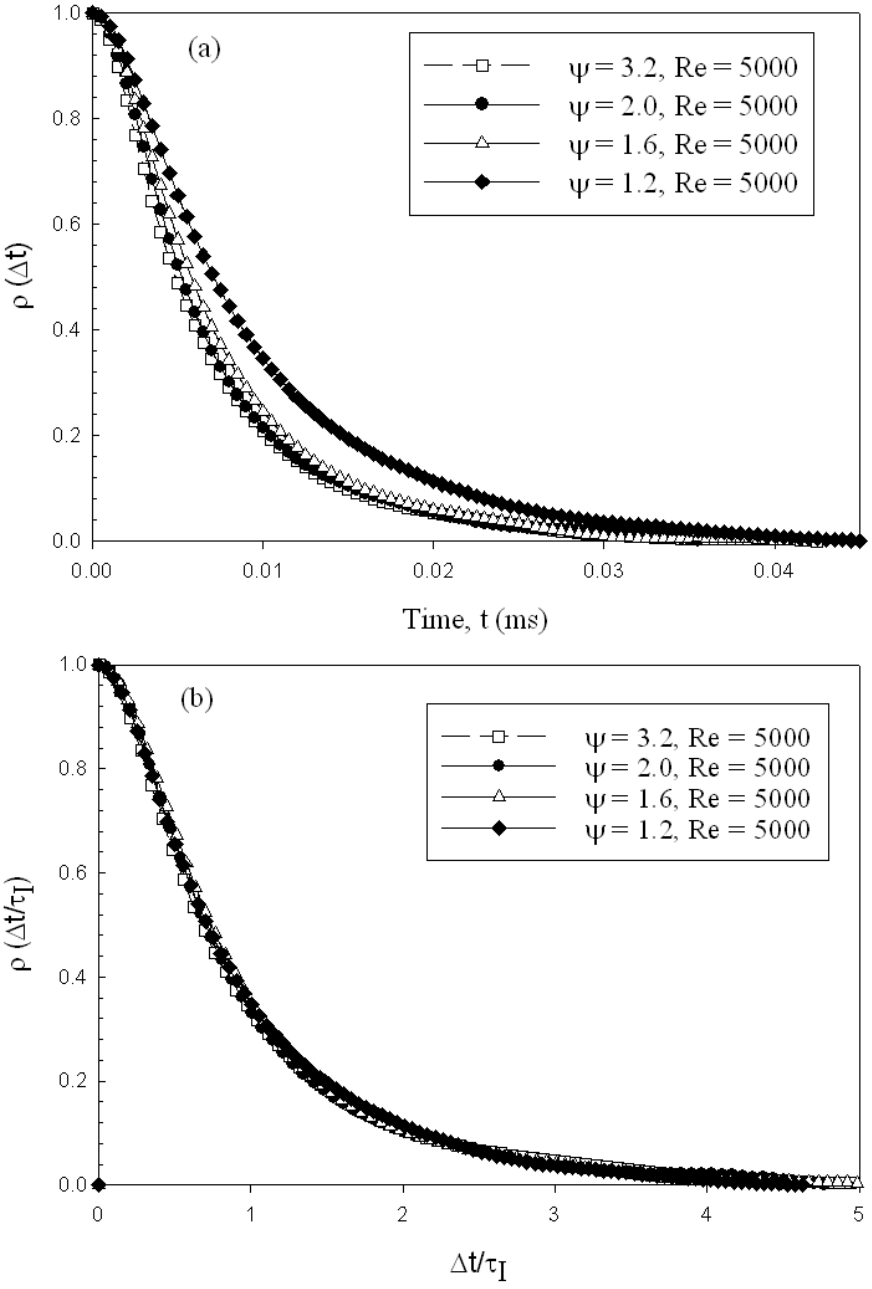

Figure 7.24: Autocorrelation functions for various ϕ_B at Re = 5000 (a) unnormalized and (b) normalized by their respective integral time scales.

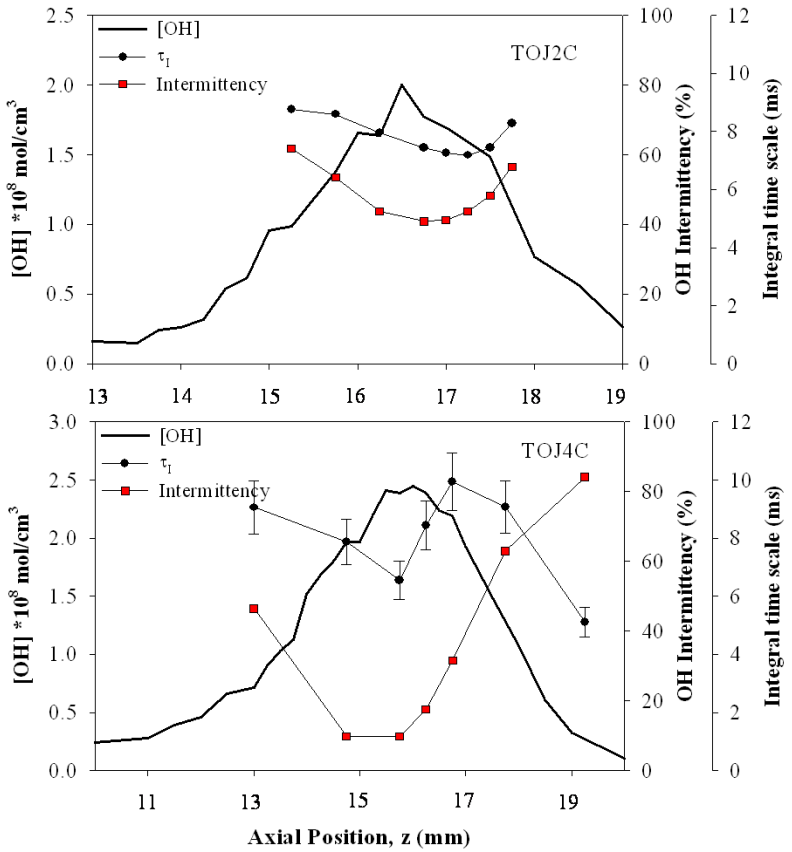

Figure 7.25: Axial variation of integral time scale and OH intermittency for flames with (a)$\phi_B = 1.2$ and (b)$\phi_B = 3.18$, at constant Re = 5000.

for flames at different Re. The hydroxyl intermittency and integral time scale reach a minimum near the axial location of peak OH. The lower value of OH intermittency at the location of peak OH indicates a high probability of OH occurrence. The axial variation in both OH integral time scale and intermittency for opposed-flow flames is similar to radial variations across the flame front reported for jet diffusion flames [53]. However, across the OH layer, the gradient of integral time scale for opposed-flow flames increases with decreasing fuel-side equivalence ratio. In fact, for the flame having the lowest fuel-side equivalence ratio (ϕ_B =1.2), the integral time scale exhibits a sinusoidal variation along the jet centerline.

7.5.3 Conclusion

Instantaneous OH layer thickness is smaller for flames having higher fuel-side equivalence ratios as shown by OH-PLIF results. The extent of spatial movement of the partially premixed flame front drops with enhanced premixing. For a flame with a equivalence ratio of 1.2, hydroxyl time series at peak [OH] exhibit very little scalar intermittency. This behavior is consistent with the presence of a broad instantaneous OH layer for this rich mixture. For the same flame, the intermittency at peak OH remains almost constant in going from stable to extinguishing flame. It was also found that OH time series obtained at three axial locations in the TOJ4C (ϕ_B =1.2) flame exhibit features similar to radial variations across the flame front reported for turbulent premixed jet flames in the thickened preheat regime.

Hydroxyl integral time scales are found to be independent of radial direction. The hydroxyl integral time scale reaches a minimum at the axial location of peak OH, consistent with measurement in jet diffusion flame.

8 Swirl Flames

This chapter presents realization of Paul's [55] work on imaging flame heat release rate in turbulent flames. This requires simultaneous measurement of two species namely hydroxyl and formaldehyde in the targeted flame. Current chapter is arranged in the similar way as the previous chapter on opposed jet burner. Introduction that includes literature survey on swirl-stabilized flames is followed by the burner description and the properties of the flame measured. Last section contains the results and discussion on the current measurement.

8.1 Introduction

Swirl flows are found in nature and are utilized in a very wide range of applications. In nature, the vortex shedding from the wings of an aircraft is the best example. In the reacting flows, most technical systems of practical interest such as gas turbine engine combustors, boilers, gasoline and diesel engines, industrial furnaces etc. involves large regions of recirculating flows. Swirled reacting flow has multi-fold advantages: it increases the efficiency of the combustion by accelerating the mixing of two flows (having different densities), it provides the reduced velocity necessary for flame stabilization and it also reduces the flame height which helps in the compact design of technical combustors. Therefore, above mentioned reasons are important enough to improve the understanding of such flows at various operating conditions.

Most of the research in the field to optimize the modern gas turbine engine is fuelled by the concept of lean premixed combustion, which demands a high ignition stability even in the mixtures of high air to fuel ratios. This can only be realized using swirl stabilization. A proper design of future low-NO_x combustors depends on more reliable numerical simulations of turbulent premixed combustion processes [107]. Although a variety of models for premixed flames exist such as Bray-Moss-Libby (BML) model, the thickened flame model, the linear eddy

model, or the G-equation approach, there is still an ongoing scientific debate on ways to model turbulent premixed flame. The numerical simulation for studying the effect of swirl on flow development and flame dynamics in a lean premixed swirl flame was recently done by Huang *et al.* [108]. This study showed a significant impact of the swirl number on the flame dynamics and the recirculation zone within such flames. Same study also showed a substantial turbulence-chemistry interaction involved in the turbulent flames on a swirl stabilized burner.

Because turbulence is considered to be mainly responsible for flame stabilization in swirl burners, extensive measurement of mean and fluctuating velocity components were performed before using laser based diagnostics [109],[8],[10]. Raman measurements were carried by W.Meier to investigate on the temperature and major species concentration in the same swirled natural gas flames. Several other groups have carried out velocity measurements and investigated time-mean and fluctuating temperatures and the concentration of stable species within the program "Arbeitsgemeinshaft TECFLAM". For these investigations a water-cooled combustion chamber with a variable swirl burner was used. These studies included research on the stability limits, pollutant formation, measurement techniques and numerical investigation of swirling flames [110].

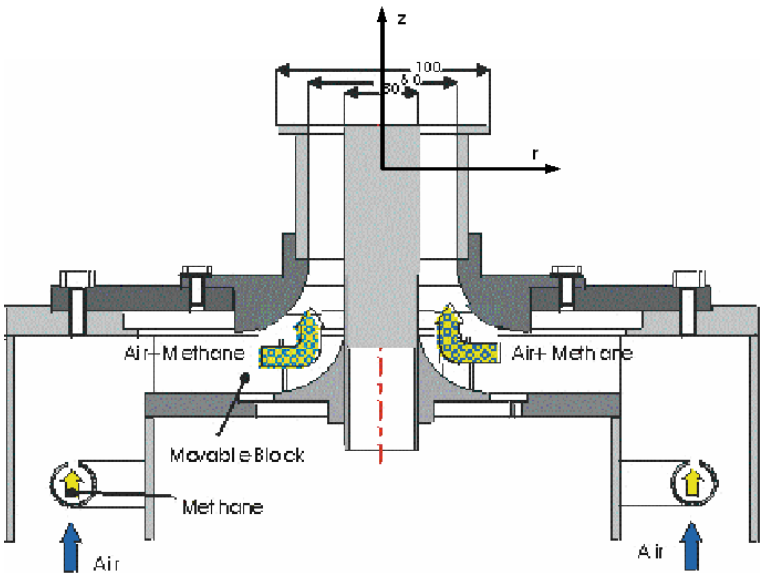

Figure 8.1: Schematic diagram of EKT swirl burner

These studies also aimed to provide a database of a swirl stabilized turbulent flame for validation of numerical simulation. More recently, turbulent-chemistry interaction was studied using a joint velocity/scalar measurement in the same target burner and natural gas as fuel [22].

Experimental investigation of heat release rate imaging on a non-premixed swirl flame was successfully carried by Böckle *et al.* [111]. This was done by measuring the flame flow field via simultaneous single-shot imaging of formaldehyde and OH molecule using PLIF. Present work also utilizes the planar technique in order to provide a snap shot of instantaneous reaction rate in a swirling flow field under the lean premixed mode.

8.2 Burner Description

Experiments were carried out with a burner that is designed with well-known Moveable-Block swirl generators. These generators are situated upstream of the nozzle and allow the adjustment of the theoretical swirl number $S_{0,th}$ ranging from 0 to 2.0. The theoretical swirl number is calculated using axial and circumferential momentum [22]. The fluid flow enters the moveable block in a radial direction and is injected radially upstream of the moveable block through eight nozzles, as can be seen from the arrows in the figure 8.2. This moveable block consists of upper and lower segments and each segment has a angular bend in radial direction. Turning the lower segment of the moveable block allows the burner to be operated at various swirl numbers. If the moveable segment is turned in such a way that the opposite edges of the radial bends of both segments lie on top of each other, then the $S_{0,th} = 1.98$ is reached.

The schematic diagram of the burner is shown in figure 8.1. This burner consists of a 15 mm wide annular duct that encloses a central bluff body with $d_b = 30$ mm. The premixed combustion mixture of fuel and air exits into the ambient atmosphere from this annular duct. About 70 mm upstream of the moveable block, a mixture of methane and air was injected into the air flow at 300 K using a perforated ring line. The co-flow fluid (N_2) surrounds the flame which provides the defined boundary condition and the protection from the particles. The co-flow exits through a duct with a diameter of $d_{cf} = 168$ mm diameter and a with the mean velocity of 0.5 m/s.

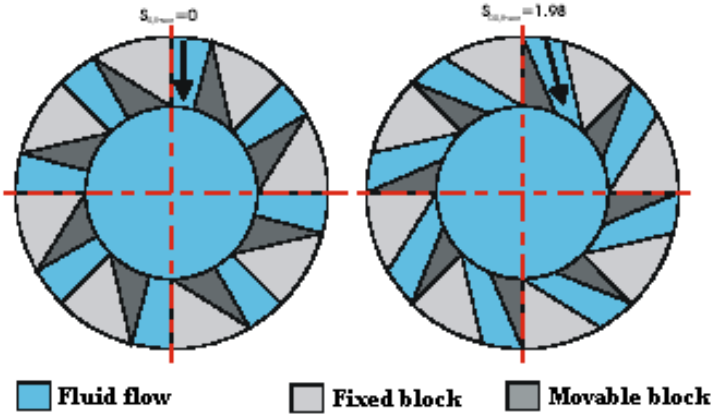

Figure 8.2: Configuring the swirl number from swirl generators situated in the burner. Left showing the configuration at no swirl (S=0) and right with S=1.98.

The investigated flame was operated close to the stability limit with $S_{0,th} = 0.75$ because theoretical swirl number $S_{0,th}$ exceeding 0.8 resulted in flash back. The operating conditions for the investigated flame are listed in table 8.1. PSF-30 represents the premixed swirl flame with power of 30 KW. Parameters ρ_u and ρ_u represents fluid density of unburned mixture and burned mixture respectively. Reynolds number is calculated using the bulk velocity of the fluid exiting through the nozzle and the hydraulic diameter.

8.3 Results and Discussion

The single shot images of the instantaneous [OH] and [HCHO] concentration were normalized to correct for the laser beam profile prior to any further analysis for results. Post-processing of images were also carried out which included filtering and smoothing as discussed in chapter-6. Image processing of the individual single-shot images of OH and HCHO was done separately.

Using images of the reference mask (grids) from both ICCD cameras, the field of view was carefully adjusted. After post-processing the camera matching was done. Camera matching included the spatial overlapping in horizontal and vertical direction of the images, so that the field of view for both the camera

		PSF-30
$S_{0,th}$	[-]	0.75
P	[kW]	30
$ø$	[-]	0.833
Q_{gas}	[m_n^3/h]	3.02
Q_{air}	[m_n^3/h]	34.91
Re_{tot}	[-]	10000
u'	[m/s]	2.5
s_L	[m/s]	0.36
u'/s_L	[-]	6.9
τ	[-]	5.8
ρ_u	[kg/m^3]	1.130
ρ_b	[kg/m^3]	0.165

Table 8.1: Details of flame configuration measured on turbulent premixed swirl burner

remains the same and also the tilt of the images. However, deviation in tilt was found to be in the sub-pixel range. These images were normalized by their maximum intensity before they were multiplied to generate the heat release rate intensities.

Figure 8.3 shows the single-shot images of OH, HCHO and multiplied intensity image from [OH][HCHO], these images were recorded simultaneously with separate detection systems in the lower part of the flame at a height ranging from 9-14mm. Hydroxyl molecule in the inner zone indicate the position of hot burnt gases that have been recirculated back to the burner center due to the recirculation zone formed by high intensity swirling motion. The position of the formaldehyde molecules indicate the fresh cold gases in the preheated zone and is formed near the shear layer between the high temperature burned gases in the recirculation zone and the outer fresh gases. The overlap area is the indicator of the location of a optimal reaction zone, where most of the chemical reaction is taking place. Typical formaldehyde concentration layer evaluated from our images was found to be around 1.5-2.5 mm. A profile is indicated in the figure 8.4 showing the overlapping of hydroxyl and formaldehyde. The intensity of

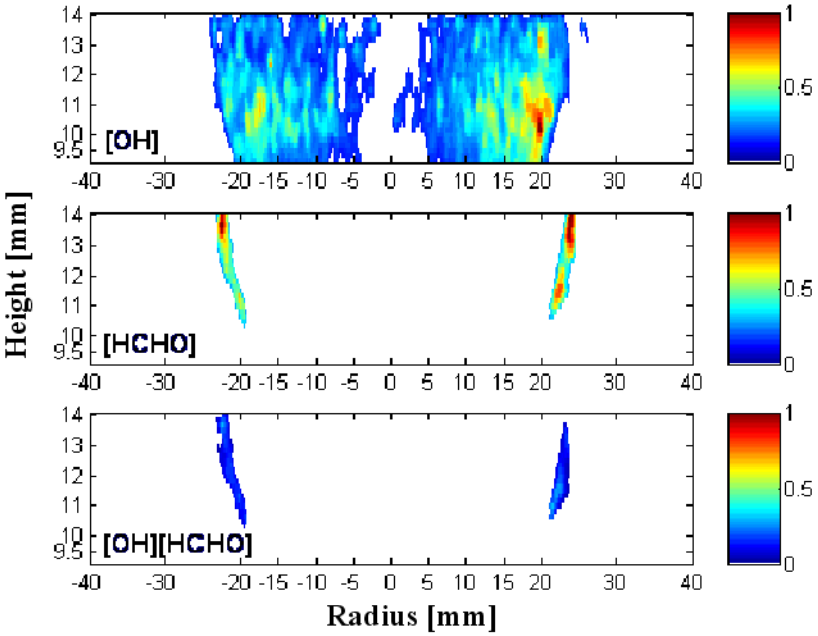

Figure 8.3: An example of processed single-shot image taken from simultaneous measurement from OH/HCHO PLIF. OH-PLIF image (top), HCHO-PLIF image (middle) and peak heat release rate position (bottom). Height above the burner nozzle exit is shown in mm's. Normalized intensity values are shown on the right column within color-bars.

overlapping is multiplied by a factor of 5 for comparison with the other profiles. All images were found to match well, thereby producing the area of reaction zone, even at the location of high swirl structure. Figure 8.5 shows the other burner height ranging from 17.5-22.5 mm. Swirling scalar field can be seen at this height indicated by hydroxyl and formaldehyde molecule, which indicates highly turbulent flow field.

Mean and standard deviation of the two-dimensional histogram of peak heat release rate is indicated in figure 8.6 for these two heights. 1000 single-shot images of the peak heat release rate contour were overlapped to generate these histogram. Results seem to be symmetrical in radial direction, showing the radial symmetry of the swirl flame.

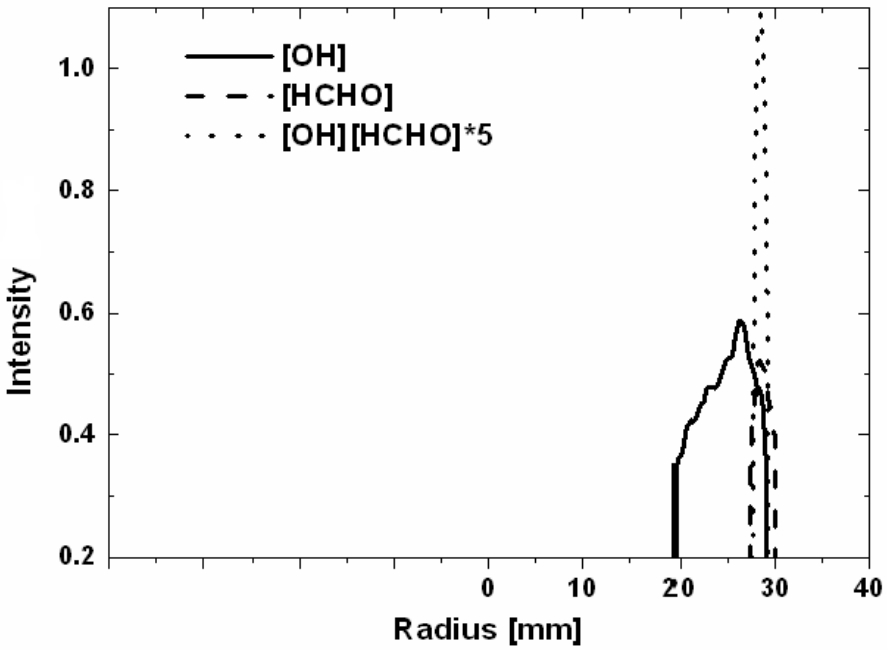

Figure 8.4: Profile extracted from the single shot PLIF image showing the matching of the OH and HCHO profile.

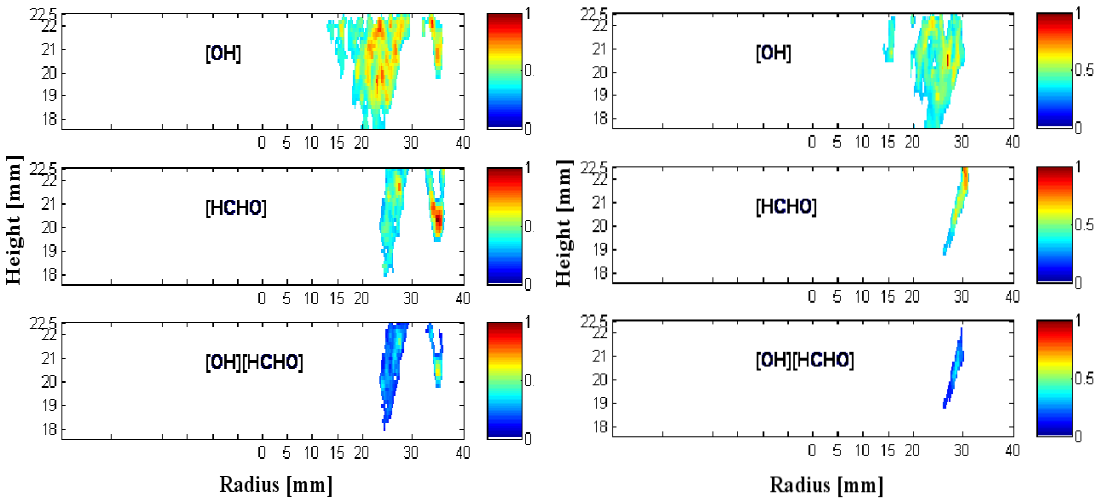

Figure 8.5: Two Snapshots taken from simultaneous measurement from normalized OH/HCHO PLIF at location H = 18-22.5 mm is shown. Location of peak heat release rate can be easily seen at highly curved regions of the flame (left column). Normalized intensity values are shown on the right column within color-bars.

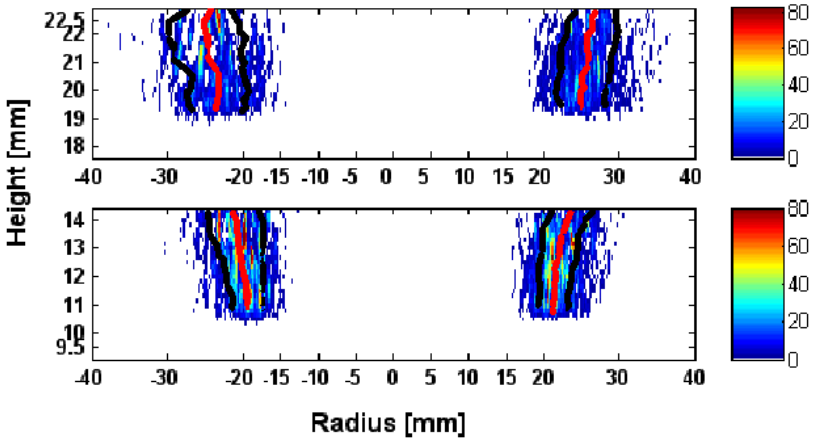

Figure 8.6: Two-dimensional histogram of the mean location of peak heat release rate evaluated from 1000 single-shot images at two different location of the burner. Solid lines shows the mean location and their standard deviation.

8.4 Conclusion

A turbulent premixed flame was measured using simultaneous laser induced fluorescence of hydroxyl and formaldehyde molecule. Such measurement provided insight into the flame front location of turbulent flames and also the position of peak heat release rate. We have used a single laser system for excitation of both molecule and also showed that the signal to noise ratio was high enough to extract information on a single-shot basis, which is important in turbulent flames. The complete flame was not captured from a single sheet due to the limitation in height of the laser sheet. The increase in height of the laser sheet reduced our signal to noise ratio drastically and the signal from the formaldehyde molecule was hardly detectable on a single shot basis. Our measurement have shown that it is possible to measure simultaneously hydroxyl and formaldehyde molecules in a highly turbulent lean-premixed swirled flame. Such measurement can be very useful in locating optimal reaction zone of an opposed jet flame where the reaction zone is restricted between the center of the nozzles [57].

9 Summary and Outlook

Flame front characteristics in various turbulent flames reaching from premixed to partially-premixed and non-premixed have been investigated using well known laser induced fluorescence technique. This work also provides insight into the flame front dynamics as a function of turbulent flow field. Turbulent flames from two different combustion devices have been investigated, namely the EKT turbulent opposed jet burner and the EKT swirl burner respectively.

The potential of extracting both, quantitative and qualitative information from the chosen combustion devices were huge. From the same setup, flames from diffusion to the premixed limit were studied, will varying parameters like Reynolds number, turbulent intensities and strain rate. Additionally, the extracted information could be used to validate and test the capability of the numerical model for the prediction of complex phenomenon. This will indirectly help in no longer relying on trial and error technique for designing combustion devices.

Investigated molecules were selected according to their presence near the reaction zone and formed in abundance during combustion processes under highly turbulent conditions. They were also checked for the possibility of single-shot detection and state of the art planar measurement. The hydroxyl and formaldehyde molecule were used as flame front marker as they are important intermediate species in combustion using fossil fuels. Investigation of formaldehyde molecules in flame was done by comparing the literature emission spectrum with the spectrum taken in this study.

Advanced image processing have been applied to the raw planar images to extract relevant information. This included normalizing the laser intensity, series of filtering, smoothing and binary image extraction. Various filtering methods ranging from median to non-linear diffusion filtering was applied to obtain the important gradients of intensity thereby removing attached unwanted noise. Sensitivity analysis was carried to choose the set of parameters applied to the images and different algorithms were checked for compatibility with the images.

Several important observations have been made during the investigation in opposed jet flames and will be detailed below.

- Increase in strain rate due to bulk velocity resulted in compression of the reaction zone and hence the OH detection area. The global flame area defined by the OH transient structure was found to be decreasing with increasing Reynolds number. And, decreasing OH global area shows a higher sensitivity with respect to flame extinction. A sharp increase in global area was found for the flame with the high degree of premixing ($\phi = 1.2$). This increase clearly indicates the transition from the regime where flame burns similar to non-premixed ones to the premixed regime.

- Local area distribution provided the information on radial symmetry and distribution of the flame. Radial symmetry was found for all flames measured in the opposed jet burner.

- Flame length and the mean stoichiometric contour provided qualitative information on the stage of turbulence. No drastic change in flame length with increasing Reynolds number shows the presence of "young turbulence". Results of the mean stoichiometric contour indicated that the mechanism of flame extinction is driven by strain effects rather than severe wrinkling.

- PDF of flame front angle was found to be symmetrical for all investigated flames and was found to be centered around 0 deg.

- The instantaneous hydroxyl layer thickness evaluated by PITLIF was found to be smaller for flames having a higher fuel-side equivalence ratio as compared to OH-PLIF results. The extent of spatial movement of the partially premixed flame front drops with enhanced premixing.

- The autocorrelation function was found to have a steeper curve for the higher Reynolds number flame compared with its lower counterpart. It was also found that the autocorrelation function fall into the same curve when normalized by their integral time. This collapse a single curve implies that the relative distribution of fluctuation rates at a single point in these turbulent flows is the same as that at a different point.

- Hydroxyl integral time scales are found to be independent of radial direction. The hydroxyl integral time scale reaches a minimum at the axial location of peak OH.

The list of important conclusion are detailed below from the swirl jet flames.

- Insight into the reaction zone location in a swirled stabilized turbulent flame was provided using multi-scalar PLIF measurement.
- Usage of single laser system for excitation of both molecules showed that signal-to-noise ratio was good enough to extract the information on single-shot basis.
- Height of the laser sheet was limited and the complete capture of the flame does not look feasible with the current setup.

Bibliography

[1] Dreizler, A. and Janicka, J. "Diagnostic challenges for gas turbine combustor model validation, "Applied Combustion Diagnostics" (edited by K. Kohse-Höinghaus and J. Jeffries)". *New York: Taylor and Francis*, 2002.

[2] Bilger, B.W., Pope, S.B., Bray, K.N.C., and Driscoll, J.F. "Paradigms of turbulent combustion research". *Proceedings of the Combustion Institute*, 30:pp. 21–42, 2005.

[3] Bray, K.N.C. "The challenge of turbulent combustion". *Proceedings of the Combustion Institute*, 26:pp. 1–26, 1996.

[4] Bilger, B.W. "Future progress in turbulent combustion research". *Prog. Energ. Comb. Sci.*, 26:pp. 367–380, 2000.

[5] Hassel, E.P. and Linow, S. "Laser diagnostics for studies of turbulent combustion". *Measurement Science and Technology*, 11:R37–R57, 2000.

[6] Barlow, R.S., Dibble, R.W., Chen, J.-Y., and Lucht, R.P. "Effect of Damköhler number on superequilibrium OH concentrations in turbulent nonpremixed jet flames". *Combustion and Flame*, Vol. 82:pp. 235–251, 1990.

[7] Dibble, R.W., Hartmann, V., Schefer, R.W., and Kollmann, and W. "Conditional sampling of velocity and scalars in turbulent flames using simultaneous LDV-Raman scattering". *Experiments in Fluids*, 5:pp. 103–113, 1987.

[8] Landenfeld, T., Kremer, A., Hassel, E.P., Janicka, J., Schäfer, T., Kazenwadel, J., Schulz, C., and Wolfrum, J. "Laser-diagnostic and numerical

study of strongly swirling natural gas flames". *Proceedings of the Combustion Institute*, 27:pp. 1023–1029, 1998.

[9] Janus, B., Dreizler, A., and Janicka, J. "Flow field and structure of swirl stabilized non-premixed natural gas flames at elevated pressure". *Proceedings of ASME Turbo Expo 2004 Power for Land, Sea, and Air*, GT-2004-53340:pp. 1–10, June 14-17, 2004.

[10] Schneider, C., Dreizler, A., and Janicka, J. "Fluid dynamical analysis of atmospheric reacting and isothermal swirling flows". *Flow, Turbulence and Combustion*, 74:pp. 103–127, 2005.

[11] Renfro, M.W., King, G.B., and Laurendeau, N.M. "Quantitative hydroxyl concentration time-series measurements in turbulent nonpremixed flames". *Applied Optics*, Vol.38(21):pp. 4596–4608, 1999.

[12] Brockhinke, A., Bülter, A., Rolon, J.C., and Kohse-Höinghaus, K. "Picosecond-LIF measurements of minor species concentration in a counterflow diffusion flame interacting with a vortex". *Applied Physics B*, pages pp. 491–496, 2001.

[13] Geyer, D., Kempf, A., Dreizler, A., and Janicka, J. "Scalar dissipation rates in isothermal and reactive turbulent opposed-jets: 1-D Raman/Rayleigh experiments supported by LES". *Proceedings of the Combustion Institute*, 30:pp. 681–689, 2005.

[14] Brockhinke, A., Kohse-Höinghaus, K., and Andresen, P. "Double-pulse one dimensional Raman and Rayleigh measurements for the detection of temporal and spatial structures in a turbulent H2-air diffusion flame". *Optics Letters*, 21:pp. 2029–2031, 1996.

[15] Hult, J. "Development of time resolved laser imaging technique for studies of turbulent reacting flows". *PhD thesis, Lund University of Technology, Lund*, 2002.

[16] Long, B.L., Fourgette, D.C., Escoda, M.C., and Layne, C.B. "Instantaneous Ramanography of a turbulent diffusion flame". *Optics Letters*, 8:pp. 244–246, 1983.

[17] Fielding, J., Schaffer, A.M., and Long, M.B. "Three-scalar imaging in turbulent non-premixed flames of methane". *Proceedings of the Combustion Institute*, Vol.27:pp. 1007–1014, 1998.

[18] Frank, J.H., Kaiser, S.A., and Long, M.B. "Reaction-rate, mixture fraction and temperature imaging in turbulent methane/air jet flames". *Proceedings of the Combustion Institute*, Vol 29:pp. 2687–2694, 2002.

[19] Hult, J., Omrane, A., Nygren, J., Kaminski, C.F., Axelsson, B., Collin, R., Hult, J., P.-E.Bengtsson,, and Alden, M. "Quantitative three-dimensional imaging of soot volume fraction in turbulent non-premixed flames". *Experiments in Fluids*, 33:pp. 265–269, 2002.

[20] Nygren, J., Hult, J., Richter, M., Alden, M., Christensen, M., Hultqvist, A., and Johansson, B. "Three-dimensional laser induced fluorescence of fuel distributions in an HCCI engine". *Proceedings of the Combustion Institute*, Vol.29:pp. 679–685, 2002.

[21] Barlow, R.S., Carter, C.D., and Pitz, R.W. "Multi-species diagnostics in turbulent flames". *in Kohse-Höinghaus, K and Jeffries, J.B. (Eds.): Applied Combustion Diagnostics, Taylor and Francis, New York*, pages pp. 384–407, 2002.

[22] Nauert, A. and Dreizler, A. "Conditional velocity measurements by simultaneously applied laser doppler velocimetry and planar laser-induced fluorescence in a swirling natural gas/air flame". *Journal of Physical Chemistry*, 219:pp. 635–648, 2005.

[23] Donbar, J.M., Driscoll, J.F., and Carter, C.D. "Reaction zone structure in turbulent non-premixed jet flames-from CH-OH PLIF images". *Combustion and Flame*, Vol.122:pp. 1–19, 2000.

[24] Böckle, S., Kazenwadel, J., Kunzelmann, T., Shin, D.I., Schulz, C., and Wolfrum, J. "Simultanous single-shot laser-based imaging of formaldehyde, OH and temperature in turbulent flames". *Proceedings of the Combustion Institute*, Vol.28:pp. 279–286, 2000.

[25] Warnatz, J., Maas, U., and Dibble, R.W. "Combustion: physical and chemical fundamentals, modeling and simulation, experiments, pollutant formation". *3rd Ed. Springer-Verlag*, ISBN 3-540-67751-8, 1996.

[26] Kohse-Höinghaus, K. and Jeffries, B.J. "Applied Combustion Diagnostics". *Combustion: An International Series*, 2002.

[27] Eckbreth, A.C. "Laser Diagnostics for Combustion Temperature and Species". *2nd Ed., Gordon and Breach, 1996.*

[28] Daily, J.W. "Laser Induced Fluorescence Spectroscopy in Flames". *Progr. Energy Combustion Sci.*, 23:pp. 133–199, 1997.

[29] Kohse-Höinghaus, K. "Laser techniques for the quantitive detection of reactive intermediates in combustion systems". *Progr. Energy Combustion Sci.*, 20:pp. 203–279, 1994.

[30] Shin, D.I., Dreier, T., and Wolfrum, J. "Spatially resolved absolute concentration and fluorescence lifetime determination of HCHO in atmospheric pressure methane/air flames". *Applied Physics B*, 72:pp. 257–261, 2001.

[31] Nguyen, Q.V., Dibble, R.W., Carter, C.D., Fiechtner, G.J., and Barlow, R.S. "Raman-LIF measurement of temperature, major species, OH, and NO in a methane-air bunsen flame". *Combustion and Flame*, Vol.105:pp. 499–510, 1996.

[32] Carter, C.D. and Barlow, R.S. "Simultaneous measurements of NO, OH, and the major species in turbulent flames". *Optics Letters*, Vol.19(4):pp. 299–301, 1999.

[33] Heard, D.E., Jeffries, J.B., Smith, G.P., and Crosley, D.R. "Laser-Induced fluorescence measurements in methane/air flames of radicals important in prompt-NO formation". *Combustion and Flame*, Vol.88:pp. 137, 1992.

[34] Lucht, R.P., Sweeney, D.W., and Laurendeau, N.M. "Laser saturated fluorescence of OH concentration in flames". *Combustion and Flame*, 50:pp. 189–205, 1983.

[35] Cheng, T.S., Wehrmeyer, J.A., and Pitz, R.W. "Simultaneous temperature and multispecies measurement in a lifted hydrogen diffusion flame". *Combustion and Flame*, 91:pp. 323–345, 1992.

[36] Rahmann, U., Bülter, A., Lenhard, U., Düsing, R., Markus, D., Brockhinke, A., and Kohse-Höinghaus, K. "LASKIN- A simulation program for time-resolved LIF spectra". *Internal Report, University of Bielefeld*, 2003.

[37] Rahmann, U., Kreutner, W., and Kohse-Höinghaus, K. "Rate-equation modeling of single- and multiple-quantum vibrational energy transfer of OH (A2Sigma+, v'=0 to 3)" . *Applied Physics B*, 69:pp. 61–70, 1990.

[38] Luque, J. and Crosley, D.R. "LIFBASE". *MP-99-0099, SRI International*, 1999.

[39] Renfro, M.W. "Fluorescence-lifetime measurements in atmospheric-pressure flames using nanosecond-pulsed lasers". *Applied Physics B*, 74:pp. 167–174, 2002.

[40] Renfro, M.W. "Quantitative time series for minor-series concentrations: measurements and modeling in turbulent nonpremixed flames". *PhD thesis, Purdue University, USA*, 2000.

[41] Thompson, B.D. "Flame measurements using picosecond time-resolved laser-induced fluorescence". *MS thesis Purdue University West Lafayette IN*, 1992.

[42] Pack, S.D., Renfro, M.W., King, G.B., and Laurendeau, N.M. "Photon-counting technique for rapid fluorescence-decay measurement". *Optics Letters*, Vol. 23(15):pp. 1215–1217, 1998.

[43] Reichardt, T.A. "Minor-species number density measurements using picosecond time-resolved laser-induced fluorescence". *MS thesis Purdue University West Lafayette IN*, 1994.

[44] Reichardt, T.A., Klassen, M.S., King, G.B., and Laurendeau, N.M. "Real-time acquisition of laser-induced fluorescence decays". *Applied Optics*, 34:pp. 973–976, 1995.

[45] O'Connor, D.V. and Phillips, D. "Time-correlated single photon counting". *Academic Press London*, 1984.

[46] Alfano, A.J., Fong, F.K., and Lytle, F.E. "High repetition rate subnanosecond gated photon counting". *Rev. Sci. Instrum.*, 54:pp. 967–972, 1983.

[47] Desilets, D.J., Coburn, J.T., Lantrip, A.D., Kissinger, P.T., and Lytle, F.E. "On-the-fly determination of fluorescence lifetime from two-point decay measurements". *Analytical Chemistry*, Vol.58(6):pp. 1123–1128, 1986.

[48] Ballew, R.M. and Demas, J.N. "An error analysis of the rapid lifetime determination method for the evaluation of single exponential decays". *Analytical Chemistry*, (61):pp. 30–33, 1989.

[49] Chaturvedy, A., King, G.B., Laurendeau, N.M., Renfro, M.W., Kempf, A., Dreizler, A., Sadiki, A., and Janicka, J. "Comparision of OH time-series measurements and large-eddy simulations in H2 jet flames". *Combustion and Flame*, 139:pp. 142–151, 2004.

[50] Gökalp, I., Shepherd, I.G., and Cheng, R.K. "Spectral behaviour of velocity fluctuation in premixed turbulent flames". *Combustion and Flame*, 71:pp. 313–323, 1988.

[51] McQuay, M.Q. and Cannon, S.M. "Time-resolved temperature measurement in the developing region of an elliptic, jet diffusion flame at Reynolds number of 6000". *Combustion and Flame*, 119:pp. 13–33, 1996.

[52] Ikeda, Y., Kojima, J., Nakajima, T., Akamatsu, F., and Katsuki, M. "Measurement of local flame-front structure in turbulent premixed flame". *Proceedings of the Combustion Institute*, 28:pp. 343, 2000.

[53] Renfro, M.W., Guttenfelder, W.A., King, G.B., and Laurendeau, N.M. "Scalar time-series measurements in turbulent CH4/H2/N2 non-premixed flames: OH". *Combustion and Flame*, Vol. 123:pp. 389–401, 2000.

[54] Renfro, M.W., King, G.B., and Laurendeau, N.M. "Scalar time-series measurements in turbulent CH4/H2/N2 non-premixed flames: CH". *Combustion and Flame*, 122:pp. 139–150, 2000.

[55] Paul, P.H. and Najm, H.N. "Planar laser-induced fluorescence imaging of flame heat release rate". *Proceedings of the Combustion Institute*, pages pp. 43–50, 1998.

[56] Najm, H.N., Paul, P.H., Mueller, C.J., and Wyckoff, P.S. "On the adequacy of certain experimental observables as measurements of flame burning rate". *Combustion and Flame*, Vol.113:pp. 312–332, 1998.

[57] Fayoux, A., Zähringer, K., Gicquel, O., and Rolon, J.C. "Experimental and numerical determination of heat release in counterflow premixed laminar flame". *Proceedings of the Combustion Institute*, 30:pp. 251–257, 2005.

[58] Tobai, J. "Pikosekunden pump-probe DFWM spektroskopie-methoden von NH und OH in atmosphärendruckflammen: untersuchung des relaxationsprozesses bei elektronischer anregung und im grundzustand". *Dissertation: Ruprecht-Karls-Universität Heidelberg*, 2000.

[59] Harrington, J.E. and Smith, K.C. "Laser-induced fluorescence measurements of formaldehyde in a methane/air diffusion flame". *Chemical Physics Letters*, Vol. 202(3-4):pp. 196–202, 1993.

[60] Bäuerle, B., Warnatz, J., and Behrendt, F. "Time-resolved investigation of hot spots in the end gas of an S.I engine by means of 2-D double pulse LIF of formaldehyde". *Proceedings of the Combustion Institute*, pages pp. 2619–2626, 1996.

[61] Böckle, S., Kazenwadel, J., Kunzelmann, T., Shin, D.I., and Schulz, C. "Single-shot laser-induced fluorescence imaging of formaldehyde with XeF excimer excitation". *Applied Physics B*, Vol.70:pp. 733–735, 2000.

[62] Burkert, A., Grebner, D., Müller, D., Triebel, W., and König, J. "Single-shot imaging of formaldehyde in hydrocarbon flames by XeF excimer laser-induced fluorescence". *Proceedings of the Combustion Institute*, Vol.28:pp. 1655–1661, 2000.

[63] Graf, N., Gronki, J., Schulz, C., Baritaud, T., Cherel, J., Duret, P., and Lavy, J. "In-cylinder combustion visualization in an auto-igniting gasoline engine using fuel tracer- and formaldehyde-LIF imaging". *SAE*, 2001-01-1924, 2001.

[64] Klein-Douwel, R.J.H., Luque, J., Jeffries, J.B., Smith, G.P., and Crosley, D.R. "Laser-induced fluorescence of formaldehyde hot bands in flames". *Applied Optics*, Vol.39(21):pp. 3712–3715, 2000.

[65] Tobai, J. and Dreier, T. "Effective A-state fluorescence lifetime of formaldehyde in atmospheric pressure methane/air flames". *Applied Physics B*, 74(1):pp. 101–104, 2002.

[66] Tolocka, M.P. and Miller, J.H. "Measurement of formaldehyde concentrations and formation rates in a methane-air, non-premixed flame and their implication for heat release rate". *Proceedings of the Combustion Institute*, pages pp. 663–640, 1998.

[67] Najm, H.N., Knio, O.M., Paul, P.H., and Wyckoff, P.S. "A study of flame observable in premixed methane-air flame". *17th International Colloquium on the Dynamics of Explosion and Reactive System*, 119, July 25-30, 1999.

[68] Möhlmann, G.R. "Formaldehyde detection in air by laser induced fluorescence". *Society of Applied Spectroscopy*, Vol. 39(No.1):pp. 98–101, 1985.

[69] Renfro, M.W., Pack, S.D., King, G.B., and Laurendeau, N.M. "A pulse-pileup correction procedure for rapid measurements of hydroxyl concentrations using picosecond time resolved laser-induced fluorescence". *Applied Physics B*, 69:pp. 137–146, 1999.

[70] Lutz, A.E., Kee, R.J., Grcar, J.F., and Rupley, F.M. "OPPDIF: A fortran program for computing opposed-flow diffusion flames, Scandia National Laboratories". *Report No. SAND96-8243*, 1996.

[71] Jähne, B. "Practical handbook on image processing for scientific applications". *Book Published by CRC Press (1997).*

[72] Perona, P. and Malik, J. "Scale-space and edge detection using anistropic diffusion". *IEEE Comp. Soc. Workshop on Computer Vision*, pages pp. 16–22, 1987.

[73] Perona, P. and Malik, J. "Scale-space and egde detection using anistropic diffusion". *IEEE Transactions on Pattern Analysis and Maschine Intelligence*, Vol. 12(7):pp. 629–639, 1990.

[74] Weickert, J. "Nonlinear diffusion filtering". *Handbook of Computer Vision and Application*, Vol. 2:pp. 423–450.

[75] Weickert, J. "A review of nonlinear diffusion filtering". *Scale-Space Theory in Computer Vision, Lecture Notes in Computer Science*, Vol. 1252:pp. 3–28, 1997.

[76] Malm, H., Sparr, G., Hult, J., and Kaminski, C.F. "Nonlinear diffusion filtering of images obtained by planar laser induced fluorescence spectroscopy". *Journal of Optical Society of America*, A 17:pp. 2148–2156, 2000.

[77] Schiessl, R., Dreizler, A., and Mass, U. "Comparison of different ways for image post-processing: Detection of flame fronts". *Society of Auto. Eng.*, 441(8):pp. 151–189, 1999.

[78] Kempf, A., Forkel, H., Chen, J.-Y., Sadiki, A., and Janicka, J. "Large-eddy simulation of a counterflow configuration with and without combustion". *Proceedings of the Combustion Institute*, 28:pp. 35–40, 2000.

[79] Geyer, D., Nauert, A., Dreizler, A., and Janicka, J. "Flow and scalar field properties of a turbulent opposed jet burner". *Proceedings of Externes TECHFLAM Seminar, Karlsruhe*, 2002.

[80] Geyer, D., Nauert, A., Dreizler, A., and Janicka, J. "Finite-rate chemistry effects in turbulent opposed flows: comparison of Raman/Rayleigh measurements and Monte Carlo PDF simulations". *Proceedings of the Combustion Institute*, 30:pp. 711–718, 2005.

[81] Geyer, D. "1D-Raman/Rayleigh experiments in turbulent-opposed jet flows". *PhD thesis, Technische Universität Darmstadt*, 2004.

[82] Kitajima, A., Ueda, T., Matsuo, A., and Mizomoto, M. "A comprehensive examination of the structure and extinction of turbulent non-premixed flames formed in a counterflow". *Combustion and Flame*, Vol.121:pp. 301–311, 2000.

[83] Kitajima, A., Ueda, T., Matsuo, A., and Mizomoto, M. "Experimental investigation of the flame structure and extinction of turbulent counterflow

non-premixed flames". *Proceedings of the Combustion Institute*, 26:pp. 137–143, 1996.

[84] Kitajima, A., Torikai, H., Takeuchi, M., and Oya, M. "Experimental study of extinction and its quantification in laminar and turbulent counterflow CH4-N2/O2-N2 nonpremixed flames". *Combustion and Flame*, 137:pp. 93–108, 2004.

[85] Korusoy, E. and Whitelaw, J.H. "Extinction and relight in opposed flames". *Experiments in Fluids*, Vol. 33:pp. 75–89, 2002.

[86] Luff, D., Korusoy, E., Lindstedt, P., and Whitelaw, J.H. "Counterflow flames of air and methane, propane and ethylene with and without periodic forcing". *Experiments in Fluids*, Vol. 35:pp. 618–626, 2003.

[87] Mastorakos, E., Taylor, A.M.K.P., and Whitelaw, J.H. "Extinction and temperature characteristics of turbulent counterflow diffusion flames with partial premixing". *Combustion and Flame*, 91:pp. 40–54, 1992.

[88] Mastorakos, E., Taylor, A.M.K.P., and Whitelaw, J.H. "Scalar dissipation rate at the extinction of turbulent counterflow non-premixed flames". *Combustion and Flame*, 91:pp. 55–64, 1992.

[89] Mastorakos, E. "Turbulent combustion in opposed jet flows". *Phd thesis, Imperial College, University of London*, 1993.

[90] Mounaim-Rouselle, C. and Gökalp, I. "Strain effects on the structure of counterflowing turbulent flames". *Proceedings of the Combustion Institute*, Vol. 25:pp. 1199–1205, 1994.

[91] Sardi, K., Taylor, A.M.K.P., and Whitelaw, J.H. "Exinction of turbulent counterflow flames under periodic strain". *Combustion and Flame*, 120:pp. 265–284, 2000.

[92] Sardi, E. "Turbulent flame extinction in unforced and periodically forced counterflows". *Ph.D. thesis, Imperial College of Science, Technology and Medicine, University of London*, 1997.

[93] Sardi, K., Taylor, A.M.K.P., and Whitelaw, J.H. "Conditional scalar dissipation statistics in a turbulent counterflow". *Journal of Fluid Mechanics*, Vol. 361:pp. 1–24, 1998.

[94] Shepherd, I.G. "Flame surface density and burning rate in premixed turbulent flames". *Proceedings of the Combustion Institute*, 26:pp. 373–379, 1996.

[95] Tsuji, H., Yoshida, A., and Endo, and N. "Effect of turbulence on extinction of counterflow diffusion flame". *Proceedings of the Combustion Institute*, pages pp. 1191–1197, 1994.

[96] Yoshida, A., Igarashi, T., and Kotani, Y. "Extinction of turbulent diffusion flames by Kolmogorov microscale turbulence". *Combustion and Flame*, Vol. 109(4):pp. 669–681, 1997.

[97] Bray, K.N.C., Champion, M., and Libby, P.A. "Premixed flame in stagnation turbulence part IV: a new theory for the Reynolds stresses and Reynolds fluxes applied to impinging flows". *Combustion and Flame*, Vol. 120:pp. 1–18, 2000.

[98] Jones, W.P. and Prasetyo, W. "Probability density function modeling of premixed turbulent opposed jet flames". *Proceedings of the Combustion Institute*, 26:pp. 275–282, 1996.

[99] Kostiuk, L.W., Bray, K.N.C., and Chew, T.C. "Premixed turbulent combustion in counterflowing streams". *Combustion Science and Technology*, 64:pp. 233–241, 1989.

[100] Kostiuk, L.W., Bray, K.N.C., and Cheng, R.K. "Experimental study of premixed turbulent combustion in opposed streams. Part III - Spatial structure of flames". *Combustion and Flame*, Vol. 118:pp. 129–139, 1999.

[101] Gülder, Ö.L., Smallwood, G.J., Wong, R., Snelling, D.R., Smith, R., Smallwood, G.J., Deschamps, B.M., and Sautet, J-C. "Flame front surface characterisitics in turbulent propane/air combustion". *Combustion and Flame*, Vol. 120(No. 4):pp. 407–416, 2000.

[102] Geyer, D., Omar, S., Nauert, A., Ludwig, A., Dreizler, A., and Janicka, J. "A Comprehensive characterization of a turbulent opposed jet flame by 1D-Raman/Rayleigh, 2D-LIF, and LDV". *1st International SFB-568 Workshop Darmstadt*, 2002.

[103] Lachaux, T., Halter, F., Chauveau, C., Gökalp, I., and Shepherd, I.G. "Flame front analysis of high-pressure turbulent lean premixed methane-air flames". *Proceedings of the Combustion Institute*, 30:pp. 819–826, 2005.

[104] Soika, A., Dinkelacker, F., and Leipertz, A. "Pressure influence on the flame front curvature of turbulent premixed flames: comparision between experiment and theory". *Combustion and Flame*, 132:pp. 451–462, 2003.

[105] Blevins, L.G. and Gore, J.P. "Computed structure of low strain rate partially premixed CH4/air counterflow flames: implications for NO formation". *Combustion and Flame*, 116:pp. 546–566, 1999.

[106] Tanoff, M.A., Smooke, M.D., Osborne, R.J., Brown, T.M., and Pitz, RW. "The sensitive structure of partially premixed methane-air vs. air counterflow flames". *Proceedings of the Combustion Institute*, 26:pp. 1121–1128, 1996.

[107] Syred, D.G. and Beer, J.M. "Combustion in swirling flows". *Combustion and Flame*, 23:pp. 143–201, 1974.

[108] Huang, Y. and Yang, V. "Effect of swirl on combustion dynamics in a lean-premixed swirl-stabilized combustor". *Proceedings of the Combustion Institute*, 30:pp. 1775–1782, 2005.

[109] Kremer, A., Hassel, E.P., and Janicka, J. "Velocity measurements in a strongly swirling natural gas flame". *Engineering Research*, 63, 1997.

[110] Schäfer, T., Kazenwadel, J., Schulz, C., and Wolfrum, J. "Multi-dimensional imaging of temperature, OH and NO in the techflam swirl burner". *PCI data archive*.

[111] Böckle, S., Kazenwadel, J., Kunzelmann, T., Shin, D.I., Schulz, C., and Wolfrum, J. "Simultaneous single-shot laser-based imaging of formaldehyde, OH, and temperature in turbulent flames". *Proceedings of the Combustion Institute*, 28:pp. 279–286, 2000.

Resume of Sunil Kumar Omar

Personal

Birth (dd.mm.yyyy)	10.12.1977	Banda (UP), India

Education

Secondary School	1992-1993	MP Board of Education, India
Higher Secondary School	1994-1995	MP Board of Education, India
Batchalor of Engineering (A.M.Ae.S.I)	1995-1998	The Aeronautical Society of India New Delhi, India
Master of Technology (M-Tech Aerospace)	1998-2000	The Indian Institute of Technology Madras, India Supervision: Dr. S. R. Chakravarthy "Development of an Experimental setup for the Combustion of Solid Propellant under high pressure oscillatory condition"
PhD Studies (Mechanical Engineering)	2001-2005	TU-Darmstadt Supervision: Prof. Dr.-Ing. J. Janicka "Investigation of Turbulent Flame Characteristics via Laser Induced Fluorescence"

Scholarships

Gate Scholarship	1998-2000	The Indian Institute of Technology Madras, India
CTES, British Chevening Scholarship	2004-2005	Imperial College, London, UK

Research Projects

	2002	Department of Mechanical Engineering, Purdue University, US Collaboration with Dr. M. Renfro
	2004-05	Imperial College, London Project with Dr. A. L. Heyes and Dr. J.P.Feist